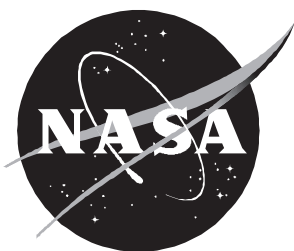# Simultaneous Three-Dimensional Velocity and Mixing Measurements by Use of Laser Doppler Velocimetry and Fluorescence Probes in a Water Tunnel

Dan H. Neuhart, David J. Wing, and Uleses C. Henderson, Jr.

Simultaneous Three-Dimensional Velocity and Mixing Measurements by Use of Laser Doppler Velocimetry and Fluorescence Probes in a Water Tunnel

Dan H. Neuhart
Lockheed Engineering & Sciences Company • Hampton, Virginia

David J. Wing
Langley Research Center • Hampton, Virginia

Uleses C. Henderson, Jr.
Purdue University • West Lafayette, Indiana

This publication is available from the following sources:

Contents

Summary

A water tunnel investigation was conducted to demonstrate the capabilities of a laser-based instrument that can measure velocity and fluorescence intensity simultaneously. Fluorescence intensity of an excited fluorescent dye is directly related to concentration level and was used to indicate the extent of mixing in flow. This instrument is a three-dimensional laser Doppler velocimeter (LDV) in combination with a fluorometer for measuring fluorescence intensity variations. This capability allows simultaneous flow measurements of the three orthogonal velocity components and mixing within the same region. Two different flows which were generated by two models were studied: a generic nonaxisymmetric nozzle propulsion simulation model with an auxiliary internal water source that generated a jet flow and an axisymmetric forebody model with a circular sector strake that generated a vortex flow. The off-body flow fields around these models were investigated in the Langley 16- by 24-Inch Water Tunnel. The experimental results were used to calculate 17 quantities that included mean and fluctuating velocities, Reynolds stresses, mean and fluctuating dye fluorescence intensities (proportional to concentration), and fluctuating velocity and dye concentration correlations. An uncertainty analysis was performed to establish confidence levels in the experimental results. In general, uncertainties in mean velocities varied between 1 and 7 percent of free-stream velocity; uncertainties in fluctuating velocities varied between 1 and 5 percent of reference values. The results show characteristics that are unique to each type of flow.

Introduction

To measure as many characteristics as possible of the off-body flow around aerodynamic shapes and within internal flow fields, instruments were developed that provide flow information previously unavailable. Mechanical probes often adversely affect or disturb the flows they are measuring. Therefore, emphasis was placed on the use of nonintrusive optical measurement techniques which can provide useful qualitative and quantitative details of many types of flow. In particular, the development of the laser gave the researcher a tool for making accurate determinations of many flow characteristics without significantly disturbing the flow field. Volumes of literature have been written which describe techniques for nonintrusive optical flow measurements. Reference 1 provides a thorough overview of general laser-based flow measurement concepts.

Laser Doppler velocimetry has been used to investigate flow fields since the mid-1960's and is described extensively in the literature. (See refs. 2 and 3.) Fluorescence intensity measurement is a well-known spectroscopic technique and fluorometry concepts are described in reference 4.

The nonintrusive technique used in the experiments discussed in this paper was a combined laser Doppler velocimetry (LDV) measurement of velocity and laser-induced fluorescence intensity measurement of dye concentration. A system was developed for the Langley 16- by 24-Inch Water Tunnel and was first described in reference 5. The three orthogonal velocity components of flow were measured by the LDV section of the instrument; the scalar fluorescence intensity was measured simultaneously by the fluorometry section at the same location as the LDV measurements and characterized mixing in the flow.

The simultaneous measurement of three velocity components and the level of dye concentration in the sample volume is a unique capability that allows examination of flows that have both a high degree of three-dimensionality and significant mixing between different regions of the flow field. By examination of the entire three-dimensional characterization of the flow, the predominant time-averaged mechanisms in mixing as well as the three-dimensional velocity flow field can be determined. This had not previously been accomplished. To demonstrate the capability of the instrument, two very different types of flows were examined: a turbulent jet flow and a vortex flow. Reference 5 reported on the design and operation of the hardware and software systems as well as provided some limited test results. This paper presents detailed experimental results from measurements of each type of flow and provides an analysis of estimated experimental uncertainties.

Symbols

A	area integral of vorticity
a	transformation matrix element
B	bias error
b	absorption path length, in. (see eq. (2))
b_0	jet half-height, in.
C	integration circuit for circulation
c	transformation matrix element; concentration of fluorescent dye, mg/ml
$D_{e^{-2}}$	laser beam diameter at e^{-2} of peak intensity levels, mm

d	distance of lens from tunnel wall, in.	$\sqrt{u'^2}, \sqrt{v'^2}, \sqrt{w'^2}$	rms velocity fluctuations, in/sec
d_f	sample volume fringe spacing, $\dfrac{\lambda}{2\sin\kappa}$, μm	$\overline{u'c'}, \overline{v'c'}, \overline{w'c'}$	covariance of velocity and concentration fluctuations, in.-V/sec
d_m	sample volume diameter, $\dfrac{4\lambda f}{\pi D_{e-2}\cos\kappa}$, μm	$\overline{u'u'}, \overline{v'v'}, \overline{w'w'}$	Reynolds normal stresses, in^2/sec^2
dS	surface element area, in^2	$\overline{u'v'}, \overline{v'w'}, \overline{w'u'}$	Reynolds shear stresses, in^2/sec^2
$\mathbf{e}$	unit vector in LDV coordinate system	v	lateral velocity, in/sec
F	fluorescence; fluorescence intensity, V; focal length, in.	W	lateral depth in test section, in.; nozzle width, in.
f	transmitting lens focal length, mm	w	vertical velocity, in/sec
I_0	incident radiant power, W	x	variable in uncertainty analysis
$\mathbf{i}, \mathbf{j}, \mathbf{k}$	unit vectors in tunnel coordinate system	x, y, z	Cartesian coordinates, in.
K	constant, (see eq. (3))	α	angle of attack, deg
l_m	sample volume length, $\dfrac{4\lambda f}{\pi D_{e-2}\sin\kappa}$, μm	Γ	circulation, in^2/sec
		Δ	implies uncertainty when preceding quantities in uncertainty analysis
N	number of samples	δ_{ij}	Kronecker delta
n	index of refraction of media	ε	absorptivity of fluorescent dye, in^{-1} (see eq. (2))
P	precision limit, $P = t_{95}S$	θ	angle in LDV coordinate system, deg
r	result in uncertainty analysis; radius, in.	κ	laser beam half-angle, deg
S	precision index	λ	wavelength of light, nm
t_{95}	statistical t distribution value giving 95-percent confidence level	ν	frequency of laser light, Hz
		$\Delta\nu$	shift or Doppler frequency, Hz
		ρ	correlation coefficient; fluid density, lbf-sec^2/ft^4
U	uncertainty; velocity, in/sec	σ	standard deviation
u	axial velocity, in/sec	Φ	quantum efficiency of fluorescent dye
u_c	jet exit velocity, in/sec	ϕ	strake azimuth angle (0° at top center), deg
u_m	jet centerline axial velocity, in/sec	ω	vorticity, sec^{-1}
u_n	velocity perpendicular to fringes, in/sec	Subscripts:	
$\overline{u}, \overline{v}, \overline{w}$	mean velocity components, in/sec	B_{ij}	correlation coefficient for bias errors
u', v', w'	velocity fluctuations, in/sec	cell	quantity for measurement grid cell

2

i, j	elemental component
ij	elemental indices
j	jet
LDV	laser Doppler velocimetry coordinate system
max	maximum
P_{ij}	correlation coefficient for precision errors
pk	peak or maximum
r	result
rms	root mean square
RSS	root sum square
t	tangential
v, g, b	components in LDV coordinate system
x	streamwise component
∞	free-stream condition

Superscripts:

$'$	fluctuating quantity
$-$	mean quantity
$\wedge$	unit vector

Abbreviations:

AD	axisymmetric decay region of jet
A/D	analog-to-digital
ANSI	American National Standards Institute
ASME	American Society of Mechanical Engineers
CD	characteristic decay region of jet
LDV	laser Doppler velocimetry
LSB	least significant bit
PC	potential core region of jet
PMT	photomultiplier tube
rms	root mean square
RSS	root sum square
SV	sample volume

Experimental System Description and Test Technique

Measured and Calculated Quantities

Four quantities are measured in the instrument coordinate system: $\Delta\nu_{u,v}$, $\Delta\nu_{u,g}$, $\Delta\nu_{u,b}$, and F_i which are the three frequency components that yield three velocity components and the fluorescence intensity in the LDV coordinate system, respectively. From these untransformed measurements, the following 17 quantities are calculated: $\overline{u}, \overline{v}, \overline{w}$; $\sqrt{\overline{u'^2}}$, $\sqrt{\overline{v'^2}}$, $\sqrt{\overline{w'^2}}$; $\overline{u'u'}$, $\overline{v'v'}$, $\overline{w'w'}$; $\overline{u'v'}$, $\overline{v'w'}$, $\overline{w'u'}$; $\overline{u'c'}$, $\overline{v'c'}$, $\overline{w'c'}$; and $\overline{c}, c'$.

Instrumentation System

Velocimeter. The use of two laser beams for velocity measurement is illustrated by figure 1. The planar wave fronts of the two intersecting beams form a set of interference fringes that are parallel to the line bisecting the angle between the two intersecting beams. Velocities are measured in the sample volume (SV) formed at the intersection of the two beams. The Doppler effect occurs because of the relative motion between the laser-scattering particle and both the laser source and receiver. Equation (1) can be derived from the principles of Doppler theory (refs. 2 and 3) and relates the Doppler shift frequency $\Delta\nu$ to the velocity of the particle by

$$u_n = \frac{\lambda \, \Delta\nu}{2 \sin \kappa} \qquad (1)$$

The Doppler signal is characterized by a varying amplitude and a constant frequency. The locus of the signal half-amplitudes forms a bump called the pedestal. This pedestal is the result of the Gaussian power distribution across the laser beam that peaks at the beam center and is generally filtered out early in the signal-processing procedure.

The signal will produce a frequency that can be directly related to velocity. However, it does not indicate the direction in which the particle was moving (i.e., positive or negative). A technique that resolves this directional ambiguity is frequency shifting; a frequency shift can be chosen to encompass the expected range of negative velocities above the zero frequency point.

Fluorometer. Fluorescence intensity is measured at the same SV location as the LDV measurements. (See fig. 1.) The measurement of fluorescent dye concentration is based on the fact that the dye molecules absorb energy from the incident radiation. A molecule that absorbs the input energy is raised

to some excited state. While excited molecules dissipate energy through collisions with other molecules, some molecules spontaneously fluoresce as they return to their initial ground state. Fluorescence is the result of the decay from the excited state to a lower molecular energy state. The absorption and emission of energy occur at specific wavelengths for each type of dye.

An equation describing the relationship between dye concentration and fluorescence (ref. 4) is

$$F = \Phi I_0 (1 - e^{-\varepsilon bc}) \qquad (2)$$

where F is the fluorescence intensity, Φ is the quantum efficiency of the dye, I_0 is the incident radiant power, ε is the molar absorptivity of the dye, b is the absorption path length, and c is the molar concentration. The equation shows that an increase in concentration increases the fluorescence intensity. At very dilute concentration levels, the relationship becomes nearly linear; reference 4 suggests a simplified equation

$$F = K\Phi I_0 \varepsilon bc \qquad (3)$$

For a given dye and laser power at a given location (no change in b) with $K = $ Constant, equation (3) shows a direct relationship between fluorescence intensity F and concentration c. The linear response range of the concentration extends from about 10^{-8} to 0.1 mg/ml. (See ref. 4.) The dye concentration was 0.0245 mg/ml in the injected fluid used to obtain all of the results reported here.

The fluorescent dye used in this system was fluorescein. The absorption and emission spectra are shown in figure 2. The relative intensity, which is proportional to dye concentration, is shown as a function of light wavelength. The wavelengths from the argon ion laser used in the test instrument are indicated at the top of the plot. The absorption spectrum represents the range of wavelengths which the dye will absorb energy from the input radiation. The peak absorption occurs at a wavelength of 494 nm and is very near the argon laser blue line of 488 nm, which is beneficial because nearly maximum energy can be absorbed; the emission occurs at the longer wavelength of 515 nm. For absorption at any discrete wavelength along the absorption spectrum, the dye will produce fluorescence throughout the entire emission spectrum. If the absorption occurs at a wavelength other than at the peak of the absorption spectrum, the intensity of fluorescence will decrease across the spectrum.

The peak of the emission spectrum occurs at 515 nm, which is very close to the argon laser green

line of 514.5 nm. This produces scattered laser light that will contaminate the fluorescence signal; therefore, the fluorescence signal must be filtered both electronically and optically. The amplifier for the fluorescence signal has a low-pass filter of 30 Hz that reduces the contribution of the LDV burst signal in the fluorescence signal. However, laser light generates broadband shot noise in the photomultiplier tube (PMT) some of which will be low frequency and will contribute noise to the signal. In addition, a 530-nm edge filter that passes light at 530 nm and above (50-percent transmission at 530 ± 5 nm and less than 1 percent at 515 nm) is used to filter out the light below 530 nm that includes the three argon laser lines. Therefore, the fluorescence signal is derived from light above the edge threshold of 515 nm. Then, as the concentration of dye in the sample volume at the intersection of the two laser beams increases or decreases, the fluorescence signal level increases or decreases, correspondingly. By introducing fluorescent dye into one of two interacting flows (e.g., a dye-saturated jet emission into a dye-free free-stream flow), the mixing of these flows can be studied by measuring the variation of fluorescence within the flow field.

The contribution to the fluorescence signal by the LDV laser light is optically and electronically filtered. However, the fluorescence emission band overlaps into the LDV wavelength band. Although the fluorescence signal levels are generally lower than the LDV levels, an additional broadband shot noise is introduced into the LDV signals at the PMT. Narrow band-pass filter settings control the contribution of the shot noise from the PMT fluorescence signal. The low-frequency fluorescence interference caused by flow fluctuations was eliminated by 25-MHz high-pass frequency filters in the electronic frequency shift units (i.e., downmixers) of the LDV system, which will be described later.

Test Facility

Experiments were performed in the Langley 16-by 24-Inch Water Tunnel which is shown in figure 3. The tunnel has a useful vertical test section of about 4.5 ft. The velocity in the test section can be varied from 0 to 9 in/sec, which yields unit Reynolds numbers from 0 to 7.73×10^4 ft^{-1}, respectively, based on a water temperature of 75°F. The typical test section velocity is 3 in/sec. Test models in the experiments described in this report were sting-mounted as shown in figure 4. This system provided model rotation in two perpendicular planes with ranges of $\pm 15°$ and $\pm 33°$. The center of rotation was located on the centerline of the test section

and 15.25 in. above the base of the sting. Electric motors, which are mounted outside of the test section and remotely controlled, drove the model support system. Model angles were set with reference to the visual indicators within an accuracy of about $\pm 0.25°$. Other details of the water tunnel are discussed in reference 6.

When the tunnel is full of water, the center of the test section is about 10 ft below the water surface. The weight of the water causes the test section acrylic walls to deflect outward to a maximum of approximately 0.090 in. The curvature of the walls, which results, alters the alignment of the laser beams passing through them. Coincidence of the six beams at the same point could not be maintained without additional braces; at least two braces were necessary to minimize the wall deflection. The braces limited optical access and restricted the choices of laser beam positions.

Models

The first test model was a scaled-down version of a wind tunnel propulsion-simulation model with a nonaxisymmetric nozzle. Auxiliary water was supplied to simulate jet flow from the nozzle exit. A photograph of this model installed in the test section is shown in figure 5(a); a sketch with principle model dimensions is provided in figure 5(b). As shown, the axis system origin was centered on the nozzle exit. This model was tested at angles of attack of 0° and 4° and at jet-to-free-stream velocity ratios of 0, 1.7, and 3. Dye injection orifices at various locations around the aft part of the model provided visualization of the flow over the boattail region. This dye was introduced into the model from the bottom. Fluorescent dye could also be introduced into the jet water supply from outside of the tunnel to permit visualization of the jet plume or measurement of mixing in the jet shear region. The jet flow was controlled by a system of valves and a flowmeter. Because of the presence of internal dye orifice tubes, foam was inserted in the nozzle upstream of the throat (fig. 5(b)) to ensure jet flow uniformity. The foam tended to compress unevenly and several attempts were made to achieve a relatively uniform flow distribution. The final test configuration was much improved over the model without the foam. A drawing of the model with the location of the measurement planes is shown in figure 6. The planes were 15 × 25 arrays ($\Delta y = 0.1$ in., $\Delta z = 0.0833$ in.) centered on the nozzle. The measurement plane closest to the nozzle exit was located one nozzle width downstream of the exit ($x = 1.032$ in.). The second plane was located three nozzle widths downstream of

the exit ($x = 3.096$ in.). A modified jet model was also tested which had a solid constant cross section extending one body length downstream from the nozzle exit. Its cross section was the same as the nozzle and provided a solid plume simulation of the jet.

The second test model was an axisymmetric forebody with a strake attached near the nose. This model was also a scaled-down representation of a wind tunnel model that had been tested to determine the effectiveness of strakes for forebody control of airplane attitude. The flat strake planform was a circular sector located along the model centerline with an inboard edge that conformed to the body shape. Limited tests were also performed on a cambered strake that had the same planform shape as the flat strake. Dye orifices were located on either side of the strake. Figure 7(a) is a photograph that shows the model in the test section. The principle model dimensions are given in figure 7(b). As shown, the camber for the cambered strake was applied longitudinally; the right edge in the side view is in the X-Y plane. Section A-A in figure 7(b) shows the cusped cross section of the strake. With the model positioned at an angle of attack of 25°, the strake was tested at azimuthal angles of 50° and 60° as measured from the top of the model.

Colored dye flow visualization (fig. 7(a)) indicated a very coherent vortex shed from the strake; this flow was studied with the laser system at three measurement planes downstream of the strake. The locations of the measurement planes relative to the model are shown in figure 8. The first plane downstream of the nose of the model was located at the downstream end of the strake ($x = 3.75$ in.) and was an 11 × 25 array ($\Delta y = 0.06$ in., $\Delta z = 0.056$ in.). The second and third grids (at $x = 5.15$ in. and $x = 10$ in.) were 18 × 25 ($\Delta y = 0.0625$ in., $\Delta z = 0.0625$ in.) and 17 × 25 ($\Delta y = 0.0625$ in., $\Delta z = 0.125$ in.) arrays, respectively. All of the measurement grids were located with their vertical inboard edges at the model top centerline and they extended spanwise in the negative Y direction perpendicular to the centerline. The vertical extent of the first array was limited by optical access between the wall support braces of the test section. This also limited the number and location of the other measurement grids.

Experimental Technique

Optical system setup. The laser measurement system operation can be described with the use of figure 9. For each measured velocity component, a pair of laser beams of the same wavelength cross to form a sample volume (SV). The SV is nominally

60 μm in diameter and 1.25 mm long and is moved throughout the flow field to the measurement location. At each location, three velocity components are measured by three pairs of beams at three different wavelengths. Additionally, fluorescence intensity is measured from the fluorescent dye, which has been introduced into part of the flow field. Mixing of the dyed and undyed flows is examined by moving the SV through the boundary between the two flows (e.g., the shear region between the jet core and freestream flows in fig. 9), and measuring the variations in fluorescence intensity.

The formation of the beam pairs used to measure each velocity component is depicted in figure 10. Laser light from an argon ion laser is separated into its many component colors using prisms and mirrors. Three of these colors are selected: violet (λ = 476.5 nm), blue (λ = 488 nm), and green (λ = 514.5 nm). These beams are split, which forms the three pairs of beams. One beam in each pair has a Bragg-shift frequency of 40 MHz applied for flow direction discrimination. Each beam is sent through a fiber-optic cable, passed through a transmitting lens outside the test section, and focused at the same point to create the sample volume in the test section. The scattered light from particulates in the water as well as fluorescent light emitted by the dye is collected on the opposite side of the test section by receiving lenses, which are focused on the SV.

The collected light is processed as shown in figure 11. The data acquisition process begins by focusing the collected light onto the face of a fiber-optic cable. A light-separating optics unit divides the light into the three individual laser colors and the fluorescent light color. Each light component is directed to a separate photomultiplier tube that converts the photons to an electrical signal that contains all of the frequency information, which includes the original Bragg-shift frequency of 40 MHz, necessary to determine the three velocity components. The electrical signals are amplified for processing. Each signal is high-pass filtered at 25 MHz and its frequency downmixed from 40 MHz to 100 kHz, which removes the pedestal and reduces the effective Bragg-shift frequency. This process allows better resolution of the Doppler signal frequency relative to the Bragg-shift frequency. The signals are then low-pass filtered at 200 kHz to reduce high-frequency noise before the burst counter processing. The velocity resolution of the system (smallest velocity measurable) is based on the counter resolution, which is about 1.5 percent at a velocity of 3 in/sec ($\approx$1 mm/sec). The counters send frequency information in digital form to the data acquisition unit. The fluorescence signal from the photomultiplier tube is amplified and sent as an analog signal to the data acquisition unit, where it is digitized.

The data acquisition unit collects, multiplexes, and buffers the data and then sends it to the computer. The unit imposes coincidence conditions on the LDV data for two or three channels, which ensures that data from the separate channels arrive within a user-specified time period. This control is necessary for calculating cross correlations such as turbulent Reynolds shear stress quantities, for which each contributing parameter must be acquired from the same measured event (i.e., same particle). In addition, the analog fluorescence data is sampled to provide data concurrent with the digital LDV data. The data from the data acquisition unit is sent via an 8-bit parallel port to the computer, which is a 32-bit desktop system.

The laser beam transmission and light collection system is shown in relation to the water tunnel test section in figure 12. The system emits the laser beams into the test section from one side; the scattered light and fluorescent light are collected (off-axis) on the opposite side. This arrangement is referred to as the forward-scatter mode of light collection. Two orthogonal beam pairs (violet and blue, λ = 476.5 nm and 488 nm, respectively) are transmitted directly on-axis into the test section for measuring the streamwise and vertical velocities. The third beam pair (green, λ = 514.5 nm) is transmitted into the test section at an angle of 45°, which becomes about 32° within the test section after refraction by the water. This beam pair allows measurement of the velocity component normal to the beam angle bisector, which is then used to calculate the on-axis lateral velocity component in the test section coordinate system. Figure 13 is a photograph of the transmitting and receiving optics.

The transmitting and receiving optics are positioned by a traverse control system that can be either operated independently of the computer in manual mode or controlled interactively by the computer system. The positioning system controls seven motor-encoder units: three X-Y-Z units on the transmitting side, an auxiliary unit for the off-axis laser beams, and three X-Y-Z units on the receiving side. The encoder resolution for the auxiliary motor-encoder system is 0.000025 in/pulse (0.635 μm/pulse). The resolution for the other six motor-encoder units is 0.00005 in/pulse (1.27 μm/pulse).

The characteristics of the sample volume for each of the three component colors are given in

Table I. LDV Sample Volume Characteristics

[See figure 14]

| Characteristics | W/d, in./in., of— | | | | |
	0/18.2	4/15.2	8/12.2	12/9.2	16/6.2
Axial: $\lambda = 476.5$ nm (violet), $d_f = 3.85$ μm					
f, in.	19.4	20.4	21.4	22.4	23.4
d_m, μm	51	54	56	59	62
l_m, mm	1.10	1.16	1.21	1.27	1.32
Vertical: $\lambda = 488$ nm (blue), $d_f = 3.94$ μm					
f, in.	19.4	20.4	21.4	22.4	23.4
d_m, μm	52	55	58	60	63
l_m mm	1.12	1.18	1.24	1.30	1.36
Lateral: $\lambda = 514.5$ nm (green), $d_f = 4.98$ μm					
f, in.	19.8	22.1	24.4	26.6	28.9
d_m, μm	56	63	69	76	82
l_m, mm	1.45	1.62	1.78	1.95	2.12

table 1 based on the distances symbolically defined in figure 14. Note that when the LDV system is run in the coincidence mode (i.e., all three velocity measurements are taken from the same particle), the effective measurement region is the intersection of the sample volumes formed by the various beams. Because the sample volumes are approximated by ellipsoids (i.e., the locus of the beams where the power is e^{-2} of the peak of the Gaussian beam power distribution), the intersection of the SV's can be approximated by calculating the length of the intersection of the maximum ellipsoid dimensions. For the beams in the center of the test section, this calculation yields an intersection length of about 220 μm. This represents the effective SV length for measurements made in the coincidence mode because it is within the focus length of the receiving optics. The maximum intersection diameter is about 56 μm, which is equal to the smallest single SV diameter.

Laser light sheet. Flow visualization was obtained by laser light sheet excitation of the fluorescein dye. The laser light sheet was generated by sweeping an argon ion laser beam of 488 nm at a 500-Hz rate. This gave a light sheet with an essentially uniform power distribution. Details on the laser light sheet system can be found in reference 7. The laser light sheet was oriented perpendicular to the longitudinal body axis. Flow patterns visualized by the fluorescence were photographed end-on from downstream of the model by reflecting the image to the outside of

the tunnel with a mirror placed at an angle of 45° in the bottom of the test section.

Seeding material. The seeding particles used in the experiments can be described with figure 15. The top of the figure shows a scanning electron microscope photograph of the seeding particles in a water sample taken from the water tunnel during a test run; the bottom of the figure shows a particle size distribution plot. The number of particles increases as the average particle size decreases; the smallest particle size range shown is 5 to 10 μm. The average size for the sample was 13 μm. The analysis indicated that only 0.5 percent of the particles were greater than 100 μm. The particles were identified as being mostly hydrated iron oxide, Fe_2O_3 (i.e., rust), with an average density of 3.6 gm/cm^3. By analytical methods of references 8 and 9, the majority of the test seeding particles were determined to be small enough to follow the flow accurately.

Model test conditions and setup. All tests were run at a free-stream velocity of 3 in/sec. The nonaxisymmetric propulsion model was tested at angles of attack of 0° and 4°. The jet-to-free-stream velocity ratios were 0, 1.7, and 3. In addition to the planar data, vertical velocity profiles were measured near the nozzle exit and axial scans were taken downstream of the exit on the model centerline.

The axisymmetric forebody with a strake was tested at an angle of attack of 25°. The baseline

flat strake was tested at strake azimuthal angles of $\phi = 50°$ and $60°$ relative to the top of the model. The cambered strake was also tested at the same two angles. However, because of limited optical access to this model, only one Y-axis scan for each azimuthal angle was made.

At the beginning of each test, the LDV system optics were aligned in an empty test section. The model was then inserted in the tunnel test section and the tunnel was filled with water. After the water was circulated to minimize any density gradients because of temperature variations, the tunnel flow was set to the test velocity of 3 in/sec. The axis system origin for these data was centered on the nozzle exit for the jet test and at the nose of the forebody for the strake test.

Measurements were initiated; as the beams were moved from point to point, the burst counter data rates were monitored to ensure that optical alignment was maintained. At each point, up to 1000 samples were acquired with a maximum acquisition time of 1 to 2 min. All data reported herein were calculated from the samples taken at each point.

Analysis of Results

The results of the experiments are presented in this section for the nonaxisymmetric propulsion model (jet test) followed by the axisymmetric forebody-strake model (strake test). An estimate of the uncertainties in the calculated results are given in tables AI(a)–AI(c) of the appendix.

Nonaxisymmetric Propulsion Model

Flow visualization. Laser light sheet flow visualization results are shown in figures 16 and 17. The qualitative turbulent development of the jet at a jet-to-free-stream velocity ratio of 1.7 and angle of attack of 4° is shown in the sequence of photographs in figure 16. The nozzle flow was visualized with the laser light sheet perpendicular to the jet longitudinal axis at the exit ($x/W = 0$), one nozzle width downstream of the exit ($x/W = 1$), and three nozzle widths downstream of the exit ($x/W = 3$). Dye traces in the jet flow show the increased mixing at the periphery of the jet as the laser light sheet was moved downstream. The flow from the boattail region is shown in the sequence of photographs in figure 17 for the same flow conditions as figure 16 but at different downstream locations of x/W. In figure 17, only the dye external to the model is shown, which mixed with the jet in a very short distance from the exit.

Mean velocity results. The axial velocity u is the component of primary interest in jet studies. Average axial velocity data taken for the jet at several spanwise stations are shown in figure 18 at $\alpha = 0°$ and a jet-to-free-stream velocity ratio of 1.7. The uncertainty in this quantity was estimated to be about ± 2.4 percent of U_∞. The maximum velocity occurred at the station $y = 0.3$ in. and decreased on either side. (The offset in the $+Y$ direction was most likely caused by some residual nonuniformity of the foam in the nozzle throat.) In addition, the velocity profiles at the closest measurement station $x = 1.032$ in., (fig. 18(a)) showed a velocity deficit between $z = 0$ and -0.2 in. for two scan locations ($y = 0$ in. and -0.3 in.). This was probably caused by either the model support strut and the associated wake momentum deficit or affected by the flow-conditioning foam in the throat. Comparison of the two axial measurement stations reveals a reduction in peak velocities at the aft station $x = 3.096$ in. (See fig. 18(b).) The velocity reduction effect of increasing longitudinal distance is shown directly for each of the jet-to-free-stream velocity ratios in figure 19. In addition, the effect of velocity ratio at each station is shown by comparing the velocity levels in figures 19(a) and 19(b).

Flow characteristics that are not discernible from line plots are often revealed by examining data contours in the measurement plane. Contours of axial velocity at $\alpha = 0°$ are shown in figure 20(a) at the first measurement station downstream of the nozzle exit ($x/W = 1$). The axial velocities were maximum in the irregularly shaped region near the center of the measurement grid. A ring of low-momentum flow around this high-speed region that resulted from flow separation on the boattail is shown. Also, a region of reduced axial velocity is evident in the lower center section of the grid. This velocity defect was a result of the momentum deficit in the wake shed by the model support strut. The effect of angle of attack is shown in figure 20(b). The effect was evident in two concentrated low-velocity regions in the top corners of the grid. They represent the reduced axial velocity regions associated with body-shed vortices from the model upper surface corners.

Vertical distribution of axial velocity. A limited number of surveys were made near the nozzle exit on the leeward side of the model. The surveys were made outside of the jet in a vertical direction at angles of attack of 0° and 4°. Vertical distributions of axial velocity at the nozzle exit are shown in figure 21 for three jet-to-free-stream velocity ratios. (Note that the bottom of the vertical axis is not at zero; however, the vertical upper extent of the nozzle

is shown in fig. 21. The vertical upper extent of the body is 0.615 in.) An increase in jet velocity ratio increased local axial velocity u for a substantial range of Z. This is indicative of jet interference effects on the nozzle boattail. A significant region of reversed flow existed with the jet off. A comparison of velocity profiles which includes a solid-plume jet simulator is shown in figure 22. The solid-plume jet simulator was a constant-dimension extension aft of the nozzle exit. The model with the solid plume generated more reverse flow than the jet-off configuration, which indicated a trend opposite to what would be expected. The solid-plume jet model was expected to represent the flow better than the jet-off configuration. This result indicates that the jet flow must be provided for proper simulation of off-body flow physics. A direct comparison of the effect of angle of attack at three velocity ratios is shown in figure 23. In all three cases, angle of attack increased the local axial velocity u profiles.

Axial velocity decay. The jets in this study are effectively three-dimensional incompressible turbulent jets. In general, incompressible turbulent jets are characterized by the presence of three distinct regions in axial velocity decay along the jet axis. (See refs. 10 and 11.) These regions are illustrated in figure 24 and are classified as follows:

1. *Potential core (PC) region.* This region is the section from the nozzle exit at point 0 to point A. Mixing that occurs at the jet boundaries has not yet permeated the entire flow field and leaves a region that is characterized by a uniform velocity on the axis equal to the jet exit velocity.

2. *Characteristic decay (CD) region.* This region is the section from point A to point B. Within this region, the axial velocity decay is dependent upon nozzle exit geometry; velocity profiles in the plane of the minor axis of the exit are found to be similar whereas, those in the plane of the major axis are nonsimilar. Therefore, this region is termed characteristic of the initial geometry.

3. *Axisymmetric decay (AD) region.* This region is the section from point B to point C where point C is not a specific, well-defined location. The axial velocity u decays in this region in accordance with $u \propto x^{-1}$, which is characteristic of axisymmetric jets. The entire flow approaches axisymmetry and thus exit geometry is no longer a factor. Velocity profiles in this region are similar in both planes of symmetry. Far downstream beyond point C, a fourth region of fully axisymmetric flow is observed.

Again, note that most of the characteristics of the jet in the PC and CD regions (i.e., near field) appear to be determined completely by the exit geometry and that flow in the AD and fully axisymmetric region (i.e., far field) is independent of the exit geometry.

In accordance with the discussion by Rajaratnam (ref. 11), the test model produces a bluff compound jet. The exit aspect ratio of the model in this study (width/height of $W/2b_0 = 1.9$) qualifies this jet to be bluff as well as compound because of the motion of the surrounding fluid. Bluff jets originating from square nozzles have been studied by Trentacoste and Sforza. (See ref. 12.) When the characteristic decay region is excluded, they discovered that the potential core of a square jet is followed very quickly by an axisymmetric decay region. These trends were apparent in the current experimental results.

Experimental observations of the current configuration of bluff compound jets were made at jet-to-free-stream velocity ratios of 1.7 and 3.0, with a nozzle exit aspect ratio ≈ 1.9. The axial scans were made in the near field up to $x/2b_0 \approx 9$ (far field is considered to be $x/2b_0 > 100$), where x is the axial distance and b_0 is the nozzle half-height. Figure 25 presents the axial velocity decay of the jet for both jet velocity ratios. Despite the scatter in the data for $U_j/U_\infty = 3$, the potential core ($u/u_{\max} = 1$) seems to extend to $x/b_0 = 2$ for both jet velocity ratios. The uncertainty in $\overline{u}/\overline{u}_{\max}$ was ± 0.9 and ± 0.5 percent for $U_j/U_\infty = 1.7$ and 3, respectively. The similar behavior for both jet velocity ratios supports the hypothesis made by Sforza (ref. 10) that the characteristics of the PC region are determined by the nozzle exit geometry and not the initial velocity. Following the potential core region, the two curves decay linearly on the log-log plot. (The curve for the velocity ratio of 3 follows the trend better than for 1.7.) The jet of this investigation seems to follow the trend of a bluff jet, which is characterized by the potential core followed by an axisymmetric decay region.

Turbulence results. The turbulence results were calculated on the basis of the statistical analysis technique of mean and standard deviation for experimental samples. Note that other sources of apparent turbulence such as vortex meandering, which could contribute to deviations from the mean flow, were not addressed here.

The Reynolds stresses reported herein will actually be the stresses per unit density. Two examples of actual Reynolds normal and shear stresses are $\rho\overline{u'u'}$ and $\rho\overline{w'u'}$, respectively. Reynolds normal stresses are analogous to pressures because they represent the

reaction of a surface to turbulent flow of momentum (e.g., $\rho u'^2 dS$) through the surface in the direction of the momentum. The distribution of average axial Reynolds normal stress $\overline{u'u'}$ is shown in figure 26 at two measurement stations. The uncertainty in this normalized $\overline{u'u'}$ was ± 0.067 percent. The levels of this stress decreased with increased distance from the nozzle exit and with reduction of velocity ratio. The asymmetry in the profile is accentuated at the higher velocity ratio. In general, the depression in the profile at the station $x = 1.032$ in. for the lower velocity ratio is characteristic of jets because the velocity fluctuations tend to be significant in the shear layer at the periphery of the jet. The vertical distributions of the average transverse Reynolds normal stress $\overline{v'v'}$ and the vertical Reynolds stress $\overline{w'w'}$ are shown in figures 27 and 28, respectively. The estimated uncertainties for these quantities were ± 1.5 percent and ± 0.042 percent, respectively. Trends similar to those for $\overline{u'u'}$ occur with the change in velocity ratio and distance. However, the levels in $\overline{v'v'}$ were significantly higher than $\overline{u'u'}$ and $\overline{w'w'}$ levels. Other experimental studies (e.g., Hinze, ref. 13) show variations from complete isotropy in these stresses to domination by the axial component $\overline{u'u'}$ over the smaller vertical $\overline{w'w'}$ and lateral $\overline{v'v'}$ components. The high indicated $\overline{v'v'}$ levels in this study probably result primarily from a larger background transverse turbulence intensity (i.e., rms velocity fluctuation) v' in the water tunnel test section and, to a lesser extent, from the propagation of errors through the coordinate transformation of $\overline{v'v'}$.

After the model tests, the velocity fluctuation v' was measured in the empty test section. The off-axis optical equipment used to measure the transverse velocity was dismantled and remounted to send the green laser beams of 514.5 nm through a perpendicular tunnel sidewall to measure the transverse velocity component directly. The resulting orthogonal system revealed a nonisotropic turbulence environment. The directly measured transverse component v' was consistently 15 to 25 percent greater than u', which was consistently 30 to 44 percent greater than w'. Possibly one contribution to the large v' is the transverse oscillation generated upstream where the water encounters the back wall and turns the corner without the aid of turning vanes. Another possible contribution is the capture of the tunnel-free surface waves which are drawn down into the test section by the curved lip at the upper back wall. Finally, without an isolation system, acoustic disturbances from the pump or from cavitation on the back side of the speed-control butterfly valve could be transmitted through the water into the test sec-

tion in some predisposed direction. These oscillations could also cause localized tunnel wall movement that would alter the instrument focus and produce apparent turbulence.

The distributions of average Reynolds shear stresses $\overline{u'v'}$, $\overline{u'w'}$, and $\overline{w'u'}$ are shown in figures 29–31, respectively, for two measurement planes and two velocity ratios. These tangential stresses are analogous to shear stresses because they cause a shear stress reaction on the surface. They represent cross correlations of turbulent fluctuating velocities and show the turbulent transport of momentum in an orthogonal direction. For example, the $\overline{u'v'}$ stresses in figure 29 represent the turbulent transport of X momentum in the Y direction. In general, the $\overline{u'v'}$ correlations were positive; therefore, a positive increase in u' corresponded to a positive increase in v'. The estimated uncertainty in this stress was ± 0.22 percent. The $\overline{v'w'}$ stresses in figure 30 represent the turbulent transport of Y momentum in the Z direction. The estimated uncertainty in this stress was ± 0.10 percent. These stresses were lower than the $\overline{u'v'}$ stresses but showed a strong reversal near the centerline in both measurement planes, especially for the high-velocity ratio. Note that the value of the shear stress, whether positive or negative, indicates the relative amount of momentum transfer due to turbulence. The $\overline{w'u'}$ stresses in figure 31 represent the transport of Z momentum in the X direction. The estimated uncertainty was ± 0.036 percent. The $\overline{w'u'}$ stresses were similar in magnitude to the $\overline{u'v'}$ stresses; however, the character of the distribution was similar to the $\overline{v'w'}$ stresses. The distributions changed sign on either side of the jet centerline which is characteristic for these shear stresses in a jet. (Note that the effective center of the jet is not at $z = 0$.) A contour plot of the $\overline{w'u'}$ stress in figure 32 shows the three-dimensional nature of the distribution in the jet.

Fluorescence results. The distribution of the local average, nondimensionalized fluorescent dye concentration across the jet is given for two measurement locations in figure 33. The estimated level of uncertainty was ± 0.71 percent. Dye was injected into the jet flow and the fluorescence intensity measurement showed the dispersion and extent of mixing with the free-stream flow. As shown in the figure, the spread of the jet increased with increasing distance downstream of the exit. The dimensional peak concentration value c was reduced at the aft measurement station, which indicated that the spread of the dye as a result of mixing reduced the concentration at the center.

The fluctuations (i.e., standard deviations) in fluorescent dye concentration are shown in figure 34. The estimate of uncertainty was ±0.57 percent. These fluctuations occur where fluid that is tagged with dye mixes with undyed free-stream fluid. High fluctuation values indicate high levels of mixing as occurs in a shear layer. For a jet, the fluctuations would be high in the shear layer surrounding the jet and be near zero in the free stream (i.e., no dye) and in the center of the jet where the dye concentration remains constant (i.e., no mixing). The distributions in figure 34 indicate the increased mixing in the downstream direction as the shear layer grows. The centerline value increased as the turbulent mixing reached the center of the jet. Contours of the concentration fluctuations are shown in figure 35 for the first measurement plane downstream of the nozzle exit. The contours map out the shear layer between the free stream and the jet by identifying the region of mixing.

The cross correlation between velocity and concentration fluctuations is indicated by calculation of the statistical covariance of these quantities similar to the way in which the mean shear stresses were calculated. For the streamwise component u'

$$\overline{u'c'} = \frac{\sum\limits_{i=1}^{N} (u_i - \overline{u})(c_i - \overline{c})}{N} \tag{4}$$

where u_i and c_i are instantaneous values. Equation (4) is the numerator (i.e., the covariance) of a correlation coefficient for u' and c'. Therefore, if this quantity is zero, u' and c' are uncorrelated and independent. These relationships are shown in figures 36–38. All of the distributions as well as the concentration fluctuations exhibited a reduction at the center of the jet. The correlations between u' and c' are indicated in figure 36 and were similar for the two velocity ratios at each measurement station. The estimated uncertainty, when normalized by U_∞ and the maximum c value for the scan, was ±0.015 percent. The values were positive-correlated in the jet shear regions and indicated a stronger relationship between the axial and concentration fluctuations than did the other two velocity fluctuations. This implies that the axial fluctuations were the predominant mechanism in shear layer mixing. The $\overline{v'c'}$ relationship is indicated in figure 37 and the $\overline{w'c'}$ cross correlations are shown in figure 38; their levels are clearly lower than the $\overline{u'c'}$ quantities. Their respective estimates of uncertainty were ±0.056 and ±0.005 percent.

Axisymmetric Forebody With Strake

Flow visualization results on the axisymmetric forebody indicated that the strake position of 50° provided the most coherent vortex structure. A position of 60° was also investigated to provide a comparison with the strake configuration of 50°. (Only these two strake angles were investigated in this study.) Observations confirmed the confinement of fluorescent dye in the vortex core both visually and quantitatively in the fluorescence measurements, which negated the possibility of turbulent mixing in the vortex. The highly three-dimensional nature of the vortex provides a flow for which the LDV is well suited and one that is very different from the jet flow shown previously. In the flow visualization figures, the flow is moving from right to left in each figure and the nose of the body is in the left side of each figure.

Flow visualization. Flow visualization results are shown in figures 39 and 40 for strake azimuth angles of $\phi = 50°$ (baseline) and 60°, respectively. The flow visualization technique used was laser light sheet excitation of fluorescein dye with visualization from the downstream perspective. The development of the strake vortex in the axial downstream direction was visualized by positioning the laser light sheet perpendicular to the body longitudinal axis. The four stations shown represent the midstrake position (fig. 39(a)), followed by the three measurement stations where quantitive data were taken. The development of the strake vortex for $\phi = 50°$ indicated that the vortex remained laminar along the entire length of the model. Figures 39(b)–39(d) show the development of a body vortex shed from the model surface inboard of the strake vortex. This is characteristic of slender bodies at incidence. Both vortices were rotating in the counterclockwise direction in the figures. Initially, the vortex generated by the strake at 60° (fig. 40(a)) showed a similar characteristic to the vortex generated by the strake at 50°. However, as the vortex migrated downstream, the appearance of the streaklines from the strake at 60° was less well-defined and the vortex appeared to be larger. This would imply a vortex was formed with a broader velocity distribution and a larger axial velocity deficit; examination of the mean velocity distributions shows this to be true.

Mean velocity results. Average u, v, and w velocity distributions across the vortex of the strake at 50° are given in figures 41(a)–41(c), respectively, at several vertical z stations. The respective uncertainties, when normalized by U_∞, were estimated to be 0.011 or −0.012, 0.031 or −0.033, and 0.0085

or -0.0098. The scans were taken at the first measurement station $x = 3.75$ in. downstream of the body nose. The location of the vortex center was $z = 1.35$ in. and $y = 0.725$ in.; the peak axial u (fig. 41(a)) and tangential (vertical, w in fig. 41(c)) velocities occurred at this Z location. The distributions of transverse velocity v (fig. 41(b)) indicated that the center of the vortex ($z = 1.35$ in.) was the location of minimum transverse velocity. This is reasonable because there should be minimal velocity through the center of the vortex along the scan Y-axis. The axial velocity distributions in figure 41(a) revealed that velocity levels were different on either side of the vortex as a result of the presence of the flow field around the body. The centerline of the body was at $y = 0$; z increased away from the body in the vertical direction. The axial velocity was greater on the body side of the vortex, perhaps, because of the accelerated flow around the side of the body. One exception was the closest z station ($z = 1.08$ in.) where the flow had apparently separated and the measurements were made in the wake of the body. The axial velocities from the other scan locations show a gradual decrease from $y = -0.4$ to 0, although still larger than U_∞. This may result from the gradual approach to the wake region where the effect of the characteristic momentum deficit is increasing. Also, there was a curious bump in the distributions outboard ($y \approx -1.0$) of the main vortex axial velocity deficit. This distortion is the result of the presence of the strake wake (i.e., separated free-shear layer) before it wrapped into the strake vortex. A similar bump was present in the tangential (vertical) velocity distributions in figure 41(c).

A comparison of the three mean velocity distributions at the first measurement station for the two strake roll angles is shown in figures 42(a)–42(c). The axial velocity distributions are plotted in figure 42(a). The distribution for the strake at 60° is displaced in Y because of the physical displacement of the tip of the strake when rotated outboard an extra 10°. The axial velocity distributions reveal that the strake at 60° generated a larger axial velocity deficit than the strake at 50°. In addition, the width of the velocity deficit is slightly broader. The transverse (fig. 42(b)) velocities v do not show significant differences in terms of levels. The vertical (fig. 42(c)) velocities w show slightly higher peak values and a greater distance between upper and lower velocity peaks for the strake at 60°. This result indicates that the vortex from the strake at 60° was spread out more as was implied by the flow visualization shown earlier. In general, as vortices approach breakdown, the ratio of peak tangential to axial velocities increases. In this

investigation, therefore, the vortex from the strake at 60° would appear to reach breakdown first.

The effect of cambering the strake at 50° is shown for the three mean velocities in figures 43(a)–43(c). The X location for the cambered strake was slightly different because of the limited optical access which resulted from the braces around the test section. The cambered strake showed much less axial velocity deficit than the baseline flat strake in figure 43(a), which indicated that the baseline strake vortex would likely break down sooner. No significant difference in transverse velocity was noted in figure 43(b). The vertical velocities in figure 43(c) indicated that the cambered strake generated slightly higher velocity peaks. The width of the vortex viscous subcores, defined as the region between the peaks of the tangential velocity distribution, appeared to be quite similar.

Contours of mean axial velocity for the strakes at 50° (baseline) and 60° are shown in figures 44 and 45, respectively. Comparison of the minimum values in the center of the contours shows the greater extent of the velocity deficit for the strake at 60°, which again indicates the tendency of the vortices from the strake at 60° to break down sooner.

Streamwise vorticity and circulation. Streamwise vorticity was calculated from the average v and w velocity data. Identification of regions of concentrated vortical flow enables location of vortex centers and the determination of relative local vortex strengths. Contours of streamwise vorticity in the three measurement planes are shown for the strakes at 50° and 60° in figures 46 and 47, respectively. The estimated maximum uncertainty in streamwise vorticity was calculated to be 2.59 sec^{-1}. This rather large value is based on the worst-case vertical velocity gradient, which exists in the center of the vortex. In other regions of the vortex flow, the uncertainty would be greatly reduced. The peak vorticity generated by the strake at 50° was stronger at the first measurement station than for the strake at 60°. However, the vorticity from the strake at 50° decreased more at the second station than did the vorticity from the strake at 60°, which was then slightly higher. The peak vorticity at the final measurement station was about the same for both strakes. Evidence of the wake from the strake before it is wrapped into the vortex exists on the lower right-hand side of the measurement grids.

The variation of streamwise vorticity across the center of the vortex for the three measurement stations is shown in figure 48 for the strake at 50°. The vorticity peaks were reduced at the downstream

measurement stations. This reduction was accompanied by a slight lateral spread in the vorticity distribution on the right-hand side of the peaks. However, the vorticity appears to be decreasing overall in the downstream direction probably because of viscous dissipation, especially, when considering the flow low test Reynolds number of 2.5×10^4 ft^{-1}. The effect of the strake wake was observed as a bump in the previously mentioned velocity distributions. There is also a bump from the effect of the strake wake in the vorticity distributions on the $-Y$ side of the vorticity peak.

The amount of vorticity contained in the viscous subcore has been examined. The streamwise vorticity calculated at the grid points is compared to the vertical velocity distribution in figure 49 for the strake at 50° at the second measurement station. On the right-hand side of the figure, a very small amount of vorticity appears inboard of the point ($y \approx -0.56$ in.) where the peak negative velocity begins to move back toward zero. On the outboard side of the figure ($y \approx -1.0$ in.), the same trend was apparent. However, the wake of the strake added a small bump of vorticity before it diminished. Overall, most of the vorticity appeared to exist in the area defined as the vortex subcore. The remainder of the vorticity is contained in the so-called rotational core (i.e., outer core) which is very small for this trailing vortex when compared to the outer cores of wing leading edge vortices. (See ref. 14.) This outer core behavior is consistent with the theory that the area outside of the outer core can be represented as a potential vortex which implies irrotational (i.e., nonvortical) flow.

Calculation of total circulation indicates total vortex strength and allows vortex comparisons. Circulation values were calculated for the two strake angles at each of the measurement stations. Because of the sign convention, circulation on the side of the model where the measurements were taken was calculated as a negative value. At the first station, the vorticity distributions were cut off by limited optical access, especially for the strake at 60°, as shown in figures 46 and 47. This prevents any comparison at the first station. At the second station, circulation values for the strakes at 50° and 60° were -2.76 in^2/sec and -3.03 in^2/sec, respectively, with an estimated uncertainty of 0.012 in^2/sec. Integration over the entire grid at the third station included some additional negative vorticity from other sources, especially for the strake at 50°. By integrating over that part of the grid which excluded this additional vorticity, circulation values of -2.94 in^2/sec and -3.13 in^2/sec were calculated for the strakes at 50° and 60°, respectively.

Comparison of these circulation values implies that the vortex from the strake at 60° was stronger and therefore likely to breakdown sooner.

Fluorescence results. The spanwise distribution of normalized fluorescent dye concentration is shown in figure 50 for the strake at 50° along the vortex center scan line at the three measurement stations. The estimated uncertainty in this quantity was calculated to be ±0.93 percent. Baseline values have been removed from c and $c_{\max}$. The dye remained confined to the viscous core and no turbulent mixing was evident.

Conclusions

An instrument that simultaneously measures three velocity components and mixing (from fluorescence intensity) in a flow field by application of laser Doppler velocimetry and fluorometry was demonstrated in the Langley 16- by 24-Inch Water Tunnel. Comprehensive three-dimensional flow-field data were acquired from two different types of flow. First, a jet flow generated by a propulsion simulation model with a nonaxisymmetric nozzle was investigated. Flow-field data were measured at two stations downstream of the model exit. Mean axial velocity profiles were presented to show the general characteristics of the jet at two jet-to-free-stream velocity ratios and two angles of attack. Vertical profiles of axial velocity above a solid-plume jet simulator revealed more reverse flow than for the jet-off configuration. This indicates that jet flow must be provided to properly simulate off-body flow physics.

Six turbulent Reynolds stresses were calculated from the measured data. The Reynolds normal stresses were maximum near the center of the jet; the Reynolds shear stresses were generally greater in the jet shear regions. Dye concentration fluctuations were mapped in the shear region which indicated the region of free-stream and jet flow mixing. The covariance of velocity fluctuations with fluorescent dye concentration fluctuations indicated that the predominant velocity fluctuation in shear-layer mixing was the longitudinal velocity fluctuation. However, all three velocity fluctuations contributed to shear-layer mixing. From examination of the three-dimensional characteristics of the flow, the three-dimensional velocity-field data and the simultaneous predominant mechanisms in mixing were determined. This had not been accomplished previously.

The experimental results from a test of an axisymmetric forebody with a strake revealed the characteristics of a laminar vortex flow with an axial velocity deficit. The flow field generated by a strake at 50°

was compared with that at 60°. The results indicated less axial velocity deficit for the strake at 50°. Streamwise vorticity and circulation were calculated from the measured data. Comparisons between the two strake angles indicated that the vortex generated by the strake at 60° was stronger and may break down sooner than the vortex from the strake at 50°. These results are important for the determination of optimal forebody-strake configurations.

The quality of the measurement system has been studied by performing an uncertainty analysis of the experimental results. The calculated uncertainties were different for the results of the two tests. In general, uncertainties in the mean velocities varied between 1 and 7 percent of free-stream velocity.

Fluctuating velocities varied between 1 and 6 percent of reference values. The uncertainties in mean lateral velocity v were consistently greater than for the other two mean velocities. The uncertainties in the lateral velocity fluctuations v' were also generally greater than for the other two components. An independent direct measurement of v' indicated a consistently greater value than for either u' or w' in the free stream. Also, the consistently greater v and v' uncertainties resulted from the effect of resolving the measured off-axis components into the orthogonal coordinate system.

Appendix

Analysis of Experimental Uncertainties

The estimation of uncertainties in the results from measurements made by the instrument was based on standard principles outlined in the ANSI/ASME *Measurement Uncertainty. Part I—Instruments and Apparatus.* (See ref. 15.) A current book by Coleman and Steele (ref. 16) that explains the contents of the document was used in the present analysis. The concepts of bias and precision errors are defined as fixed and random errors, respectively, that occur in experimentation. The bias errors are the fixed, systematic, or constant errors that induce an offset from the true value of the quantity being measured. The precision errors are random variation or repeatability errors of the quantity being measured. The total uncertainty is the root-sum-square (RSS) combination of the bias and precision error estimates and is given by

$$U_{\text{RSS}} = \left(B^2 + P_x^2 \right)^{1/2}$$

where B is the bias error estimate and P_x is the precision limit. The precision limit is the product of the precision error estimate (precision index) and t_{95} from the statistical t distribution that gives a 95-percent confidence level to the estimate of the random precision error. For experimental sample sizes greater than 30, reference 15 recommends that $t_{95} = 2$ for 95-percent confidence estimates. The equation for the total uncertainty becomes

$$U_{\text{RSS}} = [B^2 + (2S)^2]^{1/2} \tag{A1}$$

where S is the precision error estimate or precision index.

Coleman and Steele (ref. 16) describe the propagation of uncertainty in a general uncertainty analysis. If a result r is a function of many variables x_1, x_2, x_3, ..., x_N, the uncertainty U_r in a calculated result is

$$U_r = \left[\left(\frac{\partial r}{\partial x_1} U_{x_1} \right)^2 + \left(\frac{\partial r}{\partial x_2} U_{x_2} \right)^2 + \cdots + \left(\frac{\partial r}{\partial x_N} U_{x_N} \right)^2 \right]^{1/2}$$

The U_x's are the uncertainties in the measured variables x_i. In a detailed uncertainty analysis, the bias and precision limit estimates must be propagated separately. Then the estimates are combined into the total uncertainty as in the RSS method in this case. If the bias and precision limits in the measurements of the different variables are not independent of each other, cross terms exist in the expressions for the bias and precision limits, respectively, as follows:

$$\left. \begin{aligned} B_r &= \left\{ \sum_{i=1}^{N} \left[\left(\frac{\partial r}{\partial x_i} B_{x_i} \right)^2 + \sum_{j=1}^{N} \frac{\partial r}{\partial x_i} \frac{\partial r}{\partial x_j} B_{x_i} B_{x_j} \rho_{B_{ij}} (1 - \delta_{ij}) \right] \right\}^{1/2} \\ P_r &= \left\{ \sum_{i=1}^{N} \left[\left(\frac{\partial r}{\partial x_i} P_{x_i} \right)^2 + \sum_{j=1}^{N} \frac{\partial r}{\partial x_i} \frac{\partial r}{\partial x_j} P_{x_i} P_{x_j} \rho_{P_{ij}} (1 - \delta_{ij}) \right] \right\}^{1/2} \end{aligned} \right\} \tag{A2}$$

where the ρ_{ij}'s are correlation coefficients associated with each type of error and δ_{ij} is one if $i = j$ and zero if $i \neq j$. If the error terms are independent, the ρ_{ij}'s are zero and the cross terms dissapear from equations (A2).

The bias limit for r is

$$B_r = \left[\left(\frac{\partial r}{\partial x_1} B_{x_1} \right)^2 + \left(\frac{\partial r}{\partial x_2} B_{x_2} \right)^2 + \cdots + \left(\frac{\partial r}{\partial x_N} B_{x_N} \right)^2 \right]^{1/2}$$

and the precision limit for r is

$$P_r = \left[\left(\frac{\partial r}{\partial x_1} P_{x_1} \right)^2 + \left(\frac{\partial r}{\partial x_2} P_{x_2} \right)^2 + \cdots + \left(\frac{\partial r}{\partial x_N} P_{x_N} \right)^2 \right]^{1/2}$$

where the B_x's and the P_x's are the bias and precision limits for the measured variables x_i. The tabulated results show the propagated precision error estimates (i.e., precision indices) instead of the precision limit. However, the total uncertainty contains the precision limit $P = t_{95}S$. The equation for the propagated precision error estimate is

$$S_r = \left[\left(\frac{\partial r}{\partial x_1}S_{x_1}\right)^2 + \left(\frac{\partial r}{\partial x_2}S_{x_2}\right)^2 + \cdots + \left(\frac{\partial r}{\partial x_N}S_{x_N}\right)^2\right]^{1/2}$$

where the S_x's are the estimated precision errors in the measured results.

The data acquisition program for the instrument calculates the untransformed results from the measured quantities. These results are modified by a coordinate transformation to yield final results. Therefore, the uncertainty analysis was required to take into account this transformation. The propagation of the uncertainties into the calculated results, which included coordinate transformation, was performed by a method similar to that used by Morrison et al. (See ref. 17.)

Categories of errors for the estimation of untransformed result uncertainties are given in the next section. The development of coordinate transformation equations are then described. Finally, the method for calculating uncertainties in the final transformed results will be shown. All calculated quantities were normalized by appropriate terms as shown in the tables at the end of this appendix. Instead of point by point, overall test total uncertainties were estimated for each calculated quantity. Worst-case conditions were generally used, which provided an estimated upper limit on uncertainties. Final estimated uncertainties in tables AI(a)–AI(c) are presented with two significant figure accuracy because additional significant figures would be inappropriate for such estimates.

Uncertainties in Results Calculated From Measured Quantities

Four quantities are measured by the instrument: $\Delta\nu_{u,v}$, $\Delta\nu_{u,g}$, $\Delta\nu_{u,b}$, and F_i, which are the three frequency components (yields three velocity components) and the fluorescence intensity in the laser Doppler velocimeter (LDV) coordinate system, respectively. From these untransformed measurements, the following 17 quantities are calculated: $\overline{u}$, $\overline{v}$, $\overline{w}$; $\sqrt{\overline{u'^2}}$, $\sqrt{\overline{v'^2}}$, $\sqrt{\overline{w'^2}}$; $\overline{u'u'}$, $\overline{v'v'}$, $\overline{w'w'}$; $\overline{u'v'}$, $\overline{v'w'}$, $\overline{w'u'}$; $\overline{u'c'}$, $\overline{v'c'}$, $\overline{w'c'}$; and $\overline{c}$, c'.

The elemental uncertainties in the quantities measured by the velocimeter were estimated by the methods of Patrick (ref. 9) and Meyers. (See refs. 18–20.) Three categories of errors were determined for the velocimeter: laser beam geometrical errors, processor errors, and seeding-induced errors. These errors are itemized in table AII(a). Elemental processor errors were estimated for the fluorometer. Finally, statistical errors (i.e., precision errors) were calculated and are listed in tables AII(a)–AII(c) for the untransformed results. The following sections address the various categories of error sources.

Velocimeter Errors

Laser beam geometrical errors. Seven sources of error were considered in this category. They included positioning uncertainty, beam orientation, crossbeam angle, finite probe volume, negative velocity, incomplete signal, and frequency-broadening biases. The last three errors were either not significant or not applicable to the system. See reference 9 for a more detailed explanation.

Processor errors. Six sources of error were examined in this category. These included clock synchronization, quantization, electronic noise, comparator tolerance, threshold limit, and pedestal removal filter. The last three sources were insignificant.

Seed-induced errors. Four types of errors were considered in this category. They included seed particle lag, velocity bias, flow distortion, and Bragg bias. Only the first two were significant in this study and velocity bias was only significant in the strake test. No corrections were made for velocity bias.

Fluorometer Errors

The principal fluorometer errors are attributed to the analog-to-digital (A/D) processor which digitizes the fluorescence signals and the amplifier. The A/D converter which changes the amplified analog fluorescence signal to a digital signal is a 16-bit converter with a ±5-V range. According to reference 16, the accuracy, which

implies bias, is $\pm\frac{1}{2}$ of the least significant bit (LSB). This is equivalent to one half of the digital resolution times the voltage range or

$$\Delta F = \pm\frac{1}{2}\left(\frac{10\text{ V}}{2^{16}}\right) = \pm 0.0763\text{ mV}$$

The maximum fluorescence signal processor output voltage $F_{\max}$ was about 80 mV. Therefore, the error was estimated as $\Delta F/F_{\max} \approx \pm 0.1$ percent. The maximum fluctuations in dye concentrations were about 35 percent of $F_{\max}$ (≈ 0.028 V) so that the error estimated in the fluctuations was ± 0.27 percent (0.0763 mV/0.028 V). The accuracy specified by the amplifier manufacturer was ± 0.1 percent of the signal. The total errors estimated for the fluorescence quantities were calculated by the RSS of the individual A/D converter and amplifier error estimates. The estimates are summarized in table AII(c).

Statistical Errors

Statistical errors occur because of the averaging nature of data processing in the LDV system. Finite numbers of samples are averaged at each measurement location. As a result, the true standard deviation, which indicates the level of precision error for an infinite number of samples, cannot be known. The estimate of the standard deviation is defined as

$$s = \left[\frac{1}{N-1}\sum_{i=1}^{N}(u_i - \overline{u})^2\right]^{1/2}$$

where

$$\overline{u} = \frac{1}{N}\sum_{i=1}^{N}u_i$$

and where N is the number of samples, u_i is the ith velocity sample, and $\overline{u}$ is the mean velocity at the measurement location.

If several sets of mean velocities $\overline{u}$ or mean dye concentrations $\overline{c}$ are calculated, the sample distribution of the mean values is assumed to follow a normal distribution about the parent population mean value. Therefore, the standard deviation of the normally distributed means represents the precision error in the mean (i.e., standard error of the mean) and was estimated as

$$S_u = \frac{\sqrt{\overline{u'^2}}}{\sqrt{N}}$$

or

$$S_c = \frac{\sqrt{\overline{c'^2}}}{\sqrt{N}}$$

Because the mean velocity samples are assumed to be normally distributed, the standard deviations (and thus approximately the rms velocities) are assumed statistically distributed in a chi-square manner. (See ref. 9.) However, for large sample sizes ($N > 50$), the chi-square distribution approaches a normal distribution. Therefore, the precision error in the rms turbulence velocities can be estimated as the standard error in the standard deviation (refs. 9 and 21) by

$$S_{u'} = \frac{\sqrt{\overline{u'^2}}}{\sqrt{2N}}$$

or

$$S_{c'} = \frac{\sqrt{\overline{c'^2}}}{\sqrt{2N}}$$

Patrick (ref. 9) also assumed that the Reynolds shear stresses were chi-square distributed and for large sample sizes ($N > 50$), the precision error could be estimated as

$$S_{\overline{u'v'}} = \frac{\overline{u'v'}}{\sqrt{2N}}$$

The rms velocity-concentration fluctuation correlations were treated similarly to the Reynolds shear stresses and the precision errors were estimated as

$$S_{\overline{u_i'c'}} = \frac{\overline{u_i'c'}}{\sqrt{2N}}$$

In this study, a maximum of 1000 samples were taken. At times, data rates were lower and time did not permit the acquisition of 1000 samples. Therefore, 800 samples were used in the precision error estimation calculations.

All of these estimates are for quantities in the LDV coordinate system. However, because the LDV system has a third off-axis laser beam component, the estimates were transformed into the water tunnel orthogonal coordinate system. This was accomplished by propagating the results with the coordinate transformation matrices, which are derived in the next section.

Uncertainties in Final Calculated Results

The component of velocity u_g is measured with an off-axis set of laser beams. A coordinate transformation was used to calculate the final results in the tunnel coordinates. Thus, any quantity calculated with the u_g component will be affected by this transformation—including uncertainty estimates. Therefore, the transformation equations will be derived in general and then applied to this particular system.

Coordinate Transformation

The derivation of the transformation equations follows the development of Morrison et al. (See ref. 17.) In figure A1, the axes shown as dark lines form an orthogonal X-Y-Z coordinate system. The total velocity vector defined in this system would be

$$\mathbf{U} = u\hat{\mathbf{i}} + v\hat{\mathbf{j}} + w\hat{\mathbf{k}}$$

where $\hat{\mathbf{i}}$, $\hat{\mathbf{j}}$, and $\hat{\mathbf{k}}$ represent unit vectors in the X, Y, and Z directions, respectively. This represents the velocity defined in the tunnel coordinate system. The velocity defined in the LDV coordinate system would be represented generally as

$$\mathbf{U}_{\text{LDV}} = u_v\hat{\mathbf{e}}_v + u_g\hat{\mathbf{e}}_g + u_b\hat{\mathbf{e}}_b$$

where $\hat{\mathbf{e}}_v$, $\hat{\mathbf{e}}_g$, and $\hat{\mathbf{e}}_b$ are the unit vectors in the LDV coordinate system directions. In general, the two coordinate systems have the same origin but the axes are not coincident. The relationship between the respective unit vectors can be represented by

$$\left\{ \begin{array}{c} \hat{\mathbf{e}}_v \\ \hat{\mathbf{e}}_g \\ \hat{\mathbf{e}}_b \end{array} \right\} = \left[\begin{array}{ccc} a_{11} & a_{12} & a_{13} \\ a_{21} & a_{22} & a_{23} \\ a_{31} & a_{32} & a_{33} \end{array} \right] \left\{ \begin{array}{c} \hat{\mathbf{i}} \\ \hat{\mathbf{j}} \\ \hat{\mathbf{k}} \end{array} \right\}$$

and, therefore, the relationship between the velocity vectors is

$$\left\{ \begin{array}{c} u_v \\ u_g \\ u_b \end{array} \right\} = \left[\begin{array}{ccc} a_{11} & a_{12} & a_{13} \\ a_{21} & a_{22} & a_{23} \\ a_{31} & a_{32} & a_{33} \end{array} \right] \left\{ \begin{array}{c} u \\ v \\ w \end{array} \right\}$$

Because the measurements were made in the LDV coordinate system, the inverse relationship was used as defined by

$$\left\{ \begin{array}{c} u \\ v \\ w \end{array} \right\} = \left[\begin{array}{ccc} c_{11} & c_{12} & c_{13} \\ c_{21} & c_{22} & c_{23} \\ c_{31} & c_{32} & c_{33} \end{array} \right] \left\{ \begin{array}{c} u_v \\ u_g \\ u_b \end{array} \right\} \tag{A3}$$

where

$$[c_{ij}] = [a_{ij}]^{-1}$$

The derivation of the a_{ij} matrix will be followed by the derivation of the inverse c_{ij} matrix.

One example of an LDV coordinate axis is shown by the light line in figure A1(a). Here, θ_g is the angle in the X-Y plane between the X-axis and the $\hat{\mathbf{e}}_g$ unit vector in the LDV coordinate system. The other

two orthogonal LDV components are shown in figure A1(b), rotated about the Y-axis by an angle θ_v in the X-Z plane. The angles θ_v and θ_b are the angles between the water tunnel X-axis and the measured $\hat{\mathbf{e}}_v$ and $\hat{\mathbf{e}}_b$ unit vectors, respectively; the angle θ_b will always be $\theta_v + 90°$ from the X-axis. Based on the angles between the tunnel X-axis and the LDV-measured velocity vectors, equations were derived for the corresponding unit vectors. An example of the derivation geometry is shown in figure A1(c) from which the $\hat{\mathbf{e}}_g$ unit vector was derived. The equations are

$$\hat{\mathbf{e}}_v = \hat{\mathbf{i}}\cos\theta_v + \hat{\mathbf{k}}\sin\theta_v$$

$$\hat{\mathbf{e}}_g = \hat{\mathbf{i}}\cos\theta_g - \hat{\mathbf{j}}\sin\theta_g$$

$$\hat{\mathbf{e}}_b = \hat{\mathbf{i}}\cos\theta_b + \hat{\mathbf{k}}\sin\theta_b$$

The resulting equation for velocities in terms of the a_{ij} matrix is

$$\left\{\begin{array}{c} u_v \\ u_g \\ u_b \end{array}\right\} = \left[\begin{array}{ccc} \cos\theta_v & 0 & \sin\theta_v \\ \cos\theta_g & -\sin\theta_g & 0 \\ \cos\theta_b & 0 & \sin\theta_b \end{array}\right] \left\{\begin{array}{c} u \\ v \\ w \end{array}\right\}$$

From the fact that the product of a matrix and its inverse equals the identity matrix, the terms in the c_{ij} matrix can be determined by the equation

$$\left[\begin{array}{ccc} \cos\theta_v & 0 & \sin\theta_v \\ \cos\theta_g & -\sin\theta_g & 0 \\ \cos\theta_b & 0 & \sin\theta_b \end{array}\right] \left[\begin{array}{ccc} c_{11} & c_{12} & c_{13} \\ c_{21} & c_{22} & c_{23} \\ c_{31} & c_{32} & c_{33} \end{array}\right] = \left[\begin{array}{ccc} 1 & 0 & 0 \\ 0 & 1 & 0 \\ 0 & 0 & 1 \end{array}\right]$$

Multiplication of the terms to form nine equations results in the c_{ij} solution matrix

$$\left[\begin{array}{ccc} \dfrac{\sin\theta_b}{\sin(\theta_b-\theta_v)} & 0 & \dfrac{-\sin\theta_v}{\sin(\theta_b-\theta_v)} \\[2ex] \dfrac{\sin\theta_b\cos\theta_g}{\sin\theta_g\sin(\theta_b-\theta_v)} & \dfrac{-1}{\sin\theta_g} & \dfrac{-\sin\theta_v\cos\theta_g}{\sin(\theta_b-\theta_v)\sin\theta_g} \\[2ex] \dfrac{-\cos\theta_b}{\sin(\theta_b-\theta_v)} & 0 & \dfrac{\cos\theta_v}{\sin(\theta_b-\theta_v)} \end{array}\right]$$

The above inverse matrix c_{ij} was verified by multiplying it by the original a_{ij} matrix to yield the identity matrix.

The transformation equations for the correlations between the fluctuating velocities u_i' and the fluorescence fluctuations c' were similar to those for the mean velocities. They are represented in condensed form as

$$\left[\begin{array}{c} u'c' \\ v'c' \\ w'c' \end{array}\right] = [c_{ij}] \left[\begin{array}{c} u_v'c' \\ u_g'c' \\ u_b'c' \end{array}\right]$$

From the definition of the Reynolds normal and shear stresses,

$$\overline{u'u'} = \frac{\displaystyle\sum_{i=1}^{N} u_i u_i}{N} - \overline{uu} \tag{A4}$$

and

$$\overline{u'v'} = \frac{\displaystyle\sum_{i=1}^{N} u_i v_i}{N} - \overline{uv} \tag{A5}$$

where the u_i's and v_i's are total instantaneous velocity values of the sum of the mean velocity $\overline{u}$ or $\overline{v}$ and the corresponding instantaneous fluctuating velocity u' or v'. Substitution of the matrix equations (A3) for the

u_i and $\overline{u}$ values into equation (A4) yields the following transformation equation for the $\overline{u'u'}$ Reynolds normal stress:

$$\overline{u'u'} = \left[\frac{\sum_{i=1}^{N} \begin{array}{l}(c_{11}c_{11}u_{v,i}u_{v,i} + c_{11}c_{12}u_{v,i}u_{g,i} + c_{11}c_{13}u_{v,i}u_{b,i} \\ + c_{12}c_{11}u_{g,i}u_{v,i} + c_{12}c_{12}u_{g,i}u_{g,i} + c_{12}c_{13}u_{g,i}u_{b,i} \\ + c_{13}c_{11}u_{b,i}u_{v,i} + c_{13}c_{12}u_{b,i}u_{g,i} + c_{13}c_{13}u_{b,i}u_{b,i})\end{array}}{N} \right] - \left[\begin{array}{l}(c_{11}c_{11}\overline{u_v u_v} + c_{11}c_{12}\overline{u_v u_g} + c_{11}c_{13}\overline{u_v u_b} \\ + c_{12}c_{11}\overline{u_g u_v} + c_{12}c_{12}\overline{u_g u_g} + c_{12}c_{13}\overline{u_g u_b} \\ + c_{13}c_{11}\overline{u_b u_v} + c_{13}c_{12}\overline{u_b u_g} + c_{13}c_{13}\overline{u_b u_b})\end{array} \right]$$

Similar equations were derived for the other two normal stresses and the three shear stresses but are not shown here. The end result was a set of transformation equations that is expressed as the following matrix equation:

$$\begin{bmatrix} \overline{u'u'} \\ \overline{v'v'} \\ \overline{w'w'} \\ \overline{u'v'} \\ \overline{v'w'} \\ \overline{w'u'} \end{bmatrix} = \begin{bmatrix} c_{11}c_{11} & c_{12}c_{12} & c_{13}c_{13} & 2c_{11}c_{12} & 2c_{11}c_{13} & 2c_{12}c_{13} \\ c_{21}c_{21} & c_{22}c_{22} & c_{23}c_{23} & 2c_{21}c_{22} & 2c_{21}c_{23} & 2c_{22}c_{23} \\ c_{31}c_{31} & c_{32}c_{32} & c_{33}c_{33} & 2c_{31}c_{32} & 2c_{31}c_{33} & 2c_{32}c_{33} \\ c_{11}c_{21} & c_{12}c_{22} & c_{13}c_{23} & c_{11}c_{22} + c_{12}c_{21} & c_{11}c_{23} + c_{13}c_{21} & c_{12}c_{23} + c_{13}c_{22} \\ c_{21}c_{31} & c_{22}c_{32} & c_{23}c_{33} & c_{21}c_{32} + c_{22}c_{31} & c_{21}c_{33} + c_{23}c_{31} & c_{22}c_{33} + c_{23}c_{32} \\ c_{31}c_{11} & c_{32}c_{12} & c_{33}c_{13} & c_{31}c_{12} + c_{32}c_{11} & c_{31}c_{13} + c_{33}c_{11} & c_{32}c_{13} + c_{33}c_{12} \end{bmatrix} \begin{bmatrix} \overline{u'_v u'_v} \\ \overline{u'_g u'_g} \\ \overline{u'_b u'_b} \\ \overline{u'_v u'_g} \\ \overline{u'_v u'_b} \\ \overline{u'_g u'_b} \end{bmatrix}$$

For the LDV coordinate system under study, the following quantities are defined:

$$\theta_v = 0°$$

$$\theta_b = 90°$$

$$\theta_g = 32.037° \,(\text{in}\,H_2O)$$

This leads to the definitions of the two transformation matrices as

$$[c_{ij}] = \begin{bmatrix} 1 & 0 & 0 \\ \frac{\cos\theta_g}{\sin\theta_g} & -\frac{1}{\sin\theta_g} & 0 \\ 0 & 0 & 1 \end{bmatrix}$$

and of the Reynolds normal and shear stresses as

$$\begin{bmatrix} 1 & 0 & 0 & 0 & 0 & 0 \\ \left(\frac{\cos\theta_g}{\sin\theta_g}\right)^2 & \left(\frac{-1}{\sin\theta_g}\right)^2 & 0 & \frac{-2\cos\theta_g}{\sin^2\theta_g} & 0 & 0 \\ 0 & 0 & 1 & 0 & 0 & 0 \\ \frac{\cos\theta_g}{\sin\theta_g} & 0 & 0 & \frac{-1}{\sin\theta_g} & 0 & 0 \\ 0 & 0 & 0 & 0 & \frac{\cos\theta_g}{\sin\theta_g} & \frac{-1}{\sin\theta_g} \\ 0 & 0 & 0 & 0 & 1 & 0 \end{bmatrix}$$

The equations for the transformed results are

$$\left.\begin{array}{l} \overline{u} = \overline{u_v} \\[2mm] \overline{v} = \overline{u_v}\dfrac{\cos\theta_g}{\sin\theta_g} - \dfrac{\overline{u_g}}{\sin\theta_g} \\[4mm] \overline{w} = \overline{u_b} \end{array}\right\} \tag{A6}$$

$$\left.\begin{array}{l} \overline{u'c'} = \overline{u_v'c'} \\[2mm] \overline{v'c'} = \overline{u_v'c'}\dfrac{\cos\theta_g}{\sin\theta_g} - \dfrac{\overline{u_g'c'}}{\sin\theta_g} \\[4mm] \overline{w'c'} = \overline{u_b'c'} \end{array}\right\} \tag{A7}$$

$$\left.\begin{array}{l} \overline{u'u'} = \overline{u_v'u_v'} \\[2mm] \overline{v'v'} = \left(\dfrac{\cos\theta_g}{\sin\theta_g}\right)^2 \overline{u_v'u_v'} + \dfrac{1}{\sin^2\theta_g}\overline{u_g'u_g'} - \dfrac{2\cos\theta_g}{\sin^2\theta_g}\overline{u_v'u_g'} \\[4mm] \overline{w'w'} = \overline{u_b'u_b'} \end{array}\right\} \tag{A8}$$

$$\left.\begin{array}{l} \overline{u'v'} = \left(\dfrac{\cos\theta_g}{\sin\theta_g}\right)\overline{u_v'u_v'} - \dfrac{1}{\sin\theta_g}\overline{u_v'u_g'} \\[4mm] \overline{v'w'} = \left(\dfrac{\cos\theta_g}{\sin\theta_g}\right)\overline{u_v'u_b'} - \dfrac{1}{\sin\theta_g}\overline{u_g'u_b'} \\[4mm] \overline{w'u'} = \overline{u_b'u_b'} \end{array}\right\} \tag{A9}$$

where

$$u_{\mathrm{rms}} = \sqrt{\overline{u'u'}}$$
$$v_{\mathrm{rms}} = \sqrt{\overline{v'v'}}$$
$$w_{\mathrm{rms}} = \sqrt{\overline{w'w'}}$$

Of course, because the fluorescent dye concentration c and fluctuation c' are scalar quantities, they are transformed without modification to the final results.

Application of Uncertainty Propagation Into Calculated Results

By reference to the transformation equations (A6) for the mean velocities, the equations for the propagation of the bias limits and precision indices (i.e., precision errors) can be derived. Because

$$\overline{u} = \overline{u_v} \qquad \overline{w} = \overline{u_b}$$

$$\frac{\partial\overline{u}}{\partial\overline{u_v}} = 1 \qquad \frac{\partial\overline{w}}{\partial\overline{u_b}} = 1$$

and, for example,

$$B_{\overline{u}} = \left[\left(\frac{\partial\overline{u}}{\partial\overline{u_v}}B_{\overline{u_v}}\right)^2\right]^{1/2}$$

21

then the propagated bias limits and precision errors for the u and w mean velocities are equal to those for the measured quantities. That is,

$$B_{\overline{u}} = B_{\overline{u_v}} \qquad S_{\overline{u}} = S_{\overline{u_v}} \qquad B_{\overline{w}} = B_{\overline{u_b}} \qquad S_{\overline{w}} = S_{\overline{u_b}}$$

For the on-axis velocity component v, the bias equation from equations (A2) becomes

$$B_{\overline{v}}^2 = \left(\frac{\partial \overline{v}}{\partial \overline{u_v}} B_{\overline{u_v}} \right)^2 + \left(\frac{\partial \overline{v}}{\partial \overline{u_g}} B_{\overline{u_g}} \right)^2 + \left(\frac{\partial \overline{v}}{\partial \theta_g} B_{\theta_g} \right)^2 + \frac{\partial \overline{v}}{\partial \overline{u_v}} \frac{\partial \overline{v}}{\partial \overline{u_g}} \rho_{u_v u_g} B_{\overline{u_v}} B_{\overline{u_g}} + \cdots$$

The bias in θ_g in this study was $\pm 0.1°$ (± 0.0017 rad). The errors in the measurements of u_v, u_g, and θ_g are assumed to be independent. The cross terms drop out ($\rho_{u_v u_g} = \rho_{u_g \theta_g} = \rho_{u_v \theta_g} = 0$), which results in

$$B_{\overline{v}} = \left[\left(\frac{\cos \theta_g}{\sin \theta_g} B_{\overline{u_v}} \right)^2 + \left(-\frac{1}{\sin \theta_g} B_{\overline{u_g}} \right)^2 + \left(-u_v \csc^2 \theta_g + u_g \csc \theta_g \cot \theta_g \right)^2 B_{\theta_g}^2 \right]^{1/2} \tag{A10}$$

Similarly, for the precision error,

$$S_{\overline{v}} = \left[\left(\frac{\cos \theta_g}{\sin \theta_g} S_{\overline{u_v}} \right)^2 + \left(-\frac{1}{\sin \theta_g} S_{\overline{u_g}} \right)^2 \right]^{1/2}$$

There is no precision error in θ_g; the error in θ_g is a bias error.

As before, the total uncertainty is then calculated as

$$U_{\overline{u}} = \left[B_{\overline{u}}^2 + (2 S_{\overline{u}})^2 \right]^{1/2}$$

$$U_{\overline{v}} = \left[B_{\overline{v}}^2 + (2 S_{\overline{v}})^2 \right]^{1/2}$$

$$U_{\overline{w}} = \left[B_{\overline{w}}^2 + (2 S_{\overline{w}})^2 \right]^{1/2}$$

The bias limits and precision errors for the Reynolds normal stresses were calculated from the transformation equations (A8). Again, because

$$\overline{u'u'} = \overline{u_v' u_v'} \qquad \overline{w'w'} = \overline{u_b' u_b'}$$

the bias limits and precision estimates were derived as

$$B_{\overline{u'u'}} = B_{\overline{u_v' u_v'}} \qquad S_{\overline{u'u'}} = S_{\overline{u_v' u_v'}} \qquad B_{\overline{w'w'}} = B_{\overline{u_b' u_b'}} \qquad S_{\overline{w'w'}} = S_{\overline{u_b' u_b'}}$$

From the formulas for the Reynolds stresses,

$$\left. \begin{array}{l} B_{\overline{u_v' u_v'}} = B_{\overline{u_g' u_g'}} = B_{\overline{u_b' u_b'}} = 0 \\[2mm] B_{\overline{u_v' u_g'}} = B_{\overline{u_g' u_b'}} = B_{\overline{u_b' u_v'}} = 0 \end{array} \right\} \tag{A11}$$

This implies that the errors in the Reynolds stresses are strictly statistical precision errors before they are transformed into the tunnel coordinate system.

The errors in the measurements of $\overline{u_v' u_v'}$ and $\overline{u_v' u_g'}$ or $\overline{u_g' u_g'}$ and $\overline{u_v' u_g'}$ may not be independent which would generate cross terms in the error equations. However, the extent of dependence is not known; also, the magnitude and sign of the correlation coefficients of the cross terms are not known. Therefore, the measurement

22

errors in $\overline{u_v' u_v'}$, $\overline{u_g' u_g'}$, $\overline{u_v' u_g'}$, and θ_g are assumed to be independent for this quantity, which eliminates cross terms. The bias limit in $\overline{v'v'}$ can be estimated from

$$B_{\overline{v'v'}}^2 = \left(\frac{\partial \overline{v'v'}}{\partial \overline{u_v' u_v'}} B_{\overline{u_v' u_v'}} \right)^2 + \left(\frac{\partial \overline{v'v'}}{\partial \overline{u_g' u_g'}} B_{\overline{u_g' u_g'}} \right)^2 + \left(\frac{\partial \overline{v'v'}}{\partial \overline{u_v' u_g'}} B_{\overline{u_v' u_g'}} \right)^2 + \left(\frac{\partial \overline{v'v'}}{\partial \theta_g} B_{\theta_g} \right)^2$$

From the transformation equations (A8) for the $\overline{v'v'}$ Reynolds normal stress, the bias limit is

$$B_{\overline{v'v'}}^2 = \left[\left(\frac{\cos \theta_g}{\sin \theta_g} \right)^2 B_{\overline{u_v' u_v'}} \right]^2 + \left(\frac{1}{\sin^2 \theta_g} B_{\overline{u_g' u_g'}} \right)^2 + \left(\frac{-2 \cos \theta_g}{\sin^2 \theta_g} B_{\overline{u_v' u_g'}} \right)^2$$

$$+ \left[\frac{-2 \cos \theta_g}{\sin^3 \theta_g} \left(\overline{u_v' u_v'} + \overline{u_g' u_g'} \right) + 2 \overline{u_v' u_g'} \csc \theta_g (2 \cot^2 \theta_g + 1) \right]^2 B_{\theta_g}^2$$

From equations (A11), the first three terms are zero and the bias is a function only of the error in θ_g. The precision index has a similar form of

$$S_{\overline{v'v'}}^2 = \left[\left(\frac{\cos \theta_g}{\sin \theta_g} \right)^2 S_{\overline{u_v' u_v'}} \right]^2 + \left(\frac{1}{\sin^2 \theta_g} S_{\overline{u_g' u_g'}} \right)^2 + \left(\frac{-2 \cos \theta_g}{\sin^2 \theta_g} S_{\overline{u_v' u_g'}} \right)^2$$

where $S_{\overline{u_v' u_g'}}$ is the measured shear stress precision error estimate.

The transformed fluctuating (rms) velocities are calculated as the square root of the transformed Reynolds normal stresses. Therefore,

$$\sqrt{\overline{u'^2}} = u_{\text{rms}} = \sqrt{\overline{u'u'}} = \sqrt{\overline{u_v' u_v'}} = u_{v_{\text{rms}}}$$

and

$$\sqrt{\overline{w'^2}} = w_{\text{rms}} = \sqrt{\overline{u_b' u_b'}} = u_{b_{\text{rms}}}$$

Similar to the mean velocities, the bias and precision errors are

$$B_{u_{\text{rms}}} = B_{u_{v_{\text{rms}}}} \qquad B_{w_{\text{rms}}} = B_{u_{b_{\text{rms}}}} \qquad S_{u_{\text{rms}}} = S_{u_{v_{\text{rms}}}} \qquad S_{w_{\text{rms}}} = S_{u_{b_{\text{rms}}}}$$

From the transformation equations (A8) and by noting that $u_{v_{\text{rms}}}^2 = \overline{u_v' u_v'}$, and $u_{g_{\text{rms}}}^2 = \overline{u_g' u_g'}$, the fluctuating velocity v_{rms} is

$$v_{\text{rms}} = \sqrt{\overline{v'v'}} = \left[\left(\frac{\cos \theta_g}{\sin \theta_g} \right)^2 u_{v_{\text{rms}}}^2 + \frac{1}{\sin^2 \theta_g} u_{g_{\text{rms}}}^2 - \frac{2 \cos \theta_g}{\sin^2 \theta_g} \overline{u_v' u_g'} \right]^{1/2}$$

The equation for the bias limit is derived from

$$B_{v_{\text{rms}}}^2 = \left(\frac{\partial v_{\text{rms}}}{\partial u_{v_{\text{rms}}}} B_{u_{v_{\text{rms}}}} \right)^2 + \left(\frac{\partial v_{\text{rms}}}{\partial u_{g_{\text{rms}}}} B_{u_{g_{\text{rms}}}} \right)^2 + \left(\frac{\partial v_{\text{rms}}}{\partial \overline{u_v' u_g'}} B_{\overline{u_v' u_g'}} \right)^2 + \left(\frac{\partial v_{\text{rms}}}{\partial \theta_g} B_{\theta_g} \right)^2$$

Insertion of the appropriate terms in the above equation and algebraic manipulation yield

$$B_{v_{\text{rms}}}^2 = \left[\left(\frac{\cos \theta_g}{\sin \theta_g} \right)^2 \frac{u_{v_{\text{rms}}}}{v_{\text{rms}}} B_{u_{v_{\text{rms}}}} \right]^2 + \left(\frac{B_{u_{g_{\text{rms}}}}}{\sin^2 \theta_g} \frac{u_{g_{\text{rms}}}}{v_{\text{rms}}} \right)^2 + \left(\frac{-\cos \theta_g}{\sin^2 \theta_g} \frac{B_{\overline{u_v' u_g'}}}{v_{\text{rms}}} \right)^2$$

$$+ \left[\frac{-\cos \theta_g}{\sin^3 \theta_g} \left(u_{v_{\text{rms}}}^2 + u_{g_{\text{rms}}}^2 \right) + \overline{u_v' u_g'} \csc \theta_g (2 \cot^2 \theta_g + 1) \right]^2 \left(\frac{B_{\theta_g}}{v_{\text{rms}}} \right)^2$$

where the third term is zero.

The precision errors are

$$S_{v_{\text{rms}}}^2 = \left[\left(\frac{\cos\theta_g}{\sin\theta_g}\right)^2 \frac{u_{v_{\text{rms}}}}{v_{\text{rms}}} S_{u_{v_{\text{rms}}}}\right]^2 + \left(\frac{S_{u_{g_{\text{rms}}}}}{\sin^2\theta_g}\frac{u_{g_{\text{rms}}}}{v_{\text{rms}}}\right)^2 + \left(\frac{-\cos\theta_g}{\sin^2\theta_g}\frac{S_{\overline{u_v'u_g'}}}{v_{\text{rms}}}\right)^2$$

The uncertainty analysis for the Reynolds shear stresses was based on the transformation equations (A9). In this case, the velocity measurements from the same particle were required for correlation of velocity fluctuations. Therefore, each of the $\overline{u'v'}$ and $\overline{v'w'}$ stresses had a third cross term in their expressions for bias limits and precision errors. The errors were assumed to be perfectly positive-correlated and the correlation coefficients were set equal to one. The equations for the bias limits are as follows:

$$B_{\overline{u'v'}}^2 = \left(-\overline{u_v'u_v'}\csc^2\theta_g + \overline{u_v'u_g'}\csc\theta_g\cot\theta_g\right)^2 B_{\theta_g}^2$$

$$+ \left(\frac{\cos\theta_g}{\sin\theta_g}B_{\overline{u_v'u_v'}}\right)^2 + \left(\frac{-B_{\overline{u_v'u_g'}}}{\sin\theta_g}\right)^2 + \left(\frac{\cos\theta_g}{\sin\theta_g}\right)\left(\frac{-1}{\sin\theta_g}\right)B_{\overline{u_v'u_v'}}B_{\overline{u_v'u_g'}}$$

$$B_{\overline{v'w'}}^2 = \left(-\overline{u_v'u_b'}\csc^2\theta_g + \overline{u_g'u_b'}\csc\theta_g\cot\theta_g\right)^2 B_{\theta_g}^2$$

$$+ \left(\frac{\cos\theta_g}{\sin\theta_g}B_{\overline{u_v'u_b'}}\right)^2 + \left(\frac{-B_{\overline{u_g'u_b'}}}{\sin\theta_g}\right)^2 + \left(\frac{\cos\theta_g}{\sin\theta_g}\right)\left(\frac{-1}{\sin\theta_g}\right)B_{\overline{u_v'u_b'}}B_{\overline{u_g'u_b'}}$$

By application of equations (A11), only the first term in each equation is nonzero. Also,

$$B_{\overline{w'u'}} = B_{\overline{u_v'u_b'}} = 0$$

The precision errors are calculated as follows:

$$S_{\overline{u'v'}}^2 = \left(\frac{\cos\theta_g}{\sin\theta_g}S_{\overline{u_v'u_v'}}\right)^2 + \left(\frac{-S_{\overline{u_v'u_g'}}}{\sin\theta_g}\right)^2 + \left(\frac{\cos\theta_g}{\sin\theta_g}\right)\left(\frac{-1}{\sin\theta_g}\right)S_{\overline{u_v'u_v'}}S_{\overline{u_v'u_g'}}$$

$$S_{\overline{v'w'}}^2 = \left(\frac{\cos\theta_g}{\sin\theta_g}S_{\overline{u_v'u_b'}}\right)^2 + \left(\frac{-S_{\overline{u_g'u_b'}}}{\sin\theta_g}\right)^2 + \left(\frac{\cos\theta_g}{\sin\theta_g}\right)\left(\frac{-1}{\sin\theta_g}\right)S_{\overline{u_v'u_b'}}S_{\overline{u_g'u_b'}}$$

and

$$S_{\overline{w'u'}} = S_{\overline{u_v'u_b'}}$$

Fluorescent dye concentration c is not measured directly but is calculated from the following equation for the fluorescence intensity given previously:

$$F = K\Phi I_0 \varepsilon bc$$

where b represents the size of the sample volume and the other terms are as defined before. The solution for the concentration is

$$c = \frac{F}{K\Phi I_0 \varepsilon b}$$

The bias limit for the concentration is calculated from

$$B_c = \left[\left(\frac{\partial c}{\partial F}B_F\right)^2 + \left(\frac{\partial c}{\partial I_0}B_{I_0}\right)^2 + \left(\frac{\partial c}{\partial b}B_b\right)^2\right]^{1/2}$$

with the assumption that the measurements of F, I_0, and b are independent and the contributions from K, Φ, and ε can be neglected. The resulting equation for the bias limit is

$$B_c = c\left[\left(\frac{B_F}{F}\right)^2 + \left(\frac{B_{I_0}}{I_0}\right)^2 + \left(\frac{B_b}{b}\right)^2\right]^{1/2}$$

For the tests discussed in this paper, the variations in laser intensity were assumed to be small enough to be ignored during the sample period. Also, the sample volume was assumed to be completely filled with dye during the sample period and to not vary in size. This results in an equivalent relationship between the fractional bias limits for concentration and fluorescence intensity. From the above assumptions, the relative bias in the concentration results is proportional to the relative bias in the fluorescence measurements and either

$$\frac{B_c}{c} = \frac{B_F}{F}$$

or

$$B_c = \frac{B_F}{K\Phi I_0 \varepsilon b}$$

Because the correlations of velocity and dye concentration fluctuations were transformed exactly as the mean velocities were, their transformation equations are similar to equations (A7). From the formulas for the correlations, the bias errors in the $u'c'$ and $w'c'$ correlations are zero. With the assumption of independent measurement errors in $\overline{u'_v c'}$, $\overline{u'_g c'}$ and θ_g, the resulting equations for bias limits are

$$B_{\overline{u'c'}} = B_{\overline{u'_v c'}} = B_{\overline{w'c'}} = B_{\overline{u'_b c'}} = 0$$

and

$$B^2_{\overline{v'c'}} = \left(\frac{\cos\theta_g}{\sin\theta_g}B_{\overline{u'_v c'}}\right)^2 + \left(\frac{-B_{\overline{u'_g c'}}}{\sin\theta_g}\right)^2 + \left(-\overline{u'_v c'}\csc^2\theta_g + \overline{u'_g c'}\csc\theta_g\cot\theta_g\right)^2 B^2_{\theta_g}$$

where only the last term is nonzero. Similarly, for the precision errors,

$$S_{\overline{u'c'}} = S_{\overline{u'_v c'}} \qquad S_{\overline{w'c'}} = S_{\overline{u'_b c'}}$$

and

$$S^2_{\overline{v'c'}} = \left(\frac{\cos\theta_g}{\sin\theta_g}S_{\overline{u'_v c'}}\right)^2 + \left(\frac{-S_{\overline{u'_g c'}}}{\sin\theta_g}\right)^2$$

An example calculation of the positive bias error in $\overline{v}$ for the jet test is presented here. Recall that equation (A10) for this error is

$$B_{\overline{v}} = \left[\left(\frac{\cos\theta_g}{\sin\theta_g}B_{\overline{u_v}}\right)^2 + \left(-\frac{1}{\sin\theta_g}B_{\overline{u_g}}\right)^2 + \left(-u_v\csc^2\theta_g + u_g\csc\theta_g\cot\theta_g\right)^2 B^2_{\theta_g}\right]^{1/2}$$

All velocities used in this equation were nondimensionalized by U_∞. The angle $\theta_g = 32.037°$ with a bias of $\pm 0.1°$ (± 0.0017 rad). Values of $u_v/U_\infty = 1.5$ and $u_g/U_\infty = 0.05$ were used. The bias in $\overline{u_v}/U_\infty$ is 0.0207 and -0.0213 from table AII(a) and includes contributions primarily from laser beam geometry and particle lag errors; the bias in $\overline{u_g}/U_\infty$ is 0.0216 and -0.0221 from the same sources of error. The positive bias errors in $\overline{u_v}/U_\infty$ and $\overline{u_g}/U_\infty$ result in the three squared terms of equation (A10) being equal to 0.00109, 0.00166, and 0.00008, respectively. By RSS methods, the total positive bias error in $\overline{v}/U_\infty$ is 0.0532. Clearly, the first two terms contribute the most to this error because they are predominately influenced by the error in the crossbeam angle measurement. This result is typical of most systems and greater accuracy in crossbeam angle measurement will have the greatest effect in reducing the bias error.

This concludes the discussion of the propagation of uncertainty for the basic calculated quantities. All of the transformed final results are summarized in tables AI(a)–AI(c). All transformed quantities were normalized

by the appropriate terms as shown in the tables. The next section describes the use of the total uncertainties in mean velocities in the calculation of the uncertainties in streamwise vorticity and circulation from the stra ke test.

Estimates of Uncertainty in Vorticity and Circulation

The calculations of streamwise vorticity and circulation were performed with the results of the study of the axisymmetric forebody with a strake. The derivations of equations for vorticity and circulation were based on references 22–24. The following general equations are used to formulate uncertainty estimates for the calculations of streamwise vorticity and circulation.

Errors in vorticity calculations. The general equation for the streamwise vorticity and the discretized approximation is

$$\omega_x = \left(\frac{\partial w}{\partial y} - \frac{\partial v}{\partial z}\right) \approx \frac{\Delta w}{\Delta y} - \frac{\Delta v}{\Delta z}$$

The total estimated uncertainties in velocities were the combined bias and precision error. They were combined into an alternate bias error for calculation of the error in vorticity. With the assumption that v and w, and y and z were independently measured, an analysis based on total uncertainty values of the components of vorticity yields the error

$$B_{\omega_x}^2 = \left[\frac{\partial \omega_x}{\partial \left(\frac{\Delta w}{\Delta y}\right)} B_{\frac{\Delta w}{\Delta y}}\right]^2 + \left[\frac{\partial \omega_x}{\partial \left(\frac{\Delta v}{\Delta z}\right)} B_{\frac{\Delta v}{\Delta z}}\right]^2$$

The following equation was derived for the error in streamwise vorticity:

$$B_{\omega_x}^2 = \left(\frac{1}{\Delta y}\sqrt{2}B_w\right)^2 + \left(\frac{1}{\Delta z}\sqrt{2}B_v\right)^2 + \left(-\frac{\Delta w}{\Delta y^2}\sqrt{2}B_y\right)^2 + \left(-\frac{\Delta v}{\Delta z^2}\sqrt{2}B_z\right)^2$$

To obtain the worst-case estimates of uncertainty, the minimum spacing of Δy and Δz for the grid was used. The largest absolute values for the uncertainties in the v and w mean velocities were used. The calculations yielded the following result for the uncertainty in streamwise vorticity:

$$B_{\omega_x}^2 = 6.687 + 0.00028$$

$$B_{\omega_x}^2 = 2.59 \sec^{-1}$$

Clearly, the first-order terms in Δy and Δz are the dominant terms and the effect of the error in measurement position is small for this calculation. Because the uncertainties in mean velocities are greatest in high-velocity gradient regions, the level of error in ω_x is probably less in lower ω_x regions where velocity gradients diminish. (See fig. 49.)

Error in circulation calculations. Circulation was calculated by two methods: a line integral of the velocity around a closed path (i.e., rectangular cell) and an area integral of the vorticity, which resulted in circulation values that were within 0.04 percent. The equations and their approximations for each method, respectively, are

$$\Gamma = \oint_C v\,dy + w\,dz \approx \sum_{i=1}^{4} v_i\,\Delta y + w_i\,\Delta z$$

$$\Gamma = \int_A \omega_x\,dS \approx \omega_{\text{cell}}\,\Delta y\,\Delta z$$

The error in the calculated circulation for the line integral method can be estimated as follows:

$$B_\Gamma^2 = \sum_{i=1}^{4}\left[\left(\frac{\partial\Gamma}{\partial v_i}B_{v_i}\right)^2 + \left(\frac{\partial\Gamma}{\partial\Delta y}B_{\Delta y}\right)^2 + \left(\frac{\partial\Gamma}{\partial w_i}B_{w_i}\right)^2 + \left(\frac{\partial\Gamma}{\partial\Delta z}B_{\Delta z}\right)^2\right]$$

$$B_\Gamma^2 = 4\left[(\Delta y\,B_v)^2 + (v\,B_{\Delta y})^2 + (\Delta z\,B_w)^2 + (w B_{\Delta z})^2\right]$$

From typical peak values of v and w and the values defined in the previous section, the following uncertainty in the circulation was calculated:

$$B_\Gamma = 0.0124\,\text{in}^2/\sec$$

The error in the calculated circulation for the area integral method can be estimated as follows:

$$B_\Gamma^2 = \left(\frac{\partial\Gamma}{\partial\omega}B_{\omega_x}\right)^2 + \left(\frac{\partial\Gamma}{\partial\Delta y}B_{\Delta y}\right)^2 + \left(\frac{\partial\Gamma}{\partial\Delta z}B_{\Delta z}\right)^2$$

$$B_\Gamma^2 = (\Delta y\,\Delta z\,B_{\omega_x})^2 + (\omega_x\,\Delta z\,B_{\Delta y})^2 + (\omega_x\,\Delta y\,B_{\Delta z})^2$$

From a peak vorticity value and other values previously defined, the uncertainty in circulation was estimated as

$$B_\Gamma = 0.0088\,\text{in}^2/\sec$$

Analysis of Uncertainty Results

The significance of the final uncertainty results can be examined by comparing them with reference values. The reference value for all fluctuating quantities was $0.53U_\infty$ and was determined by calculating the averages of the mean plus standard deviations of the velocity fluctuations u', v', and w' from the jet test. The uncertainties in the mean values are already referenced to the free-stream velocity and are shown in table AI(a). The remaining uncertainty results relative to $0.53U_\infty$ (or $(0.53U_\infty)^2$ for stress terms) are given as percentages in table AIII. The results from the strake test are significantly lower because of much lower turbulence values (≈ 11 percent of U_∞). The velocity-concentration quantities were referenced to $0.53U_\infty$ and $0.1\,\overline{c}_{\max}$ ($\overline{c}_{\max} = 45$ mV).

All quantities associated with the on-axis v component (including mean values in table AI(a)) had the greatest uncertainties because of the resolution of the off-axis geometry into the on-axis v-component direction. This system has been analyzed by Neti and Clark, Yanta and Ausherman, and Bell, Rodman, and Mehta. (See refs. 25, 26, and 27, respectively.) They formulated a relation for the error in the on-axis velocity component as a function of the off-axis angle, an assumed fractional uncertainty in measured components, and the ratio of on-axis velocity to measured velocity. When the velocity ratio is small, the errors in on-axis velocity can be extremely large (>100 percent). This implies that the errors estimated on a point-by-point basis may be considerably greater or less than the values estimated in this study. However, the error values given in the tables are a reasonable estimate of the orders of magnitude.
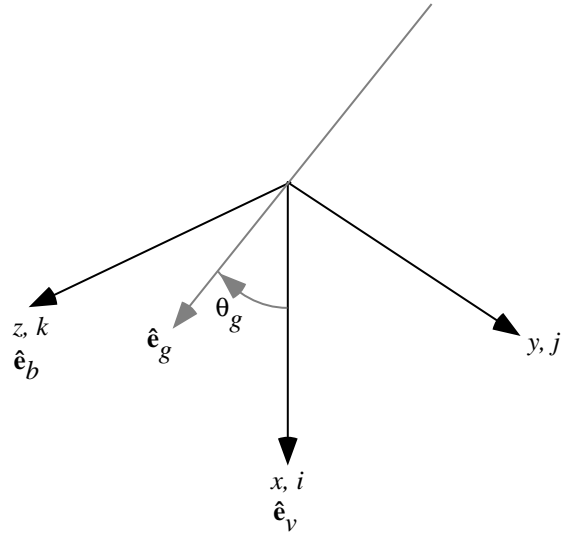
(a) Nonorthogonal component.
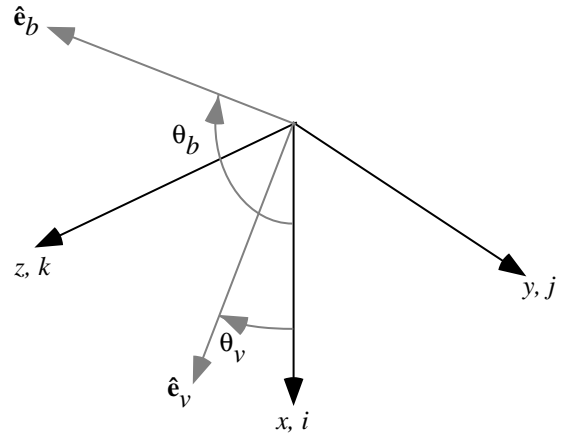
(b) Orthogonal components.
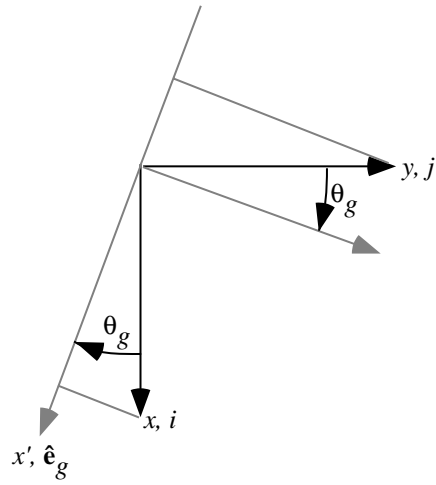
(c) Unit vector $\hat{\mathbf{e}}_{\mathbf{g}}$ derivation.

Figure A1. Coordinate system axes.

Table AI. Uncertainty Estimates for Transformed Results

(a) Mean and fluctuating (rms) velocities, $U_\infty = 3$ in/sec

Error	$\dfrac{\overline{u}}{U_\infty}$	$\dfrac{\overline{v}}{U_\infty}$	$\dfrac{\overline{w}}{U_\infty}$	$\dfrac{\sqrt{\overline{u'^2}}}{U_\infty}$	$\dfrac{\sqrt{\overline{v'^2}}}{U_\infty}$	$\dfrac{\sqrt{\overline{w'^2}}}{U_\infty}$
Jet test						
Bias	$+0.0207$ -0.0213	$+0.0532$ -0.0545	$+0.0129$ -0.0138	±0.00504	±0.0154	±0.00389
Precision	±0.00580	±0.0198	±0.00456	±0.00410	±0.0150	±0.00322
Total uncertainty	±0.024	$+0.066$ -0.067	±0.016	±0.0096	±0.034	±0.0075
Strake test						
Bias	$+0.0101$ -0.0112	$+0.0254$ -0.0281	$+0.00822$ -0.00957	±0.00195	±0.0119	±0.00441
Precision	±0.00168	±0.00888	±0.00110	±0.00119	±0.00600	±0.000775
Total uncertainty	$+0.011$ -0.012	$+0.031$ -0.033	$+0.0085$ -0.0098	±0.0031	±0.017	±0.0047

(b) Reynolds normal stresses, $U_\infty = 3$ in/sec

Error	$\dfrac{\overline{u'u'}}{U_\infty^2}$	$\dfrac{\overline{v'v'}}{U_\infty^2}$	$\dfrac{\overline{w'w'}}{U_\infty^2}$
Jet test			
Bias	0	±0.00027	0
Precision	±0.00067	±0.00728	±0.00042
Total uncertainty	±0.00067	±0.015	±0.00042
Strake test			
Bias	0	±0.00005	0
Precision	±0.00006	±0.00149	±0.00002
Total uncertainty	±0.00006	±0.0030	±0.00002

(c) Reynolds shear stresses and fluorescence-related data, $U_\infty = 3$ in/sec

Error	$\dfrac{\overline{u'v'}}{U_\infty^2}$	$\dfrac{\overline{v'w'}}{U_\infty^2}$	$\dfrac{\overline{w'u'}}{U_\infty^2}$	$\dfrac{\overline{u'c'}}{U_\infty c_{max}}$	$\dfrac{\overline{v'c'}}{U_\infty c_{max}}$	$\dfrac{\overline{w'c'}}{U_\infty c_{max}}$	$\dfrac{c}{c_{max}}$	$\dfrac{c'}{c_{max}}$
Jet test								
Bias	±0.0000728	±0.0000622	0	0	±0.0000238	0	±0.0014	±0.0029
Precision	±0.00110	±0.00050	±0.00036	±0.00015	±0.00028	±0.00005	±0.00346	±0.00244
Total uncertainty	±0.0022	±0.0010	±0.00036	±0.00015	±0.00056	±0.00005	±0.0071	±0.0057
Strake test								
Bias	±0.0000029	±0.0000012	0				±0.0014	±0.0029
Precision	±0.00012	±0.000066	±0.00002				±0.00461	±0.00326
Total uncertainty	±0.00024	±0.00013	±0.00002				±0.0093	±0.0071

Table AII. Uncertainty Estimates for Untransformed Results

(a) Mean and fluctuating (rms) velocities, $U_\infty = 3$ in/sec

[Jet test]

Error	$\dfrac{\overline{u_v}}{U_\infty}$	$\dfrac{\overline{u_g}}{U_\infty}$	$\dfrac{\overline{u_b}}{U_\infty}$	$\dfrac{\sqrt{\overline{u_v'^2}}}{U_\infty}$	$\dfrac{\sqrt{\overline{u_g'^2}}}{U_\infty}$	$\dfrac{\sqrt{\overline{u_b'^2}}}{U_\infty}$
Beam geometry						
Position uncertainty	±0.00364	≈0	≈0	±0.00020	±0.00031	±0.00015
Beam orientation	±0.00197	±0.0128	±0.0128	±0.00154	±0.00116	±0.00168
Crossbeam angle	±0.0195	±0.0174	±0.00130	±0.00107	±0.00170	±0.00084
Finite probe volume	±0.00667	0	0	±0.00467	±0.00708	±0.00338
Processor errors						
Clock synchronization	0.0000075	0.0000019	0.0000025	0.0000037	0.0000013	0.0000010
Quantization	≈0	≈0	≈0	≈0	≈0	≈0
Electronic noise	0.000155	0.000262	0.000062	0.0000016	0.0000057	0.0000002
Seed-induced errors						
Particle lag	-0.0049	-0.0049	-0.0049	0	0	0
Velocity bias[1]						
Totals						
Total bias	$+0.0207$ -0.0213	$+0.0216$ -0.0221	$+0.0129$ -0.0132	±0.00504	±0.00738	±0.00389
Precision errors	±0.00580	±0.00927	±0.00456	±0.00410	±0.00655	±0.00322
Total uncertainty	$+0.0237$ -0.0242	$+0.0285$ -0.0288	$+0.0158$ -0.0165	±0.00962	±0.0150	±0.00752

[1]Not computed.

Table AII. Continued

(a) Concluded

[Strake test]

Error	$\dfrac{\overline{u_v}}{U_\infty}$	$\dfrac{\overline{u_g}}{U_\infty}$	$\dfrac{\overline{u_b}}{U_\infty}$	$\dfrac{\sqrt{\overline{u_v'^2}}}{U_\infty}$	$\dfrac{\sqrt{\overline{u_g'^2}}}{U_\infty}$	$\dfrac{\sqrt{\overline{u_b'^2}}}{U_\infty}$
Beam geometry						
Position uncertainty	≈ 0	± 0.000133	± 0.000177	± 0.000067	± 0.000240	± 0.000160
Beam orientation	± 0.00513	± 0.00513	± 0.00394	± 0.000623	± 0.000310	± 0.00069
Crossbeam angle	± 0.00833	± 0.00785	± 0.00654	± 0.000309	± 0.00083	± 0.000202
Finite probe volume	± 0.0025	± 0.00362	± 0.00304	± 0.00182	± 0.00652	± 0.00435
Processor errors						
Clock synchronization	0.0000025	0.0000019	0.0000025	0.0000002	0.0000004	0.0000001
Quantization	≈ 0	≈ 0	≈ 0	≈ 0	≈ 0	≈ 0
Electronic noise	0.000155	0.000262	0.000062	0.0000002	0.0000016	≈ 0
Seed-induced errors						
Particle lag	-0.0049	-0.0049	-0.0049	0	0	0
Velocity bias[2]						
Totals						
Total bias	$+0.0101$ -0.0112	$+0.0101$ -0.0112	$+0.00822$ -0.00957	± 0.00195	± 0.00658	± 0.00441
Precision errors	± 0.00168	± 0.00449	± 0.00110	± 0.00119	± 0.00318	± 0.000755
Total uncertainty	$+0.0106$ -0.0117	$+0.0136$ -0.0144	$+0.00851$ -0.00982	± 0.00308	± 0.00915	± 0.00467

[2]Not computed.

Table AII. Concluded

(b) Reynolds normal stresses, $U_\infty = 3$ in/sec

Error	$\dfrac{\overline{u'_v u'_v}}{U_\infty^2}$	$\dfrac{\overline{u'_g u'_g}}{U_\infty^2}$	$\dfrac{\overline{u'_b u'_b}}{U_\infty^2}$
Jet test			
Bias	0	0	0
Precision	±0.00067	±0.00171	±0.00042
Total uncertainty	±0.00067	±0.00171	±0.00042
Strake test			
Bias	0	0	0
Precision	±0.00006	±0.00040	±0.00002
Total uncertainty	±0.00006	±0.00040	±0.00002

(c) Reynolds shear stresses and fluorescence-related data, $U_\infty = 3$ in/sec

Error	$\dfrac{\overline{u'_v u'_g}}{U_\infty^2}$	$\dfrac{\overline{u'_g u'_b}}{U_\infty^2}$	$\dfrac{\overline{u'_b u'_v}}{U_\infty^2}$	$\dfrac{\overline{u'_v c'}}{U_\infty c_{\max}}$	$\dfrac{\overline{u'_g c'}}{U_\infty c_{\max}}$	$\dfrac{\overline{u'_b c'}}{U_\infty c_{\max}}$	$\dfrac{c}{c_{\max}}$	$\dfrac{c'}{c_{\max}}$
Jet test								
Bias	0	0	0	0	0	0	±0.0014	±0.0029
Precision	±0.00060	±0.00016	±0.00036	±0.00015	±0.00008	±0.00005	±0.00346	±0.00244
Total uncertainty	±0.00060	±0.00016	±0.00036	±0.00015	±0.00008	±0.00005	±0.00706	±0.00568
Strake test								
Bias	0	0	0				±0.0014	±0.0029
Precision	±0.00007	±0.00004	±0.00002				±0.00461	±0.00326
Total uncertainty	±0.00007	±0.00004	±0.00002				±0.00933	±0.00714

Table AIII. Final Estimated Total Uncertainties in Fluctuating
Quantities Relative to Reference Values

| Parameter | Total uncertainties, percent, for— | |
	Jet test	Strake test
$\sqrt{\overline{u'^2}}/U_\infty$	2	0.6
$\sqrt{\overline{v'^2}}/U_\infty$	6	3
$\sqrt{\overline{w'^2}}/U_\infty$	2	.9
$\overline{u'u'}/U_\infty^2$	.2	.02
$\overline{v'v'}/U_\infty^2$	5	.6
$\overline{w'w'}/U_\infty^2$	.2	.01
$\overline{u'v'}/U_\infty^2$	.8	.1
$\overline{v'w'}/U_\infty^2$	.4	.05
$\overline{w'u'}/U_\infty^2$	.1	.01
$\overline{u'c'}/U_\infty c_{\max}$	.3	
$\overline{v'c'}/U_\infty c_{\max}$	1	
$\overline{w'c'}/U_\infty c_{\max}$	.1	
$\overline{c}/c_{\max}$	1	1
$\sqrt{\overline{c'^2}}/c_{\max}$	2	1

References

1. Trolinger, J. D.: Laser Applications in Flow Diagnostics. AGARD-AG-296, Oct. 1988.

2. Durst, F.; Melling A.; and Whitelaw, J. H.: *Principles and Practice of Laser-Doppler Anemometry.* Academic Press, 1981.

3. Adrian, Ronald J.: "Laser Velocimetry," *Fluid Mechanics Measurements*, Richard J. Goldstein, ed., Hemisphere Publ. Corp., 1983, pp. 155–244.

4. Guilbault, George G.: *Practical Fluorescence—Theory, Methods, and Techniques.* Marcel Dekker, Inc., 1973.

5. McDevitt, T. Kevin; Ambur, Todd A.; Orngard, Gary M.; and Owen, F. Kevin: *Measurement of Vortex Flow Fields.* NASA CR-189543, 1992.

6. Pendergraft, Odis C., Jr.; Neuhart, Dan H.; and Kariya, Timmy T.: *A User's Guide to the Langley 16- by 24-Inch Water Tunnel.* NASA TM-104200, 1992.

7. Rhodes, David B.; Franke, John M.; Jones, Stephen B.; and Leighty, Bradley D.: *A Twin-Mirrored Galvanometer Laser Light Sheet Generator.* NASA TM-100587, 1988.

8. Dring, R. P.; and Suo, M.: Particle Trajectories in Swirling Flows. *J. Energy*, vol. 2, no. 4, July–Aug. 1978, pp. 232–237.

9. Patrick, William P.: *Error Analysis for Benchmark Fluid Dynamic Experiments, Part I: Error Analysis Methodology and the Quantification of Laser Velocimeter Error Sources.* R85-151772, UTRC, June 1985.

10. Sforza, P. M.; Steiger, M. H.; and Trentacoste, N.: Studies on Three-Dimensional Viscous Jets. *AIAA J.*, vol. 4, no. 5, May 1966, pp. 800–806.

11. Rajaratnam, N.: *Turbulent Jets.* Elsevier Scientific Publ. Co., 1976.

12. Trentacoste, Nicholas; and Sforza, Pasquale: Further Experimental Results for Three-Dimensional Free Jets. *AIAA J.*, vol. 5, no. 5, May 1967, pp. 885–891.

13. Hinze, J. O.: *Turbulence*, Second ed. McGraw-Hill Book Co., 1975.

14. Verhaagen, N.; and Van Ransbeeck, P.: Experimental and Numerical Investigation of the Flow in the Core of a Leading Edge Vortex. AIAA-90-0384, Jan. 1990.

15. *Measurement Uncertainty. Part 1—Instruments and Apparatus.* ANSI/ASME PTC 19.1-1985, 1986.

16. Coleman, Hugh W.; and Steele, W. Glenn, Jr.: *Experimentation and Uncertainty Analysis for Engineers.* John Wiley & Sons, 1989.

17. Morrison, G. L.; Johnson, M. C.; Swan, D. H.; and Deotte, R. E., Jr.: Advantages of Orthogonal and Non-Orthogonal Three-Dimensional Anemometer Systems. *Flow Meas. Instrum.*, vol. 2, Apr. 1991, pp. 89–97.

18. Gartrell, Luther R.; Gooderum, Paul B.; Hunter, William W., Jr.; and Meyers, James F. (Appendix by James F. Meyers): *Laser Velocimetry Technique Applied to the Langley 0.3-Meter Transonic Cryogenic Tunnel.* NASA TM-81913, 1981.

19. Meyers, James F.: Laser Velocimeter Data Acquisition and Real Time Processing Using a Microcomputer. *Fourth International Symposium on Applications of Laser Anemometry to Fluid Mechanics*, Springer-Verlag, July 1989.

20. Meyers, James F.: "Biasing Errors and Corrections," *Laser Velocimetry, Volume 1*, VKI, June 1991, pp. 23–36.

21. Szulc, Stefan; J. Stadler, transl.: *Statistical Methods.* Pergamon Press, 1965.

22. Holbrook, G. Thomas; Dunham, Dana Morris; and Greene, George C.: *Vortex Wake Alleviation Studies With a Variable Twist Wing.* NASA TP-2442, 1985.

23. Milne-Thomson, L. M.: *Theoretical Aerodynamics, Fourth ed.* Dover Publ., Inc., 1973.

24. Panton, Ronald L.: *Incompressible Flow.* John Wiley & Sons, 1984.

25. Neti, Sudhakar; and Clark, Wayne: On-Axis Velocity Component Measurement With Laser Velocimeters. *AIAA J.*, vol. 17, no. 9, Sept. 1979, pp. 1013–1014.

26. Yanta, William J.; and Ausherman, Donald W.: A 3-D Laser Doppler Velocimeter for Use in High-Speed Flows. *Proceedings of the Seventh Symposium on Turbulence*, 1983, pp. 350–359.

27. Bell, J. H.; Rodman, L. C.; and Mehta, R. D.: Aspects of the Design and Performance of a 3-Component LDV System. *ICIASF '85 Record*, IEEE, Aug. 1985, pp. 288–296.

Intersecting laser beams

Flow

Seeding particles in the flow

Interference fringes

Scattered light

Filter

Filter

LDV photodetector

Fluorescence photodetector
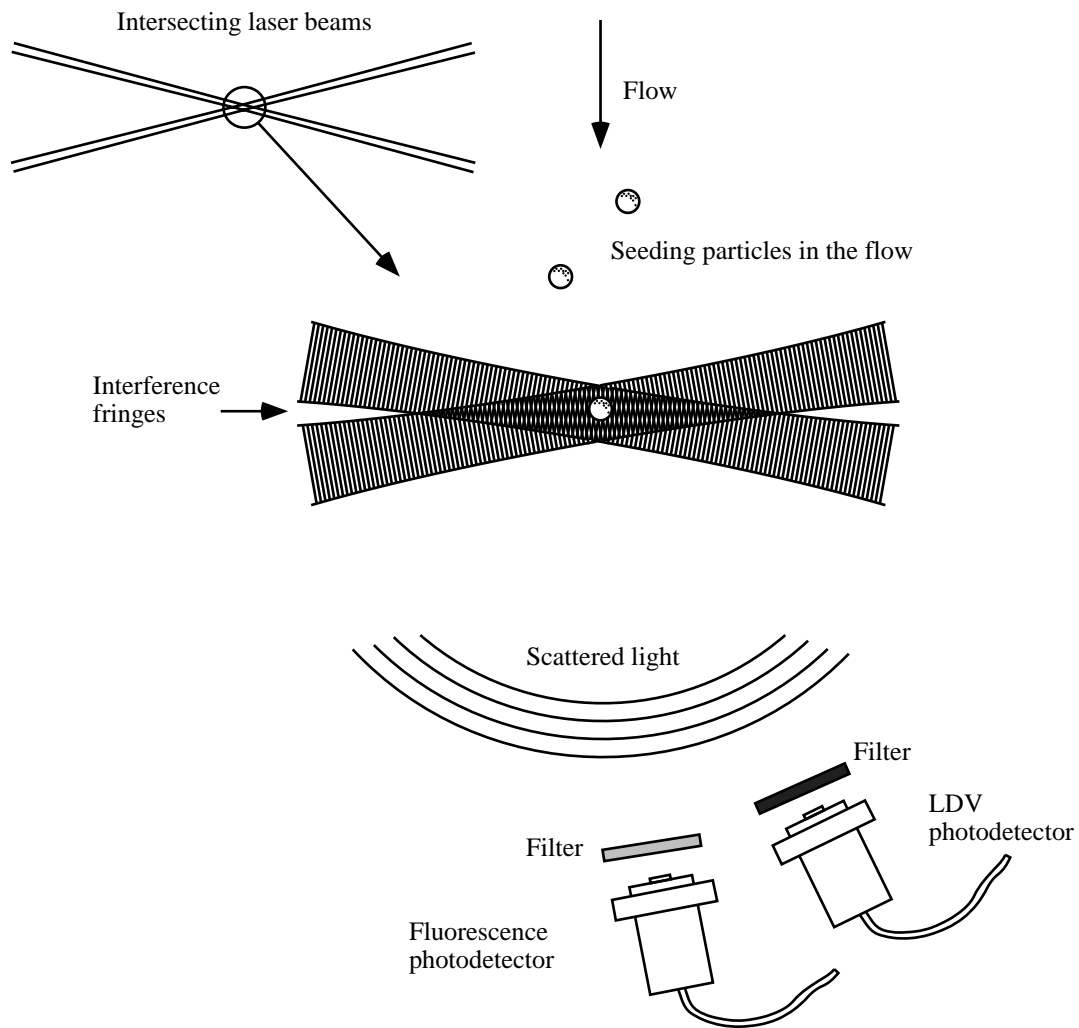
$$u_n = \Delta\nu\, d_f$$

In which:

u_n Velocity component of particle
normal to laser beam bisector

$\Delta\nu$ Doppler-shift frequency of scattered light

d_f Fringe spacing

Figure 1. Dual beam LDV and fluorescence probes.

Figure 2. Fluorescein dye spectra.

Figure 3. Langley 16- by 24-Inch Water Tunnel.
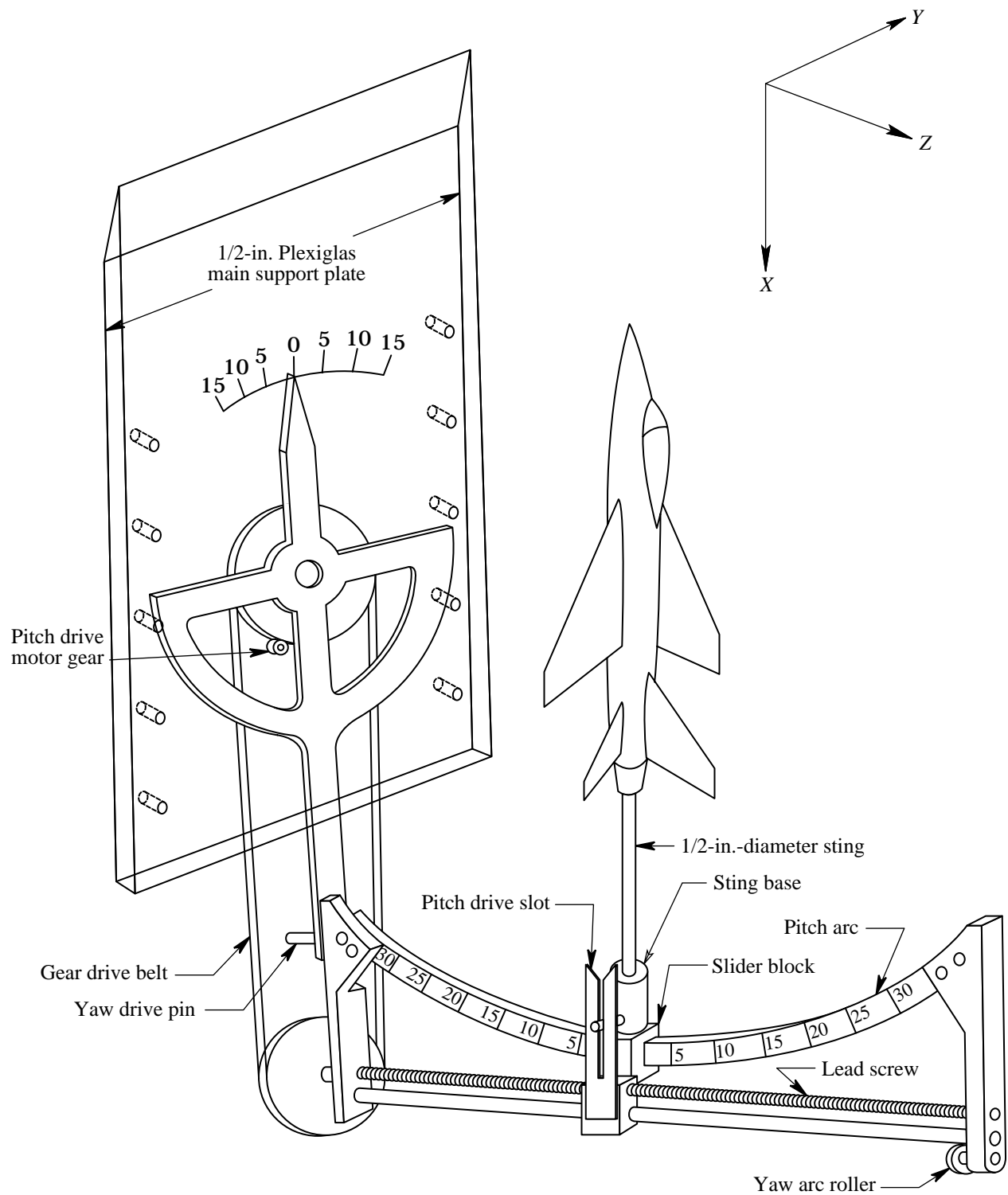
Figure 4. Model support angle-of-attack and sideslip mechanism.

Top

(a) Model in test section.

Figure 5. Nonaxisymmetric propulsion model.

12.474

Flow-
conditioning
foam

Y

X

1.032

1.348

Section A-A

Z

Y

A

Alternate
water
supply

Support
strut

Z

X

.532

1.230

A
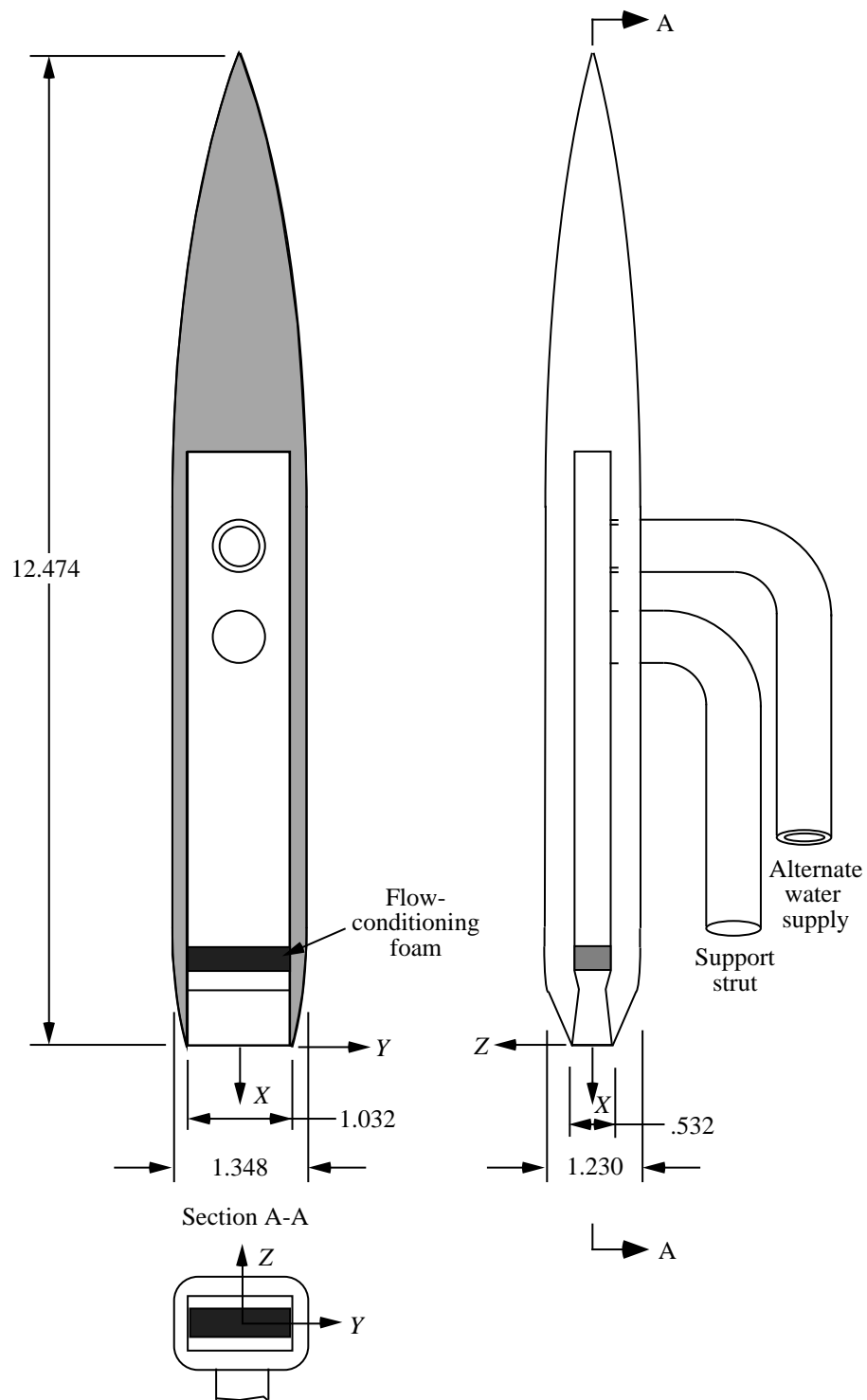
(b) Principle dimensions. All dimensions are in inches.

Figure 5. Concluded.
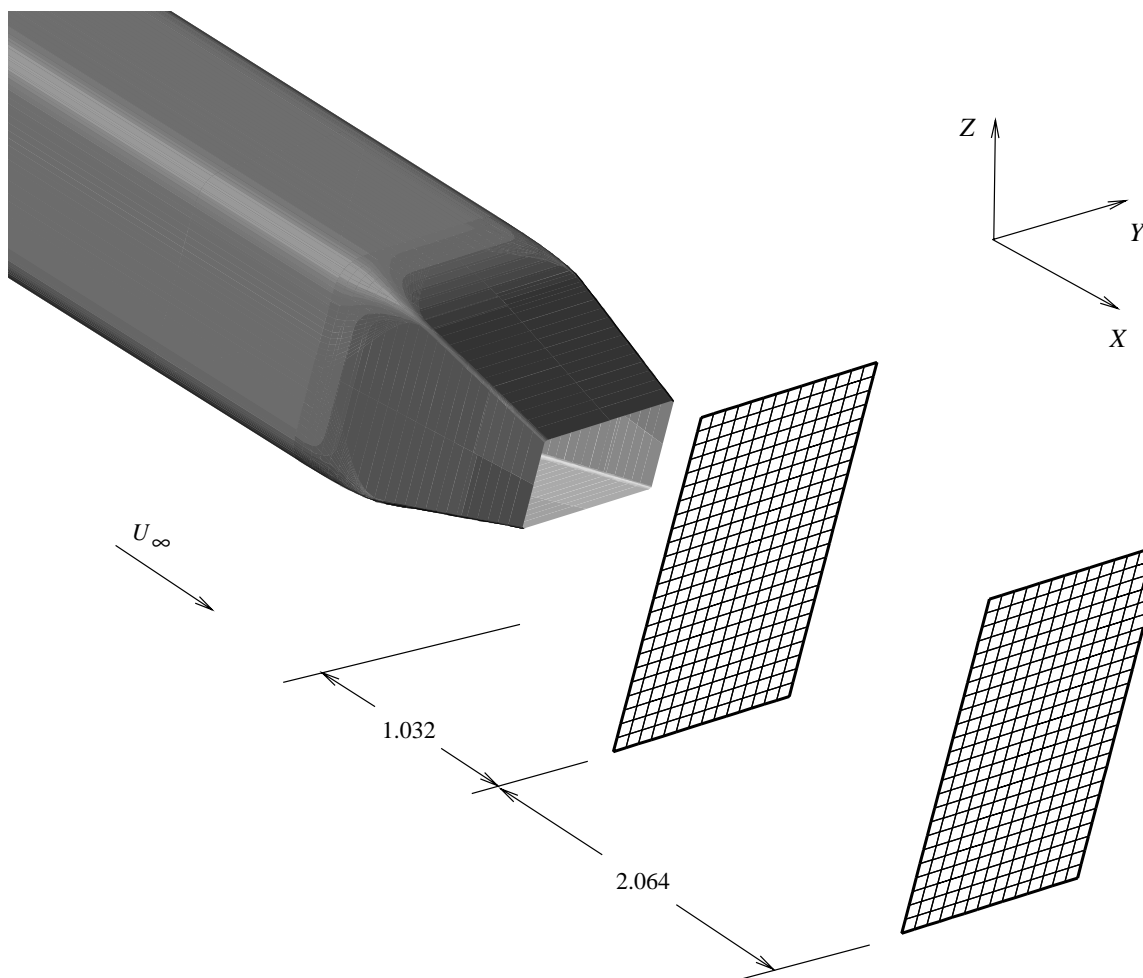
Figure 6. Nonaxisymmetric nozzle model measurement grids. All dimensions are in inches.

(a) Model in test section.

Figure 7. Axisymmetric forebody with strake.

Forebody
Top view

Baseline strake
Top view

R

X

Y

X

$x = 2.68$
$y = -2.41$ $r = 3.53$

$x = 3.768$

11.00

Cambered strake

3-percent biconvex wrapped around
NACA-63 mean line with
planar outer edge

Top view

Side view

Z

A

A

X

Section A-A
(enlarged)

Forebody coordinates, in.			
x	r	x	r
0.000	0.000	4.007	1.045
.184	.138	5.007	1.142
.407	.240	6.007	1.220
1.007	.461	7.465	1.295
2.007	.725	8.500	1.325
3.007	.921	11.000	1.325
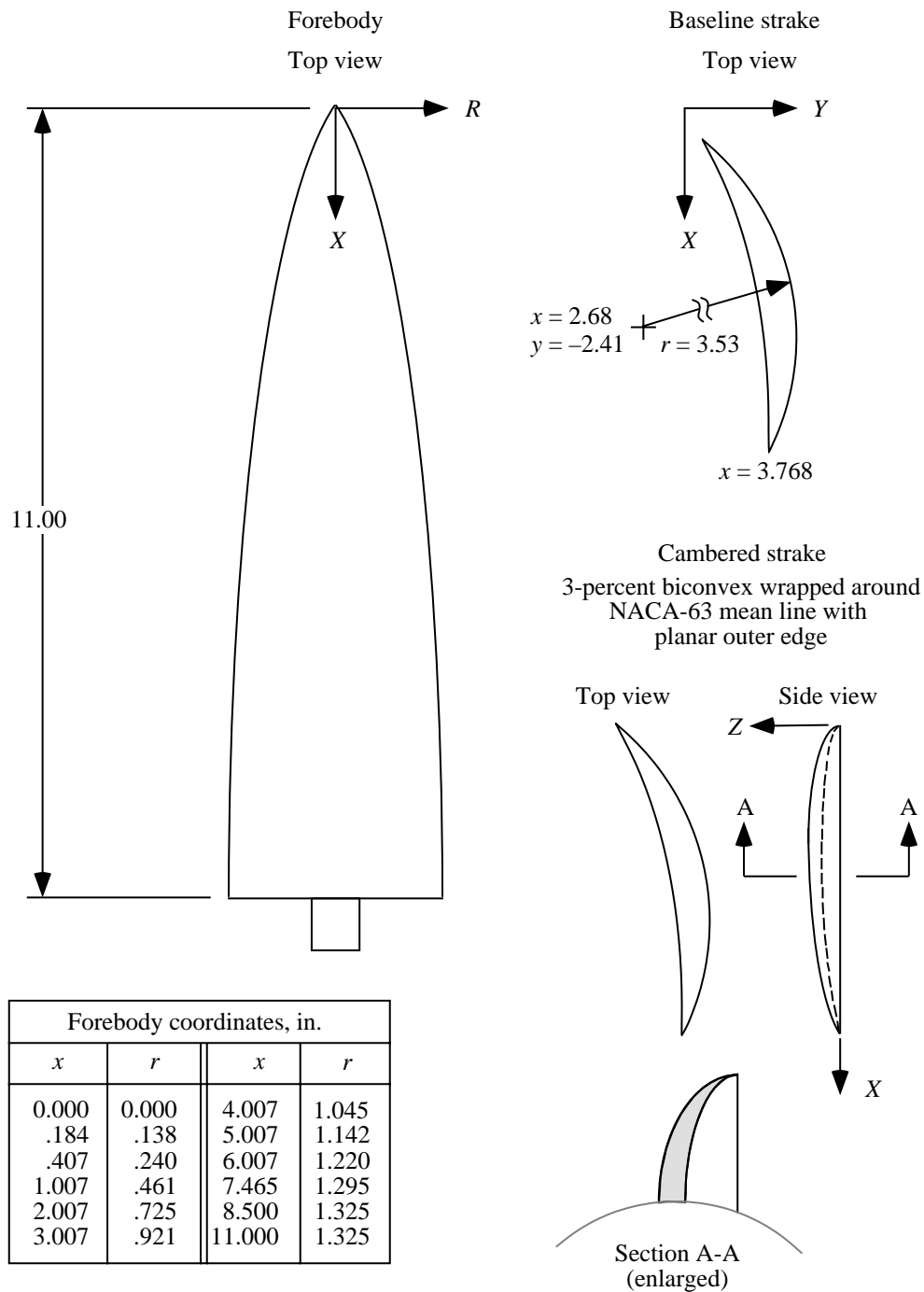
(b) Principle dimensions. All dimensions are in inches.

Figure 7. Concluded.
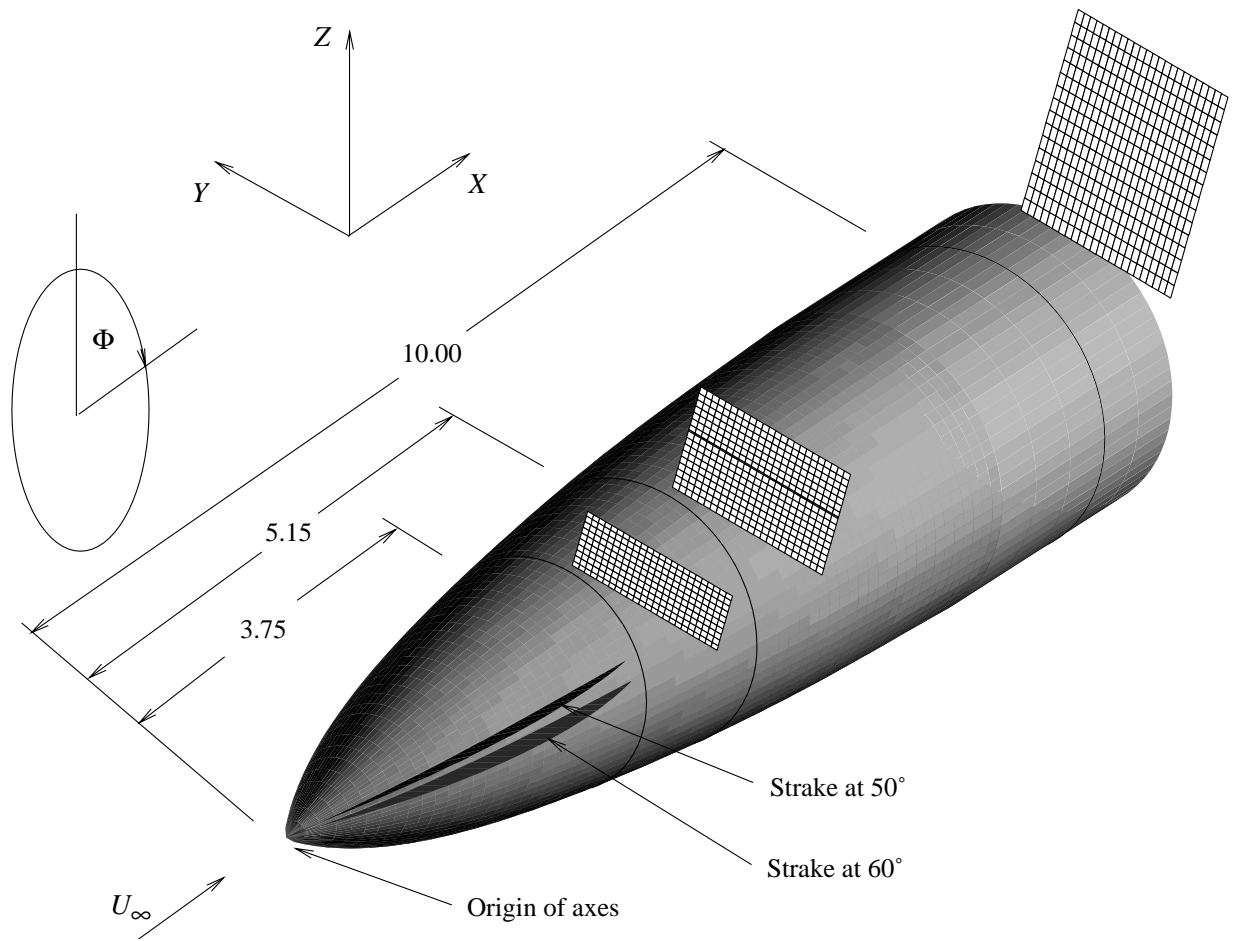
Figure 8. Axisymmetric forebody-strake model with candidate strakes and measurement grids. All linear dimensions are in inches.

u_∞ →
(No dye)

u_j →
(Dye tracer)

Laser beams

Jet core: Low mixing with free-stream and
high dye concentration

Shear regions: High mixing with free-stream and
high dye concentration fluctuations
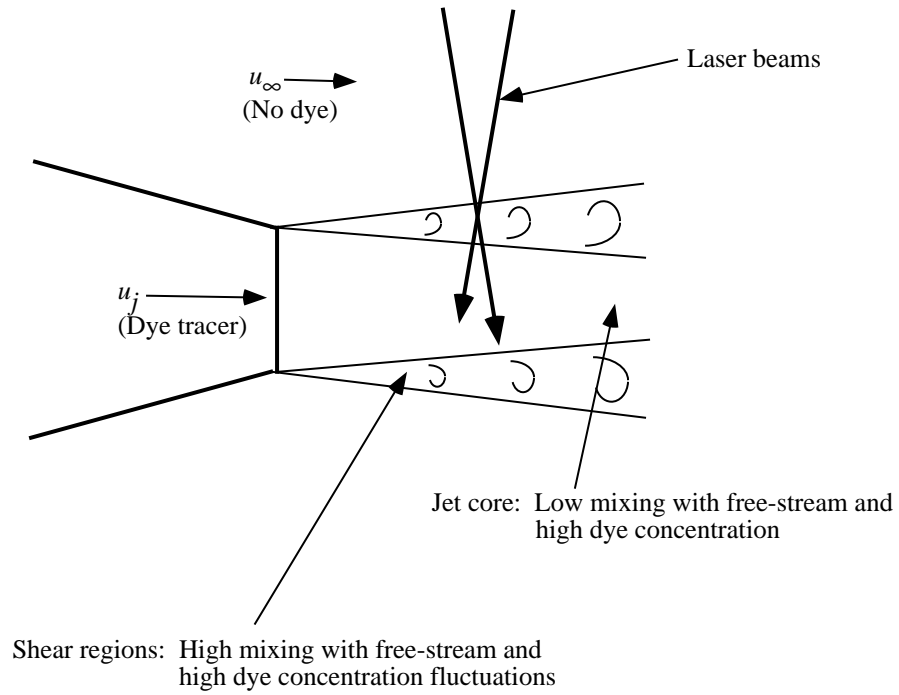
Figure 9. Laser beams probing jet.

Light-
separating
optics

Argon ion laser

Fiber-optic cables

Transmitting lens

Receiving lenses

Sample volume
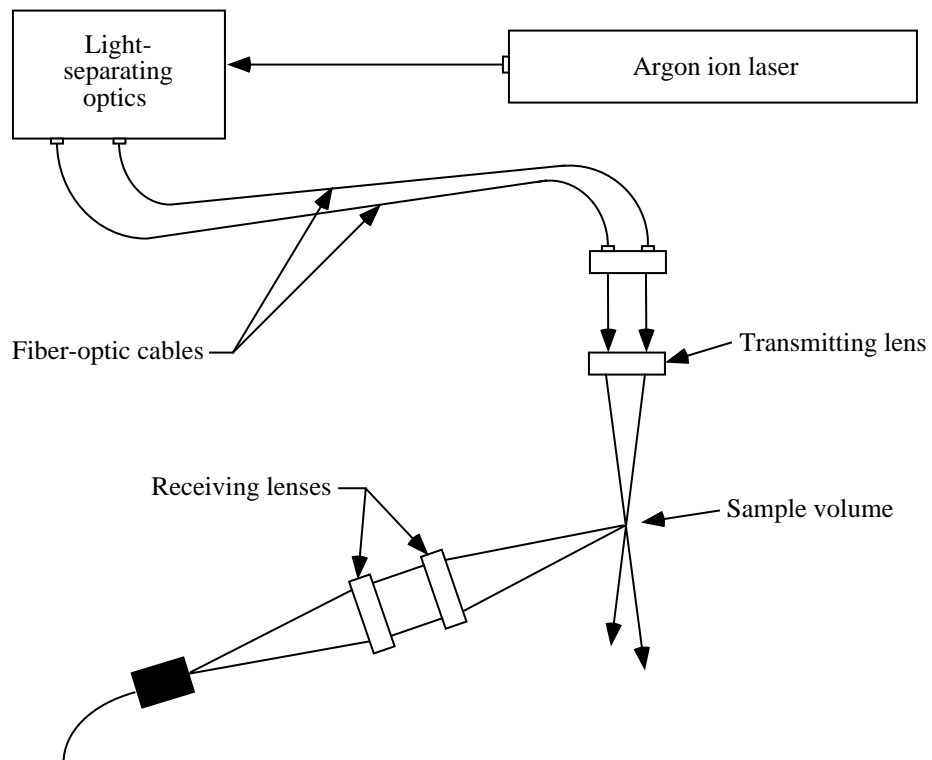
Figure 10. Laser beam transmission and scattered light collection.
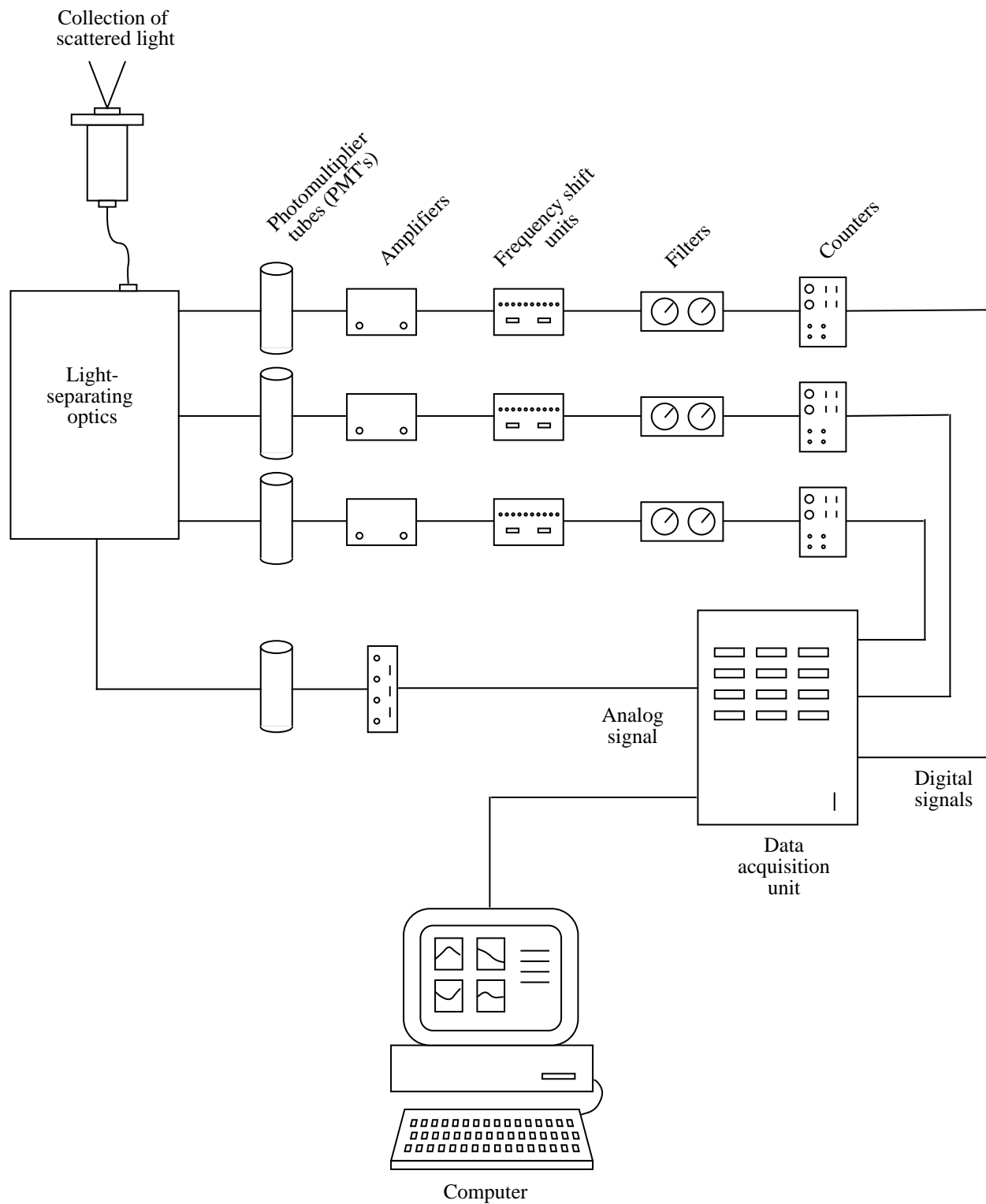
Figure 11. Data acquisition system.

Traverse and optics,
receiving side

Water tunnel
test section

Traverse and optics,
transmitting side

Flow
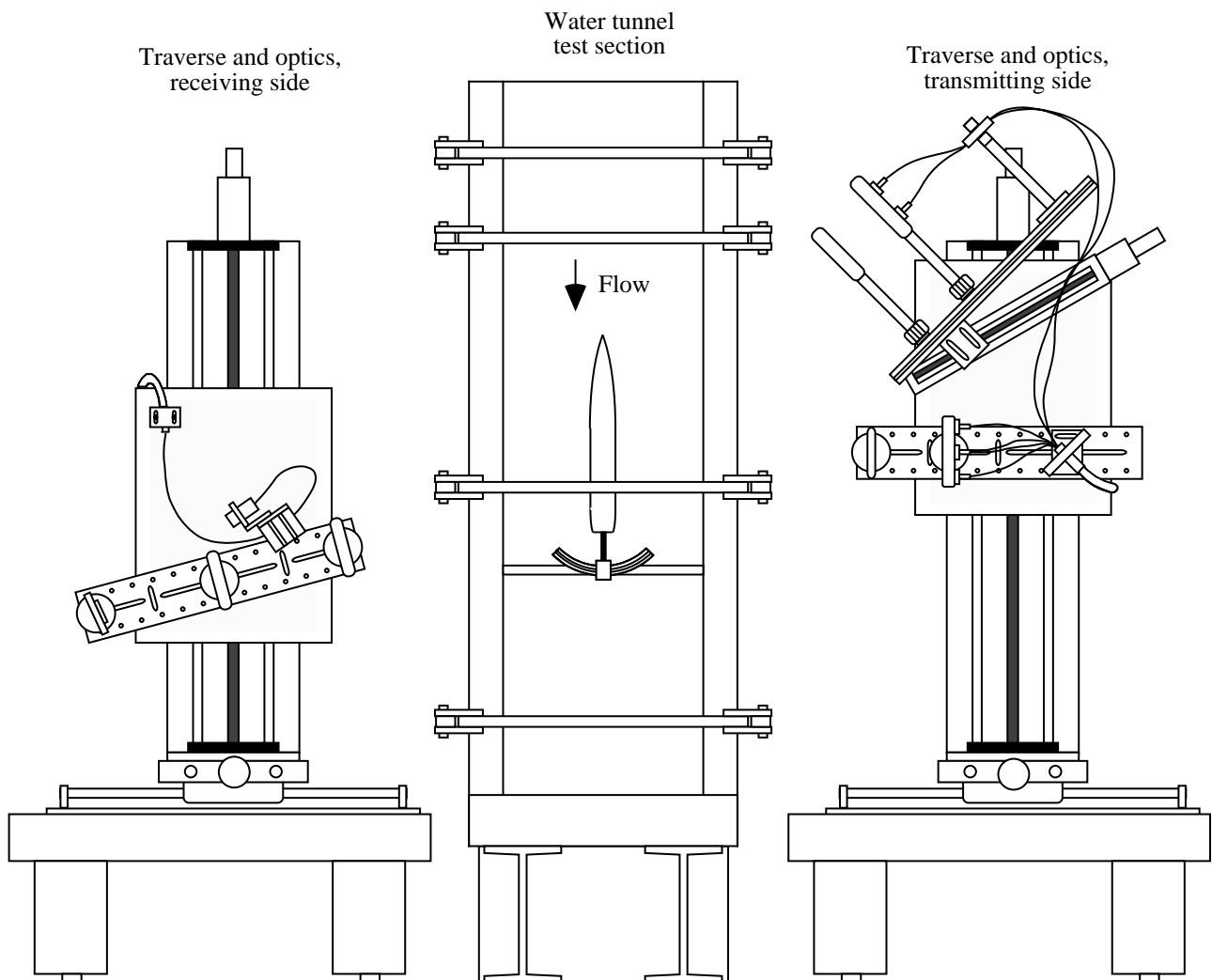
Figure 12. Water tunnel laser instrument.
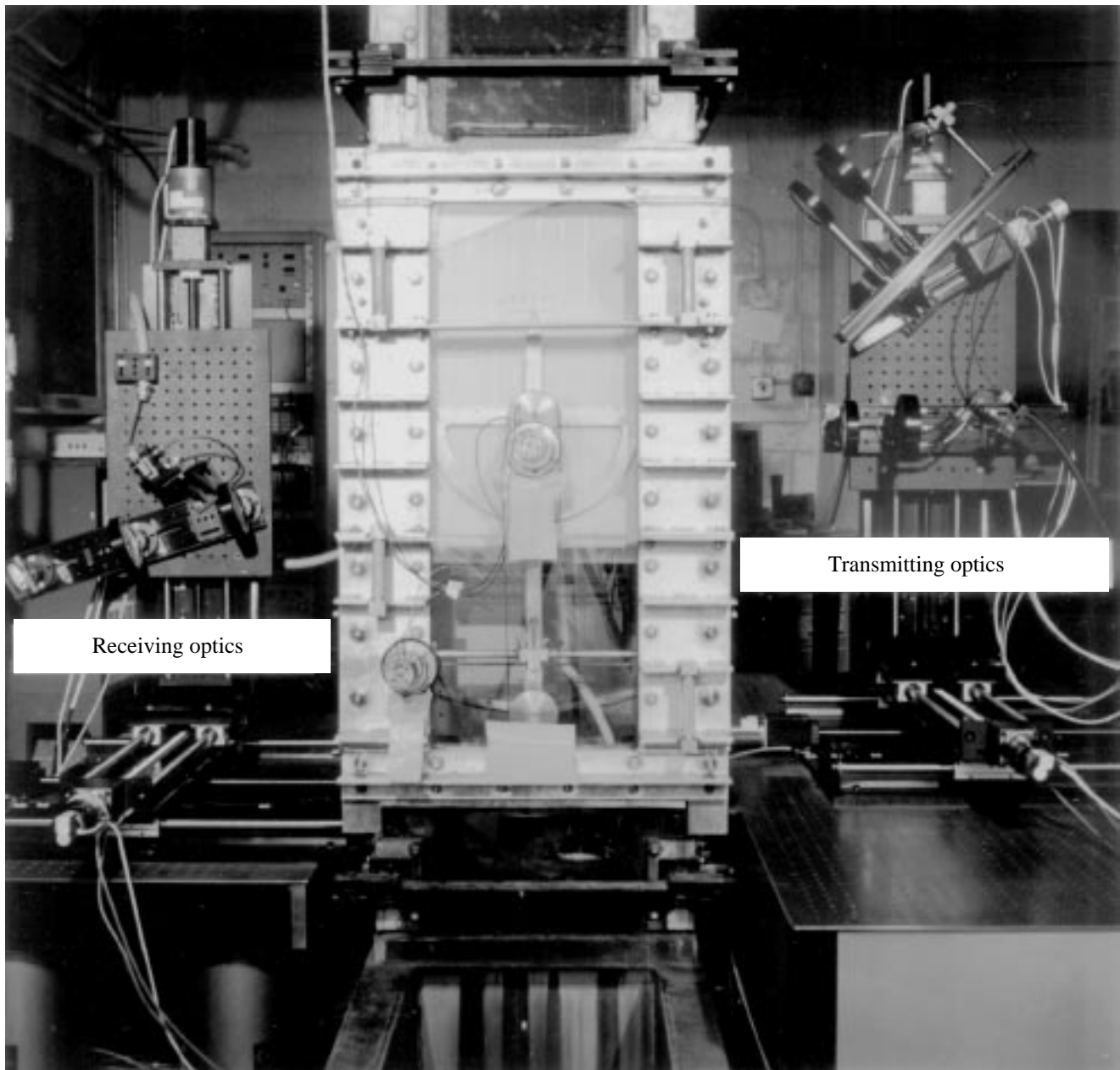
Figure 13. Laser instrument installed at Langley 16- by 24-Inch Water Tunnel.

Incident beam

n_1

n_2

n_3

Lens

Optical axis

d

W

F
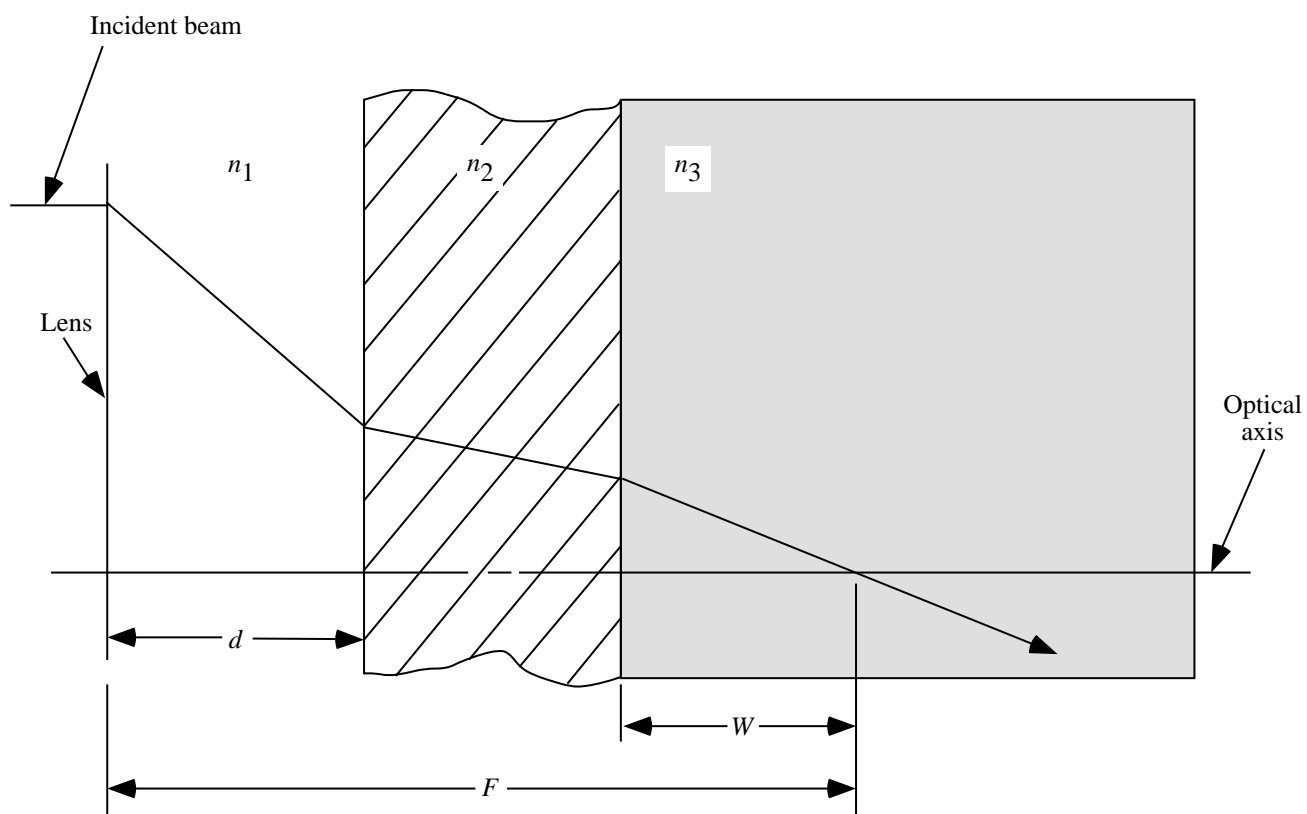
Indices of refraction

$n_1 = 1.0$ (air)

$n_2 = 1.43$ (Lucite™)[1]

$n_3 = 1.333$ (water)

[1]Lucite: trademark of E. I. du Pont de Nemours & Co.

Figure 14. Beam refraction through media.
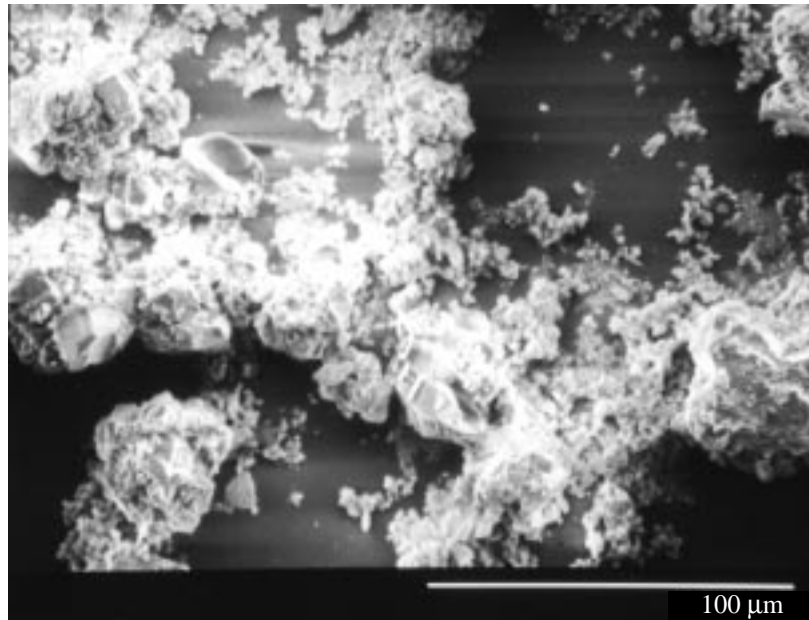
(a) Scanning electron microscope photograph of seeding.
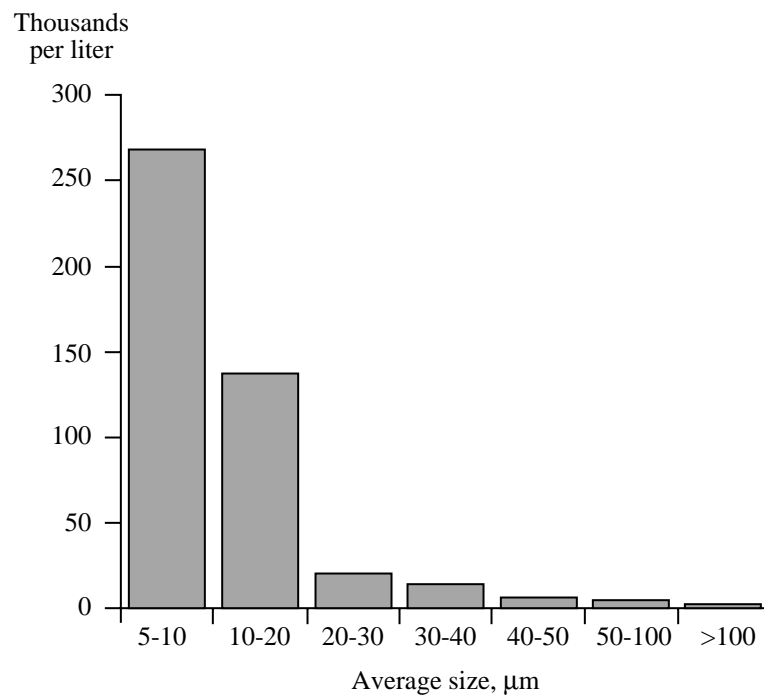
(b) Particle size distribution.

Figure 15. Water tunnel seeding for laser Doppler velocimeter (natural particulates).

(a) $x/W = 0$.
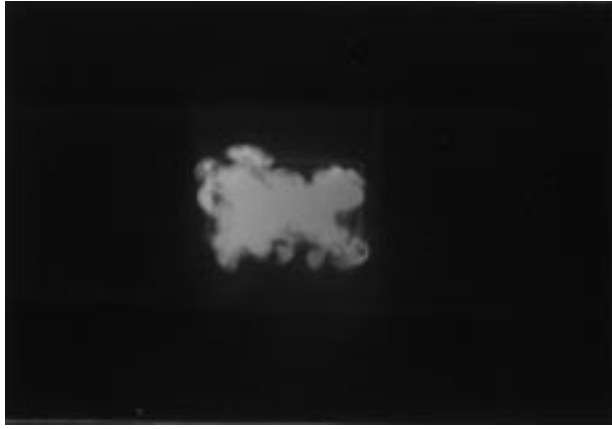
(b) $x/W = 1$.
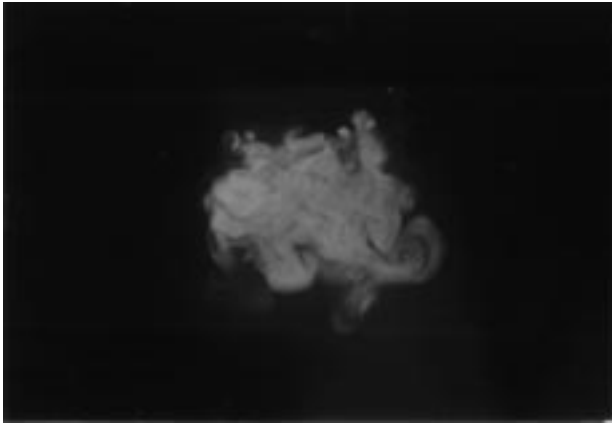
(c) $x/W = 3$.

Figure 16. Laser light sheet flow visualization of nonaxisymmetric propulsion model. $\alpha = 4°$; $U_j/U_\infty = 1.7$.

50
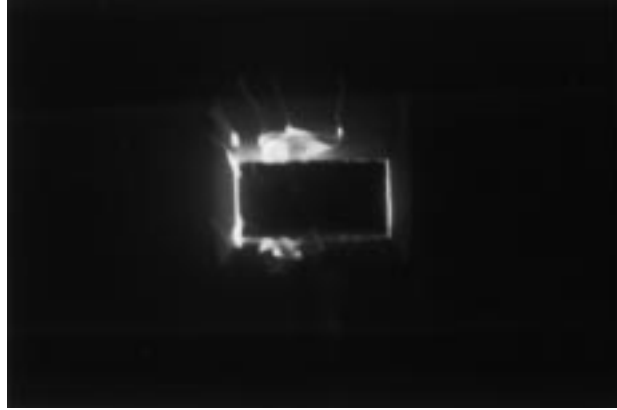
(a) $x/W = 0$.
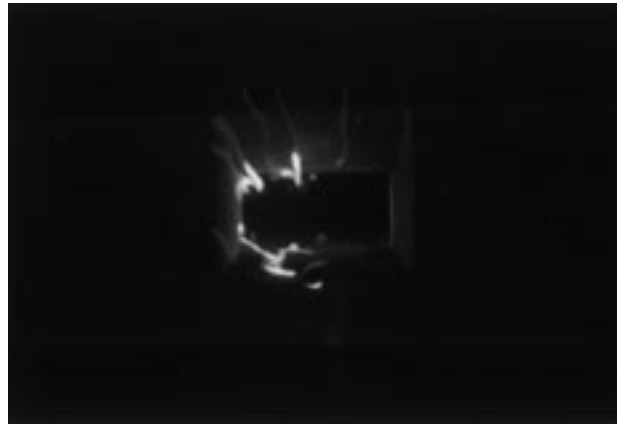
(b) $x/W = 0.5$.

(c) $x/W = 1$.

Figure 17. Laser light sheet flow visualization of nonaxisymmetric propulsion model. $\alpha = 4^{\circ}$; $U_j/U_\infty = 1.7$; external dye only.

(a) $x = 1.032$ in.

(b) $x = 3.096$ in.
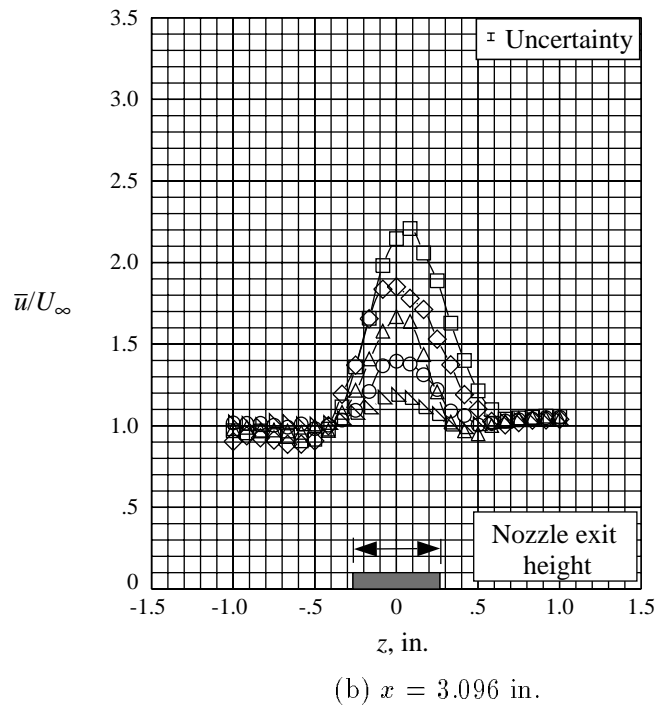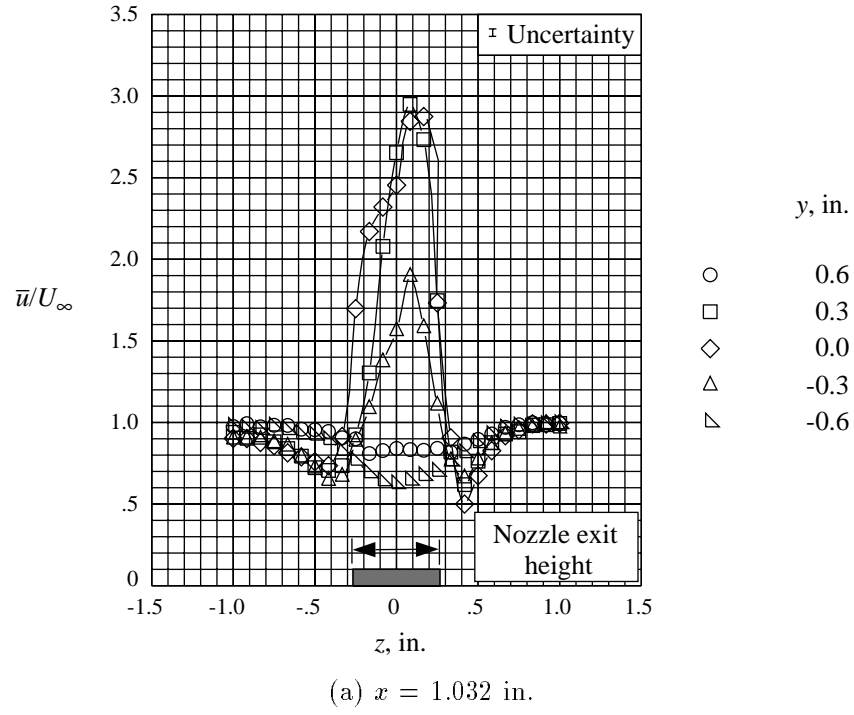
Figure 18. Axial velocity profiles for nonaxisymmetric boattail model. $U_j/U_\infty = 1.7$; $\alpha = 0°$.

(a) $U_j/U_\infty = 1.7$.

(b) $U_j/U_\infty = 3.0$.
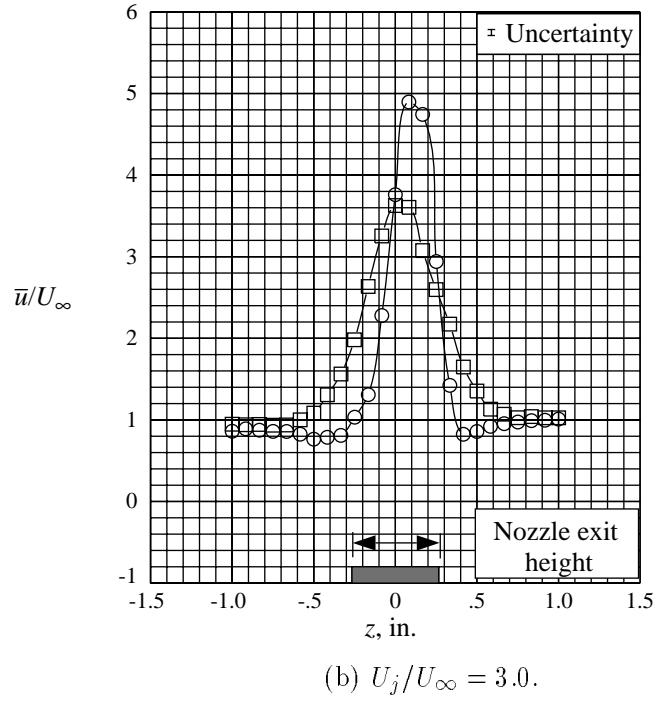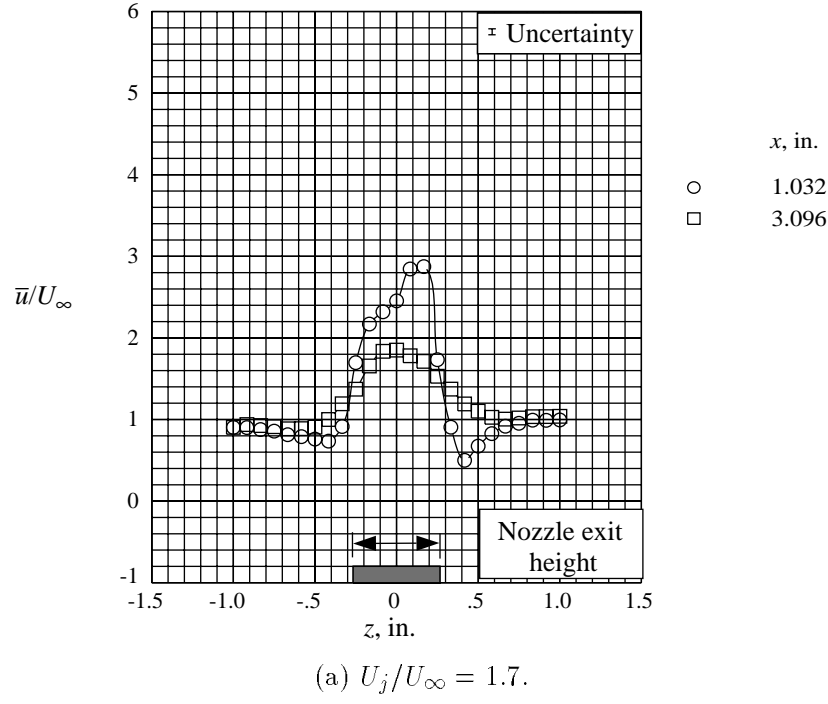
Figure 19. Effect of measurement location downstream from nozzle exit on axial velocity profile of non-axisymmetric boattail model. $y = 0$ in.; $\alpha = 0°$.

(a) $x = 1.032$ in.; $U_j/U_\infty = 1.7$; $\alpha = 0°$.

Figure 20. Axial velocity contours.

(b) $x = 1.032$ in.; $U_j/U_\infty = 1.7$; $\alpha = 4°$.

Figure 20. Concluded.

(a) $\alpha = 0°$.

(b) $\alpha = 4°$.
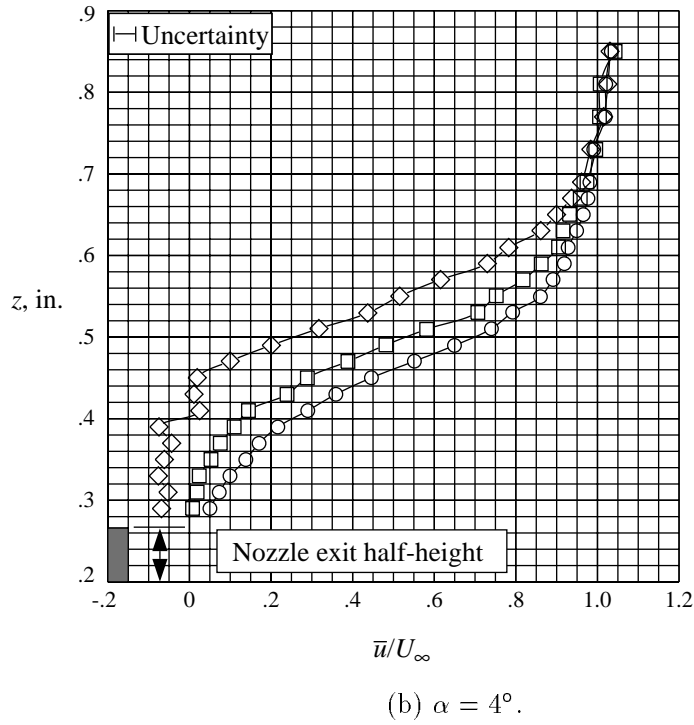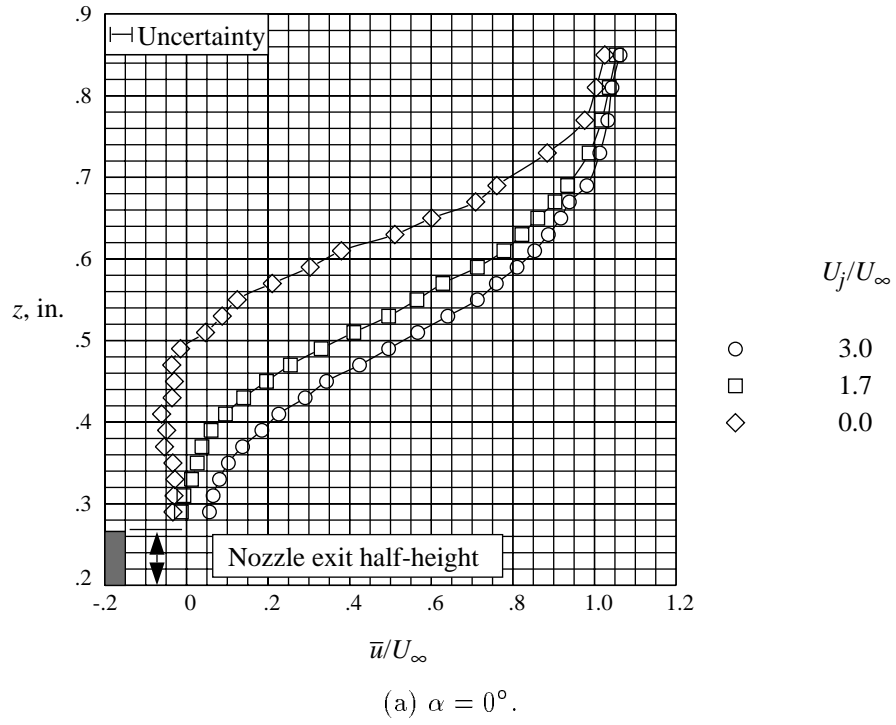
Figure 21. Vertical distribution of boattail axial velocity profiles for nonaxisymmetric boattail model. $x = 0$ in.; $y = 0$ in.

(a) $\alpha = 0°$.

(b) $\alpha = 4°$.
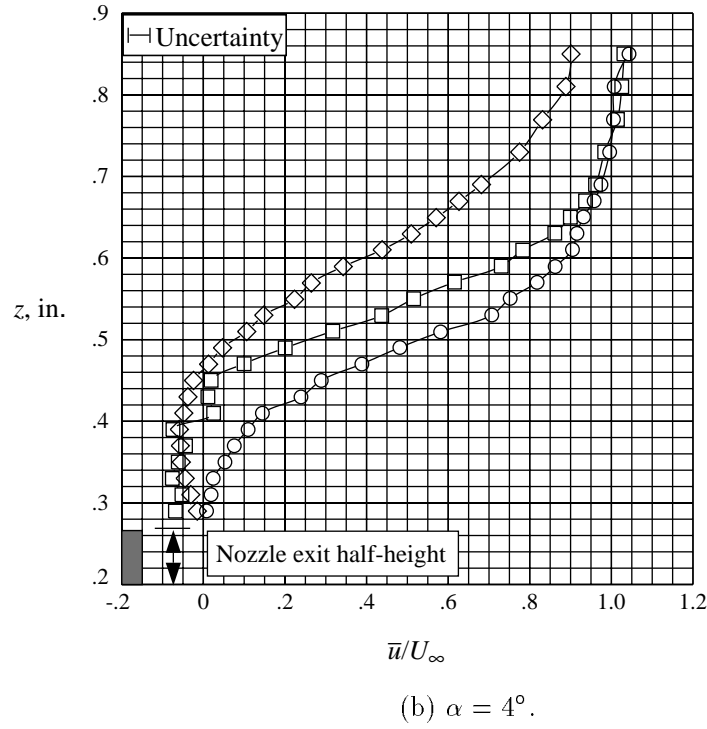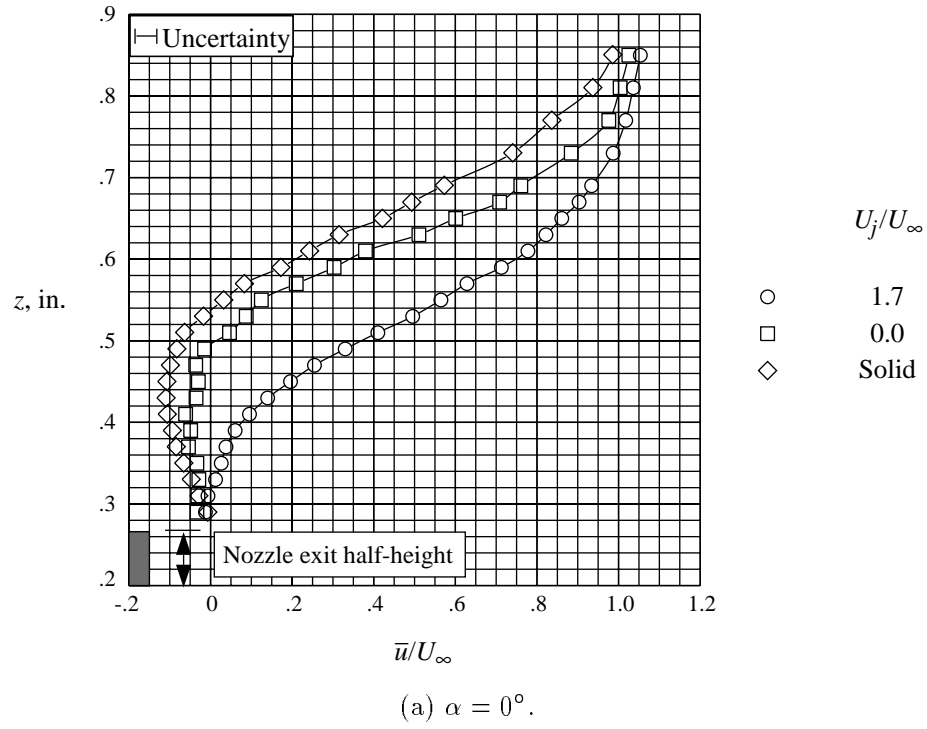
Figure 22. Vertical distribution of boattail axial velocity profiles of nonaxisymmetric boattail model with solid plume included. $x = 0$ in.; $y = 0$ in.

(a) $U_j/U_\infty = 3.0$.

(b) $U_j/U_\infty = 1.7$.
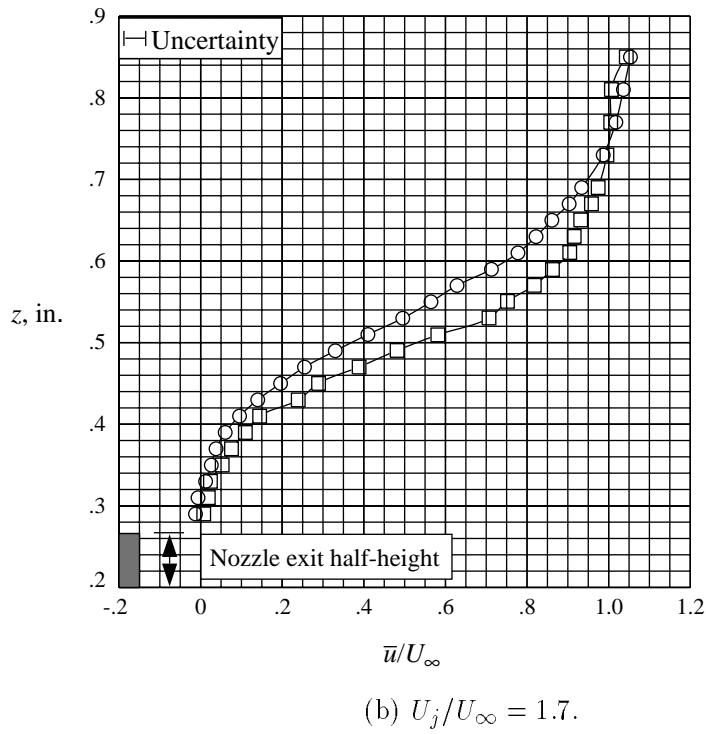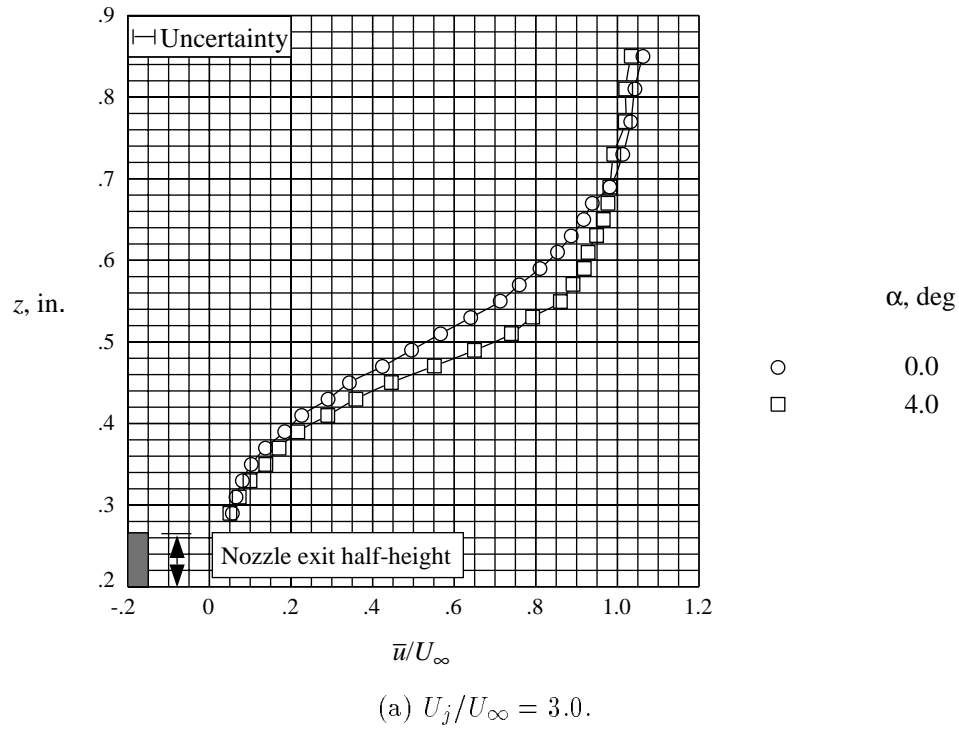
Figure 23. Effect of angle of attack on boattail axial velocity vertical profile of nonaxisymmetric boattail. $x = 0$ in.; $y = 0$ in.
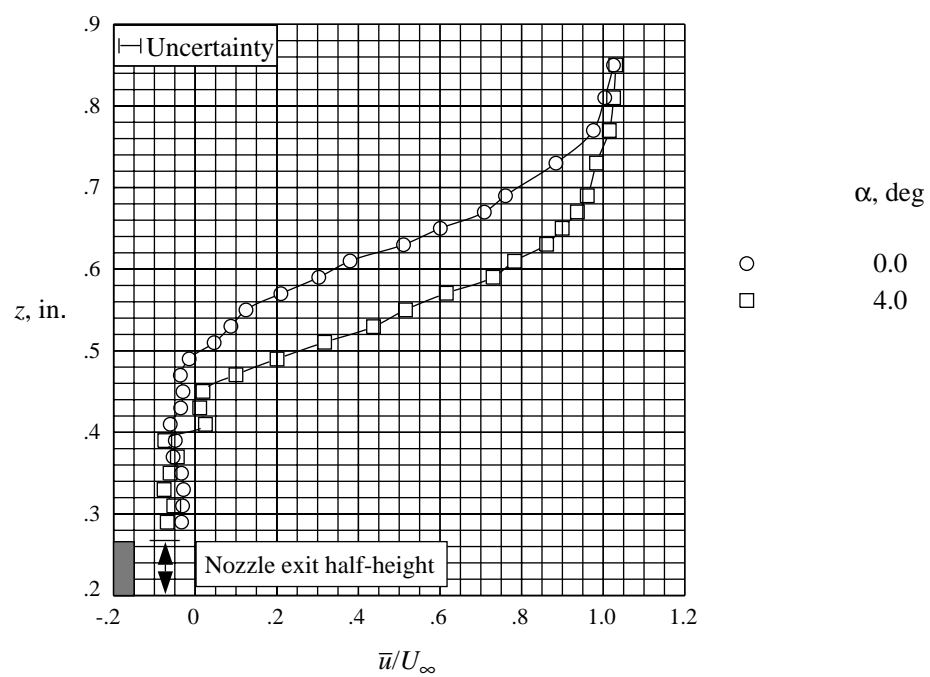
(c) $U_j/U_\infty = 0$.

Figure 23. Concluded.
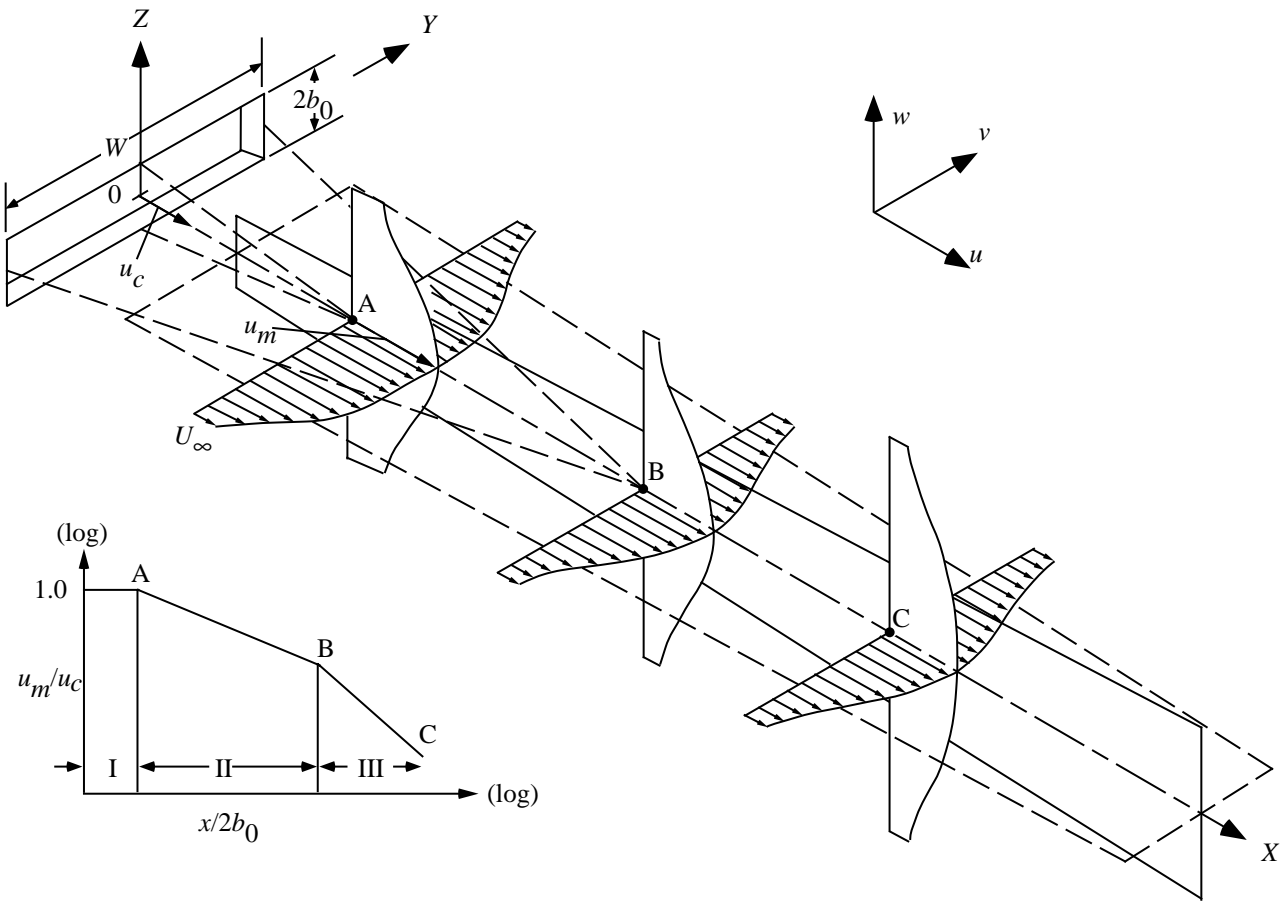
Figure 24. Representation of flow field of compound rectangular jet.
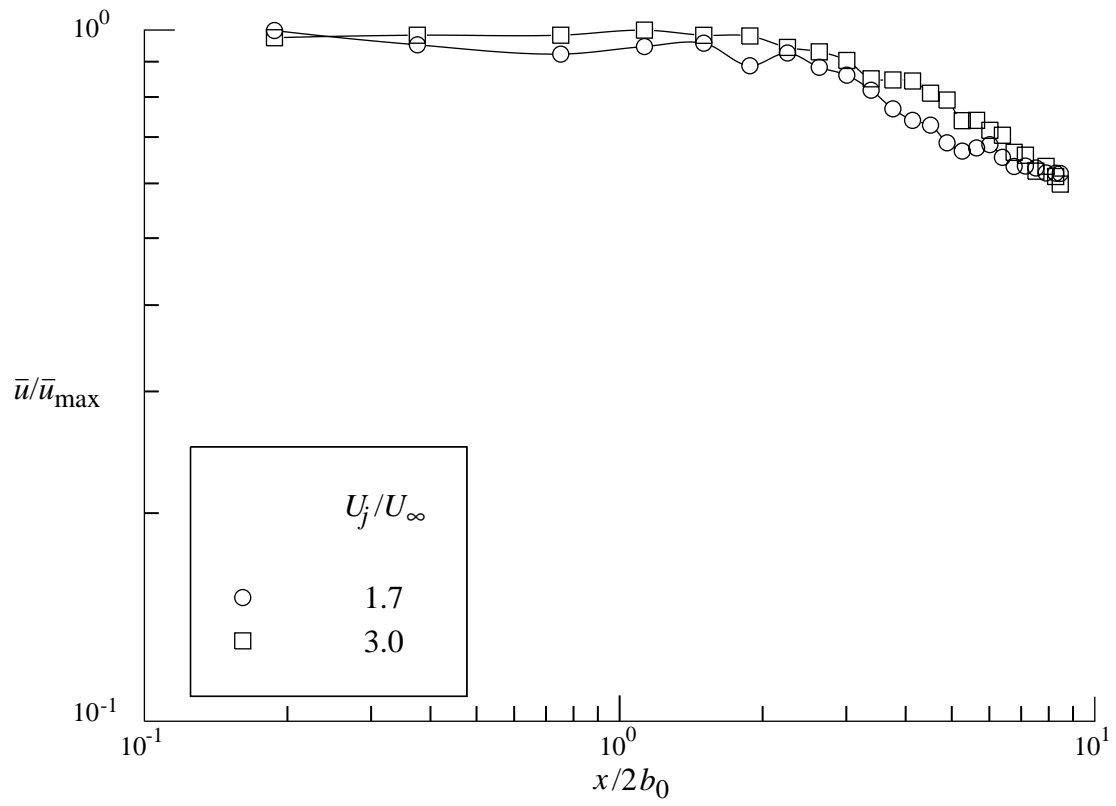
Figure 25. Axial velocity decay on jet centerline of nonaxisymmetric boattail model. $y = 0$ in.; $z = 0$ in.; $\alpha = 0°$.
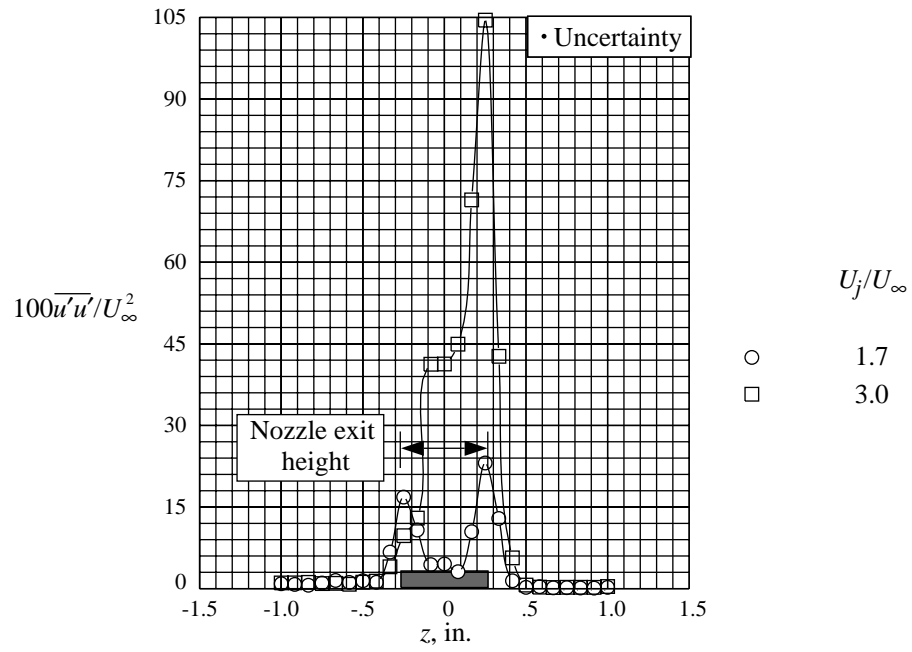
(a) $x = 1.032$ in.
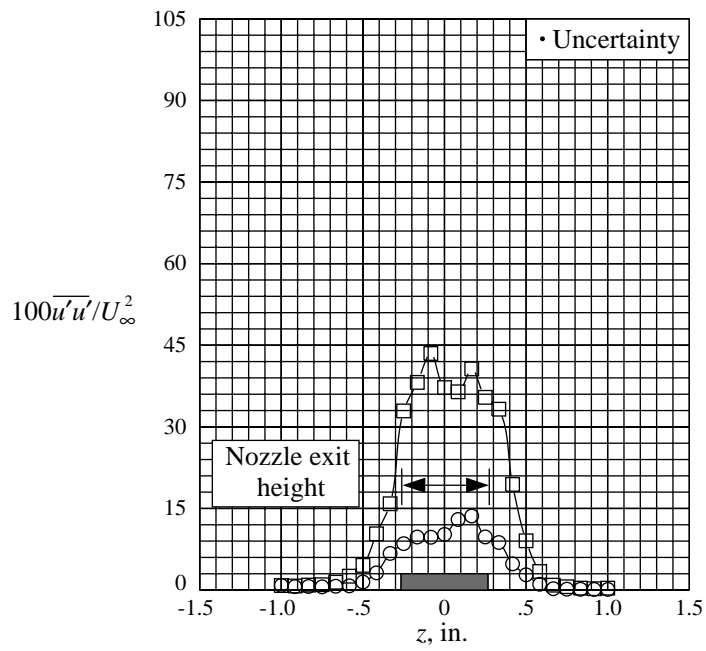
(b) $x = 3.096$ in.

Figure 26. Reynolds normal stress $\left(\overline{u'u'}\right)$ profiles for nonaxisymmetric boattail model. $y = 0$ in.; $\alpha = 0°$.
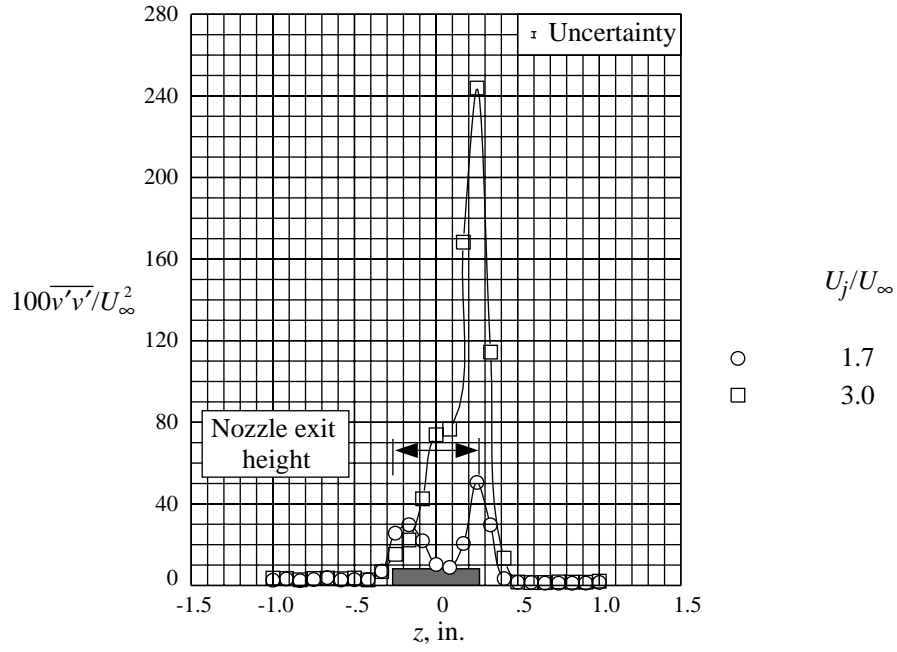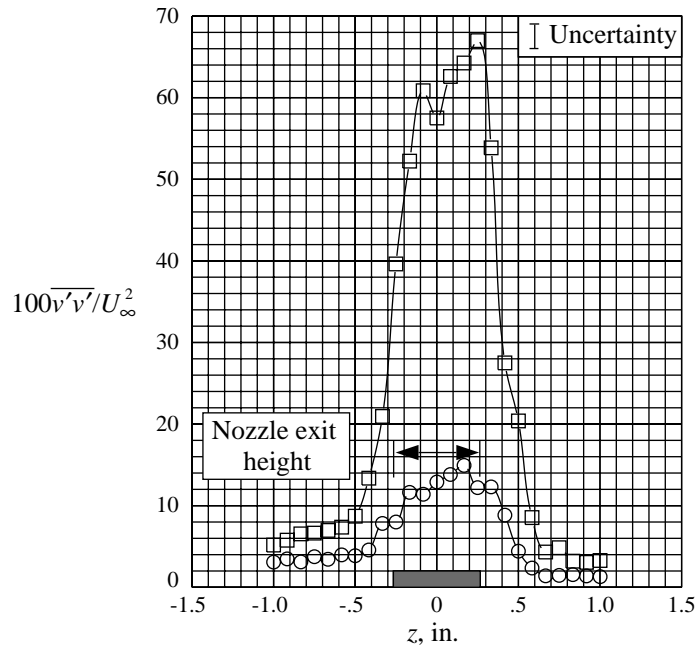
(a) $x = 1.032$ in.

(b) $x = 3.096$ in.

Figure 27. Reynolds normal stress $\left(\overline{v'v'}\right)$ profiles for nonaxisymmetric boattail model. $y = 0$ in.; $\alpha = 0°$.
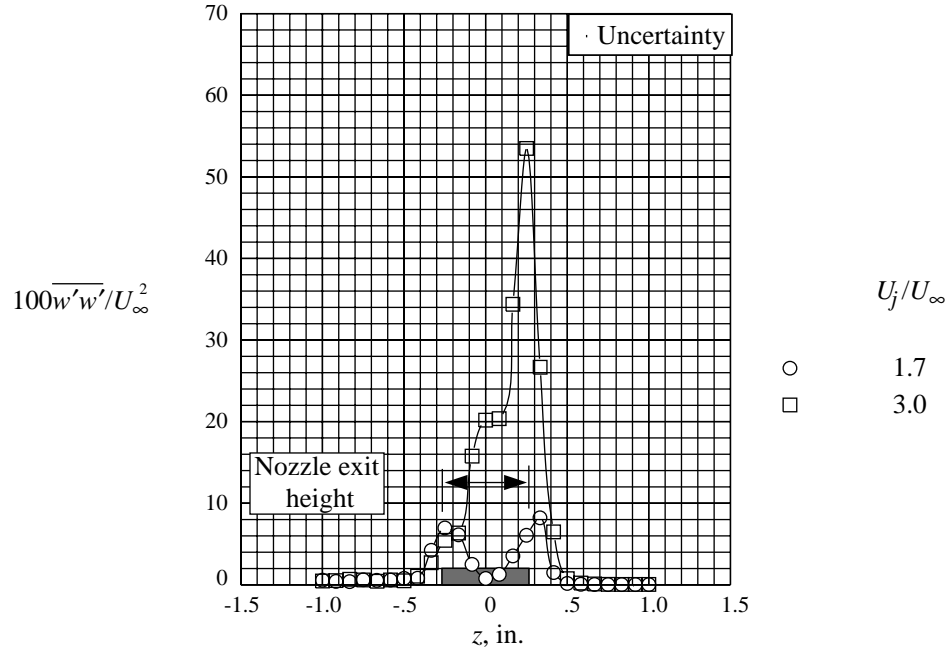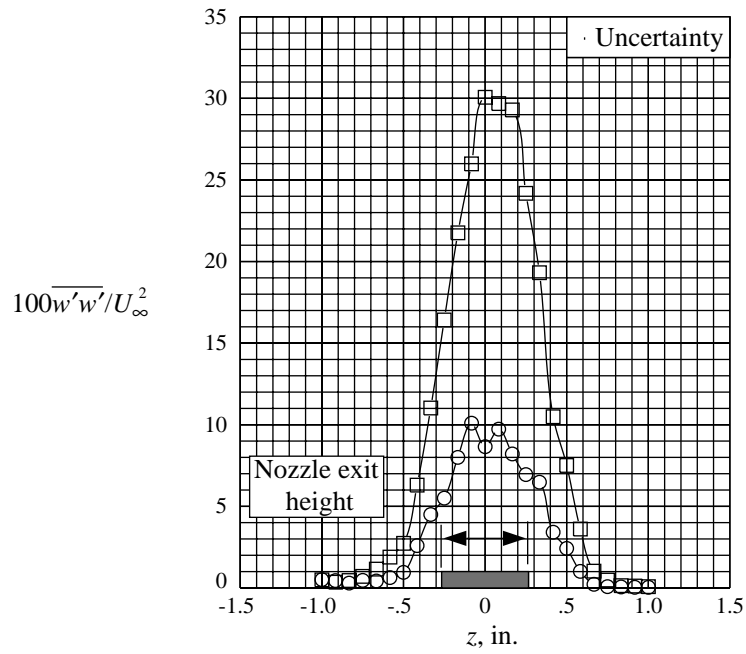
(a) $x = 1.032$ in.

(b) $x = 3.096$ in.

Figure 28. Reynolds normal stress $\left(\overline{w'w'}\right)$ profiles for nonaxisymmetric boattail model. $y = 0$ in.; $\alpha = 0°$.
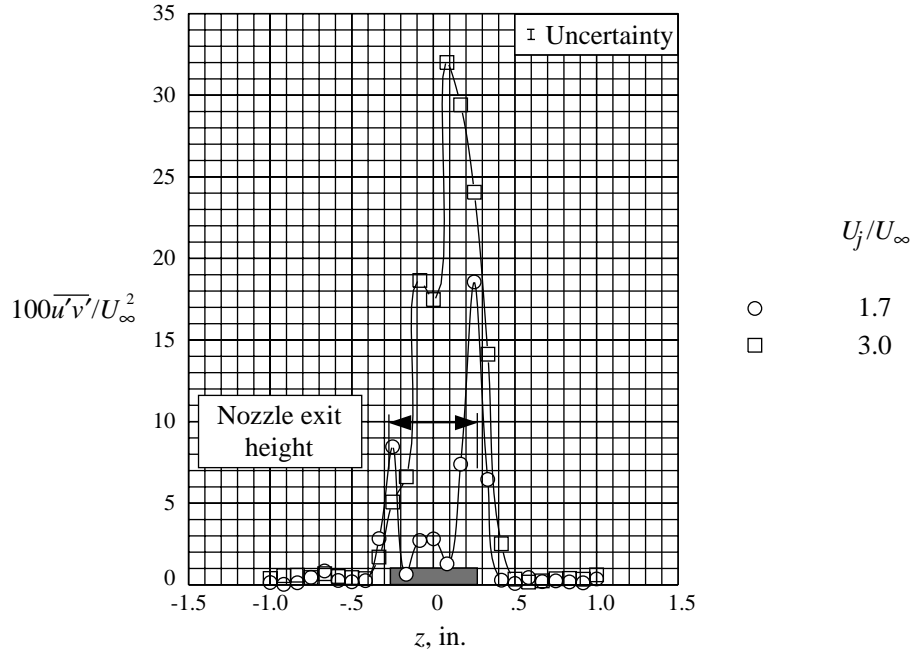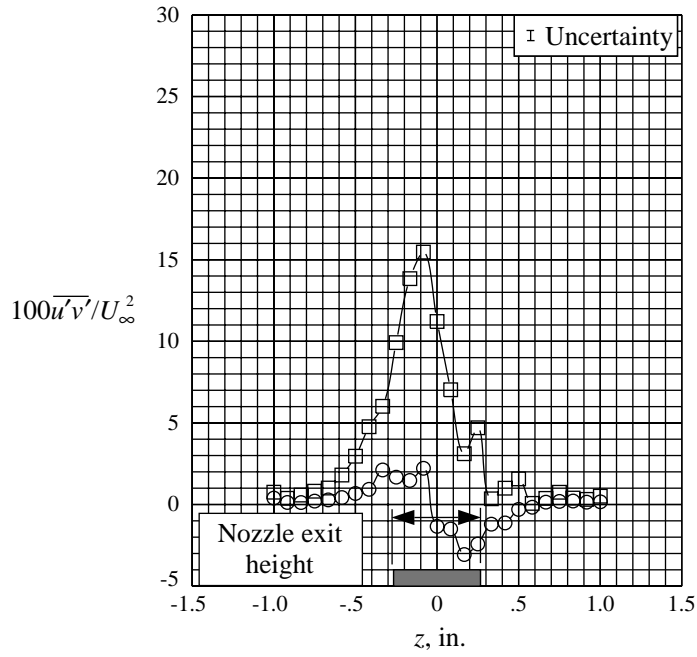
(a) $x = 1.032$ in.

(b) $x = 3.096$ in.

Figure 29. Reynolds shear stress $\left(\overline{u'v'}\right)$ profiles for nonaxisymmetric boattail model. $y = 0$ in.; $\alpha = 0°$.
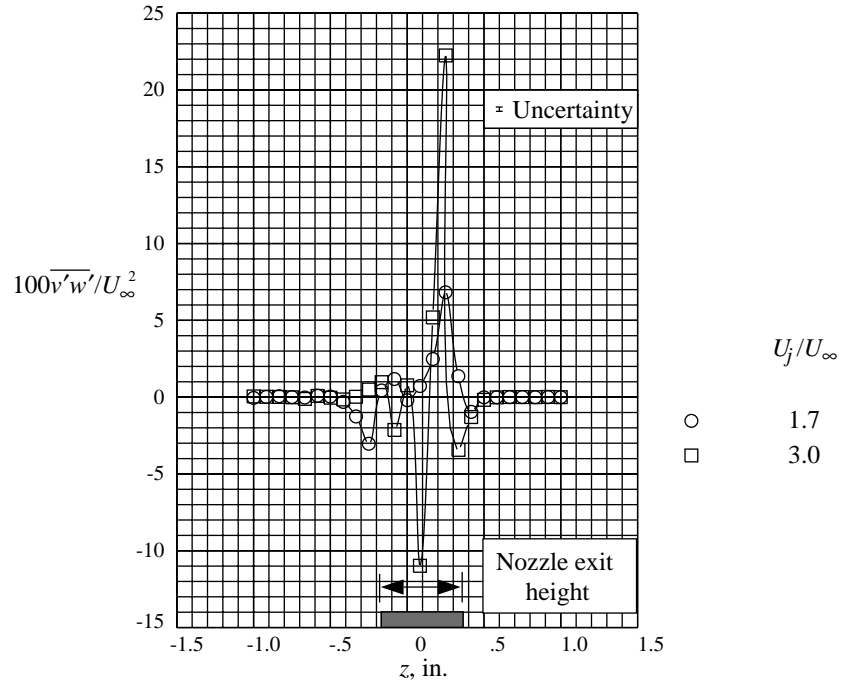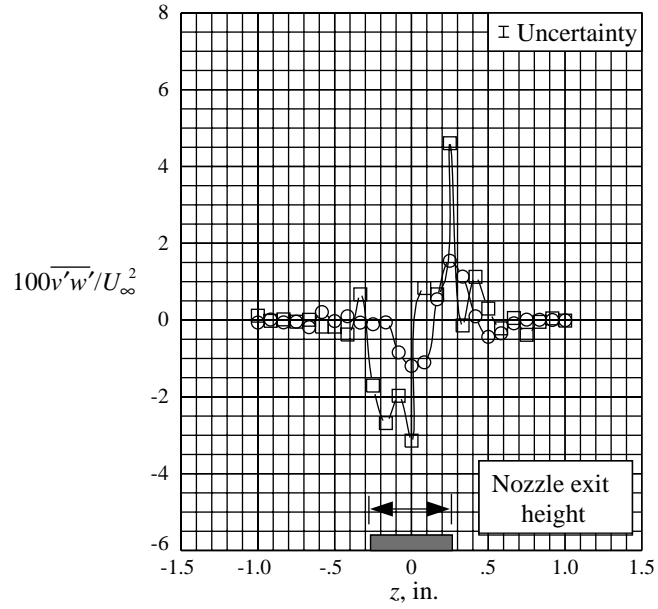
(a) $x = 1.032$ in.

(b) $x = 3.096$ in.

Figure 30. Reynolds shear stress $\left(\overline{v'w'}\right)$ profiles for nonaxisymmetric boattail model. $y = 0$ in.; $\alpha = 0°$.
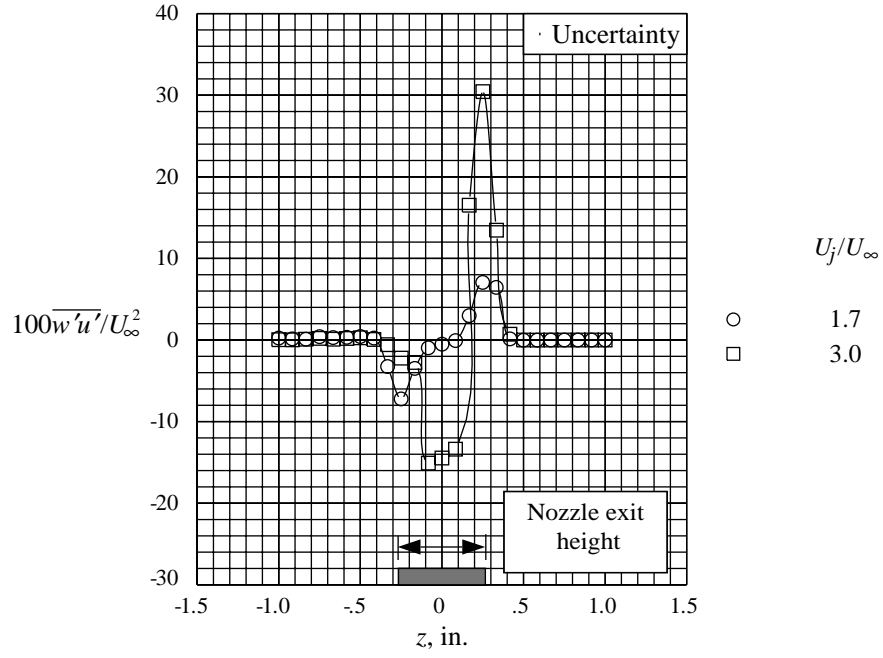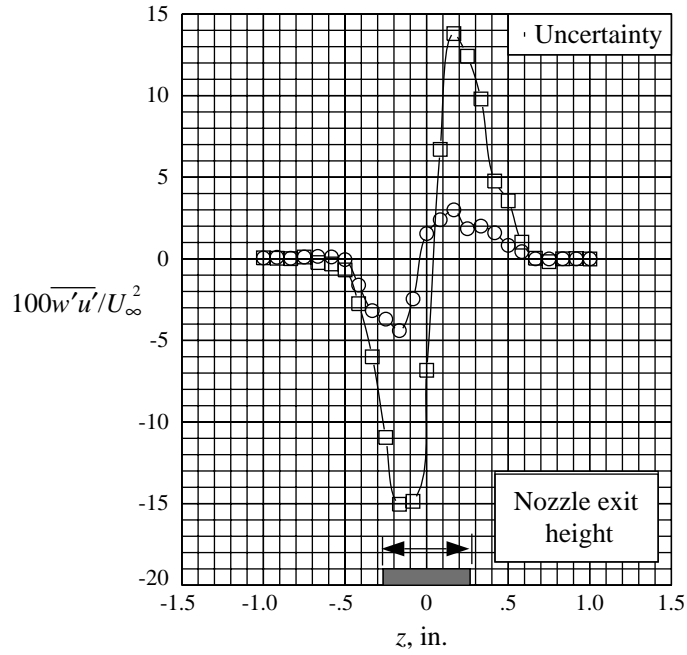
(a) $x = 1.032$ in.

(b) $x = 3.096$ in.

Figure 31. Reynolds shear stress $\left(\overline{w'u'}\right)$ profiles for nonaxisymmetric boattail model. $y = 0$ in.; $\alpha = 0°$.
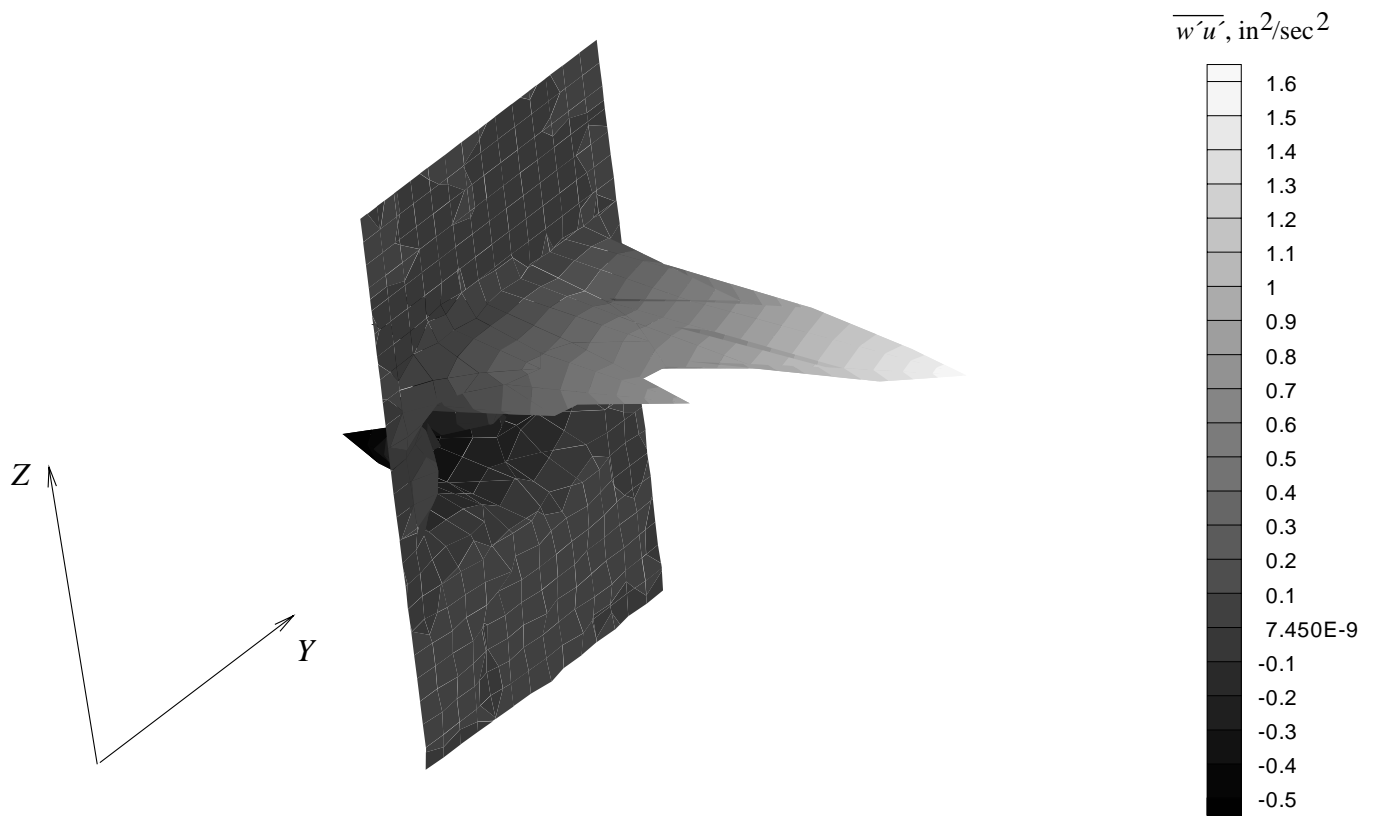
Figure 32. Reynolds shear stress $\overline{w'u'}$. $x = 1.032$ in.; $U_j/U_\infty = 1.7$; $\alpha = 0°$.

$\overline{w'u'}$, in^2/sec^2

1.6
1.5
1.4
1.3
1.2
1.1
1
0.9
0.8
0.7
0.6
0.5
0.4
0.3
0.2
0.1
7.450E-9
-0.1
-0.2
-0.3
-0.4
-0.5
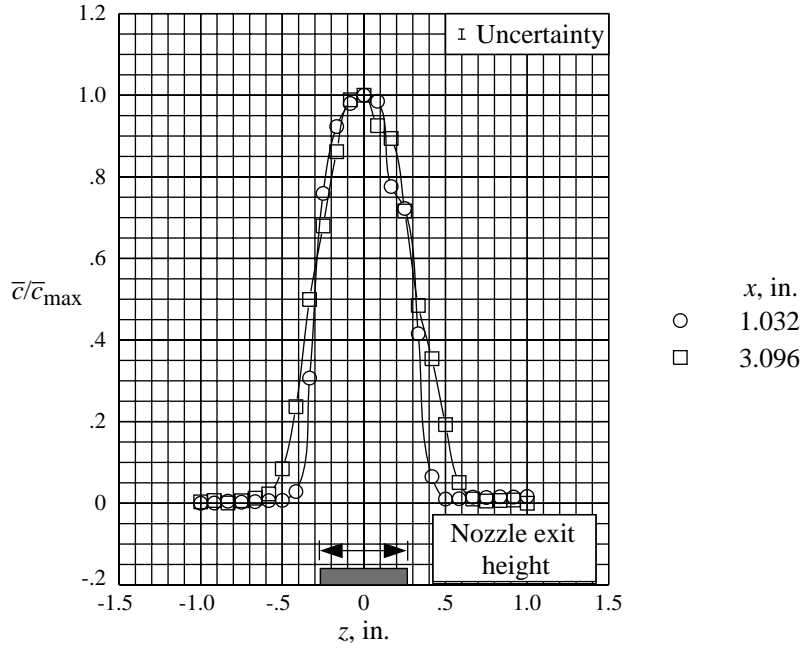
Figure 33. Fluorescent dye concentration profiles for nonaxisymmetric boattail model. $y = 0$ in.; $\alpha = 0°$; $U_j/U_\infty = 1.7$.
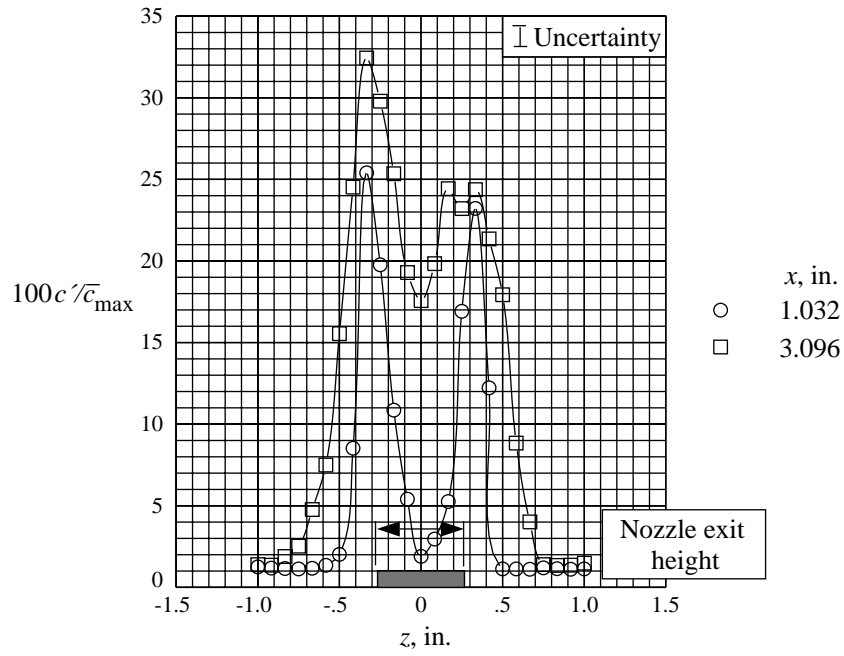
Figure 34. Fluorescent dye concentration fluctuations for nonaxisymmetric boattail model. $y = 0$ in.; $\alpha = 0°$; $U_j/U_\infty = 1.7$.
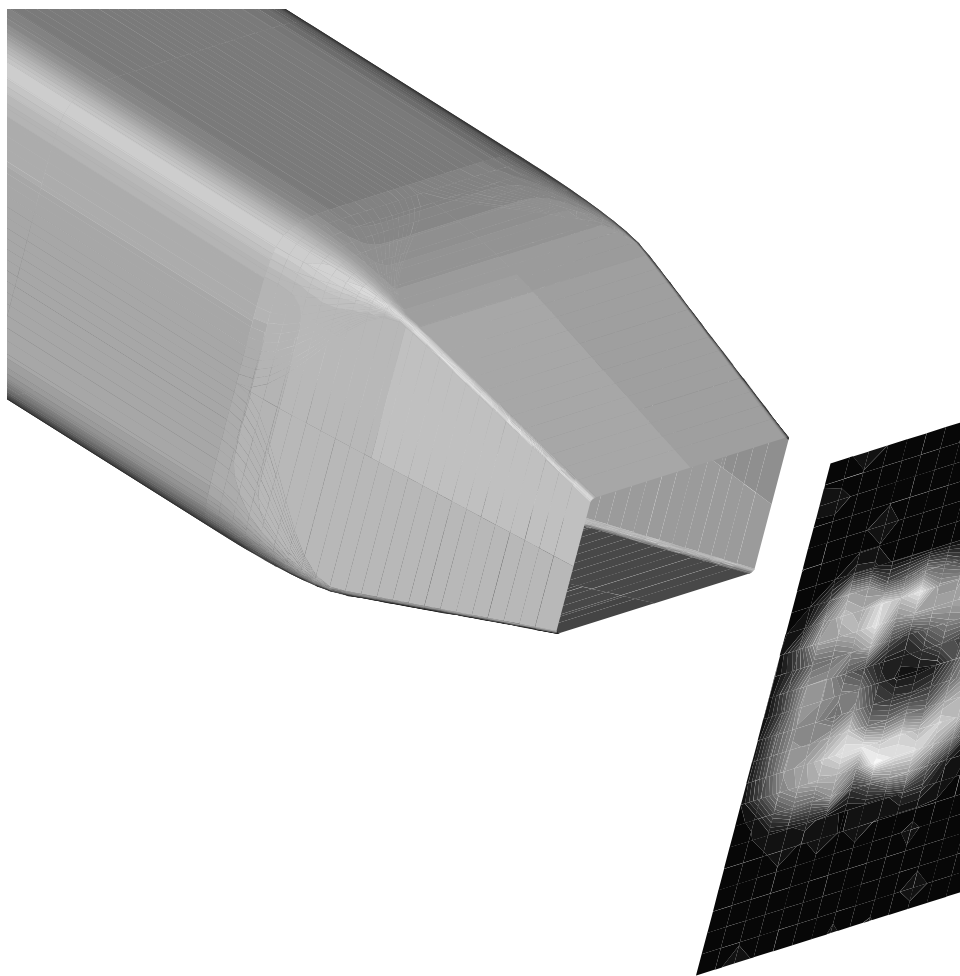
Figure 35. Fluorescent dye concentration fluctuations. $x = 1.032$ in.; $U_j/U_\infty = 1.7$; $\alpha = 0°$.

(a) $x = 1.032$ in.

(b) $x = 3.096$ in.
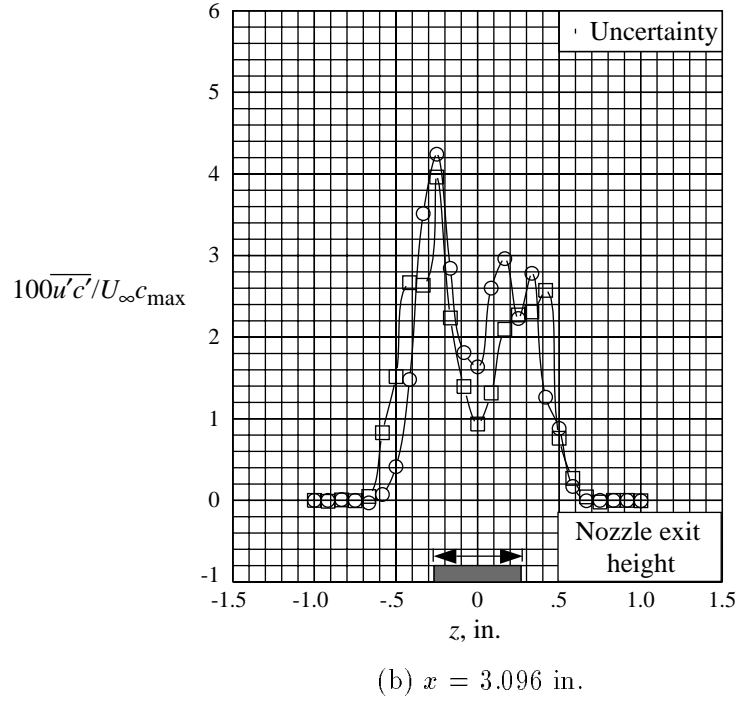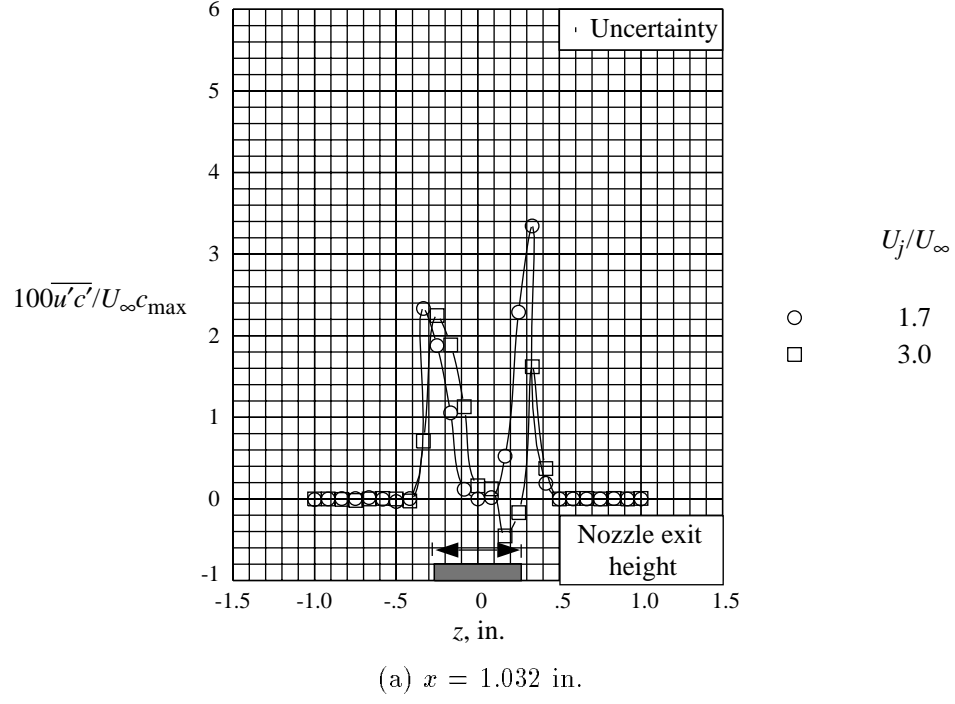
Figure 36. Correlation between axial velocity and concentration fluctuations for nonaxisymmetric boattail model. $y = 0$ in.; $\alpha = 0°$.

71

(a) $x = 1.032$ in.

(b) $x = 3.096$ in.
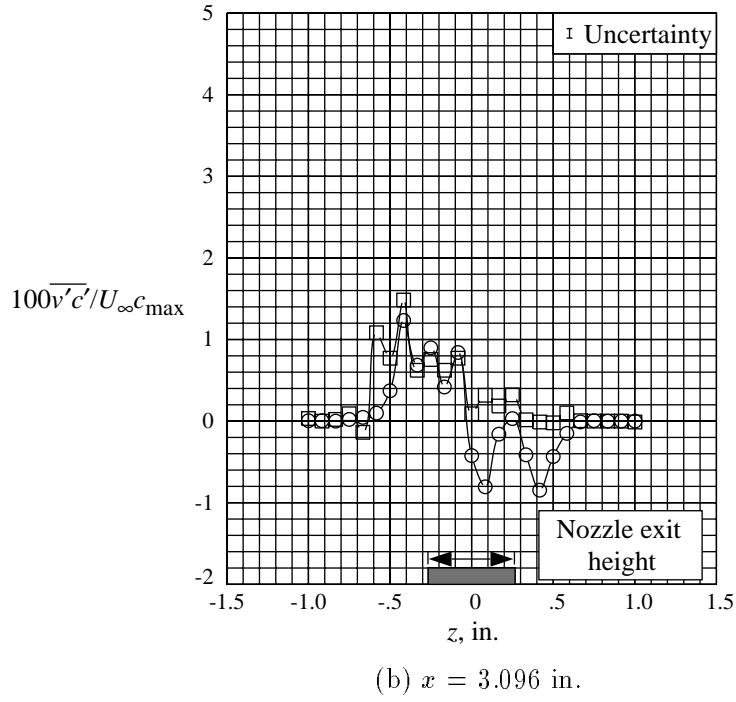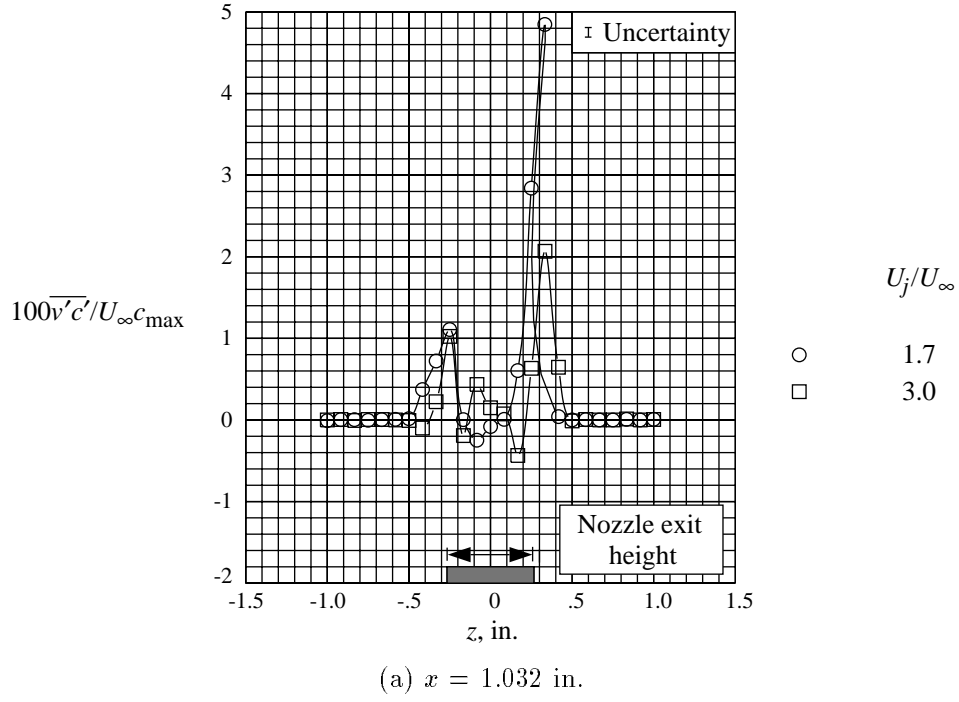
Figure 37. Correlation between transverse velocity and concentration fluctuations for nonaxisymmetric boattail model. $y = 0$ in.; $\alpha = 0°$.

(a) $x = 1.032$ in.

(b) $x = 3.096$ in.
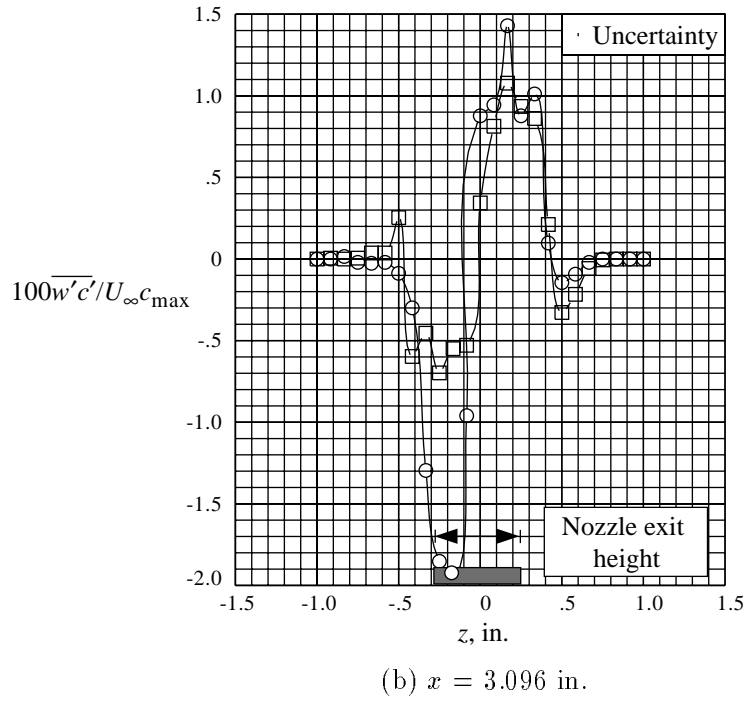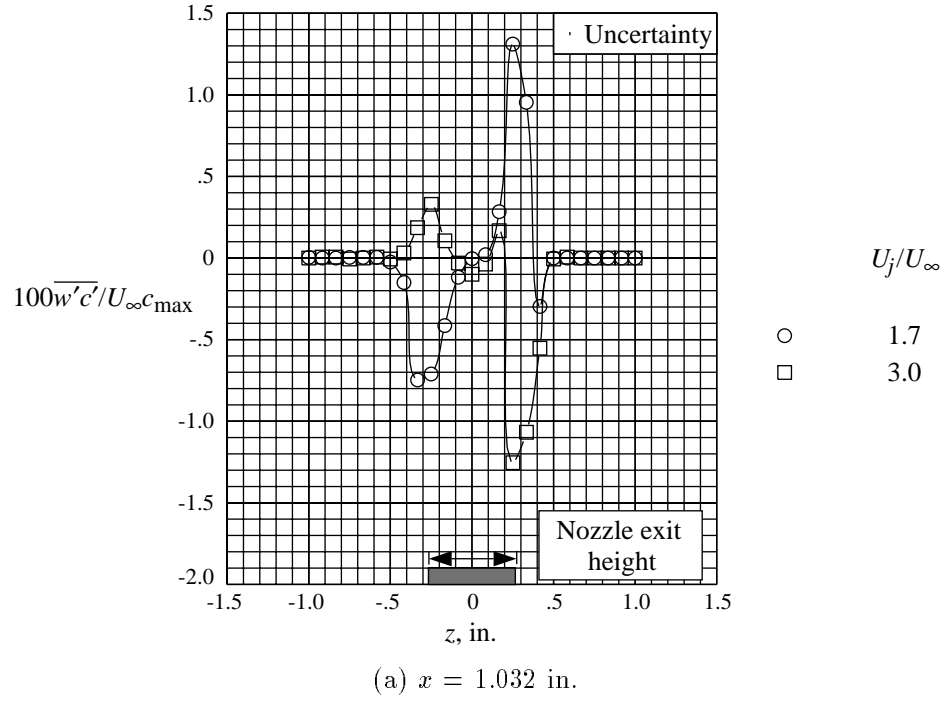
Figure 38. Correlation between vertical velocity and concentration fluctuations for nonaxisymmetric boattail model. $y = 0$ in.; $\alpha = 0°$.

(a) $x = 1.875$ in.

(b) $x = 3.75$ in.

Flow

(c) $x = 5.15$ in.

(d) $x = 10$ in.
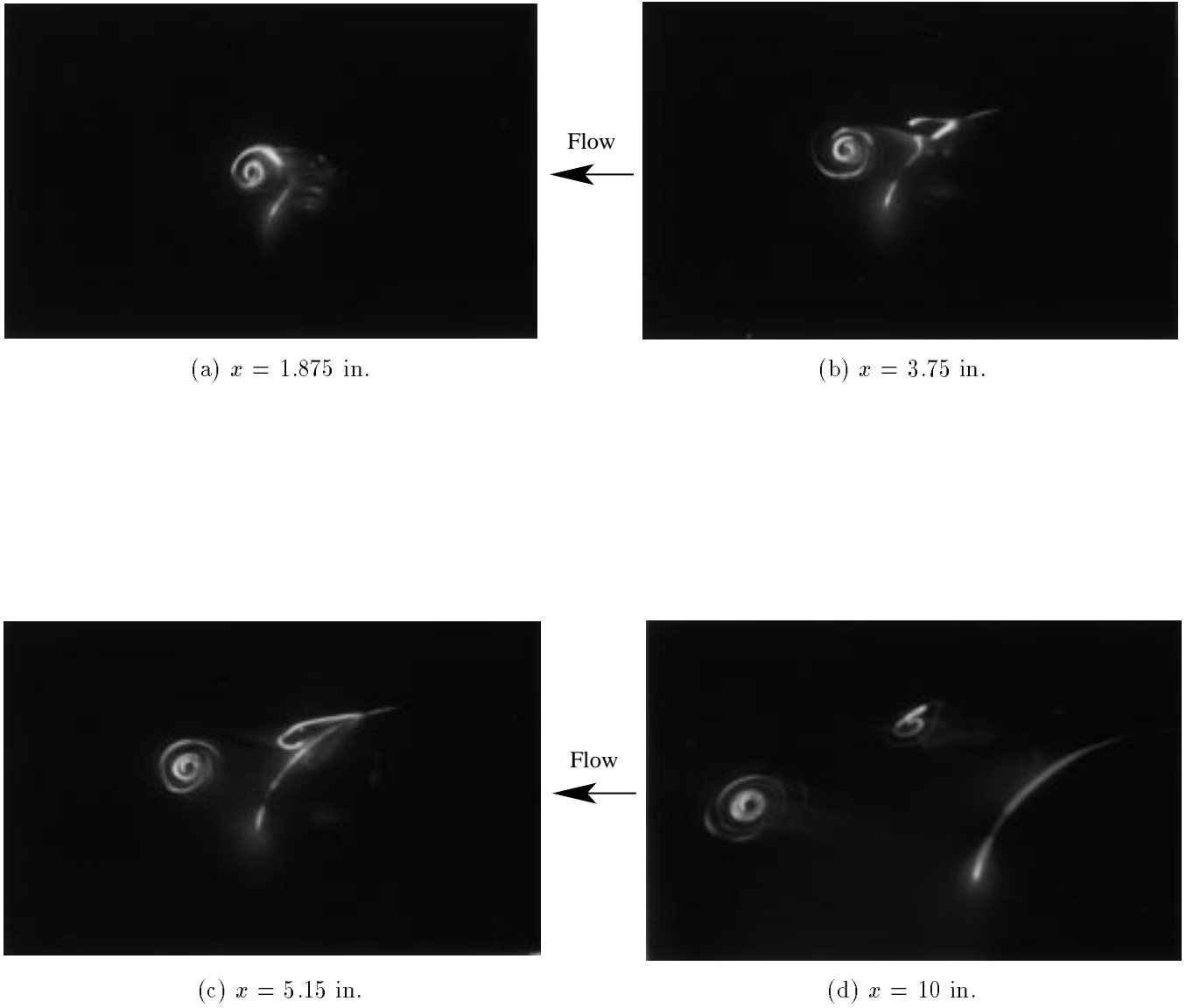
Flow

Figure 39. Laser light sheet flow visualization of axisymmetric forebody with strake. $\alpha = 25°$; $\phi = 50°$.

(a) $x = 1.875$ in.

(b) $x = 3.75$ in.

Flow

(c) $x = 5.15$ in.

(d) $x = 10$ in.
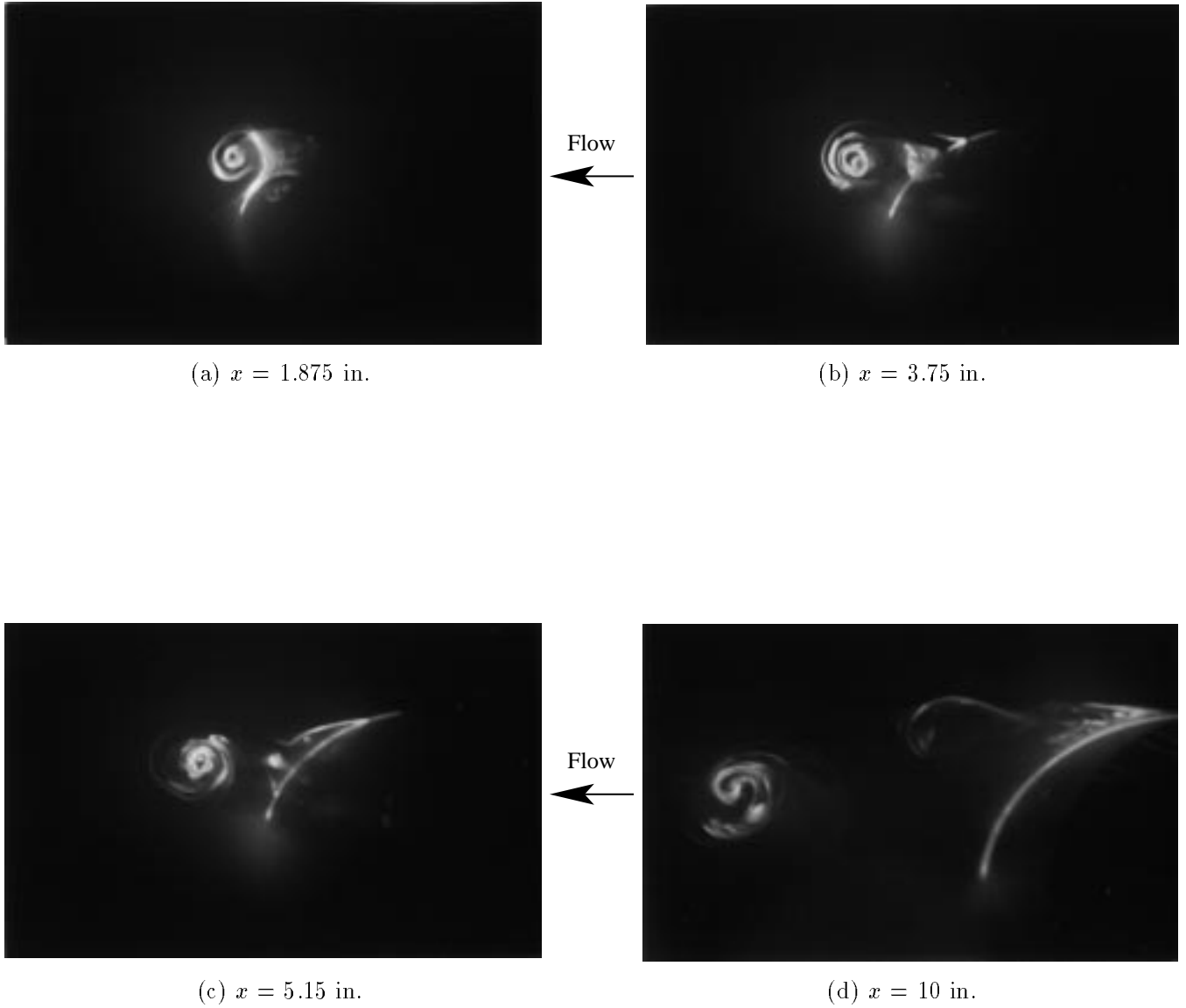
Flow

Figure 40. Laser light sheet flow visualization of axisymmetric forebody with strake. $\alpha = 25°$; $\phi = 60°$.
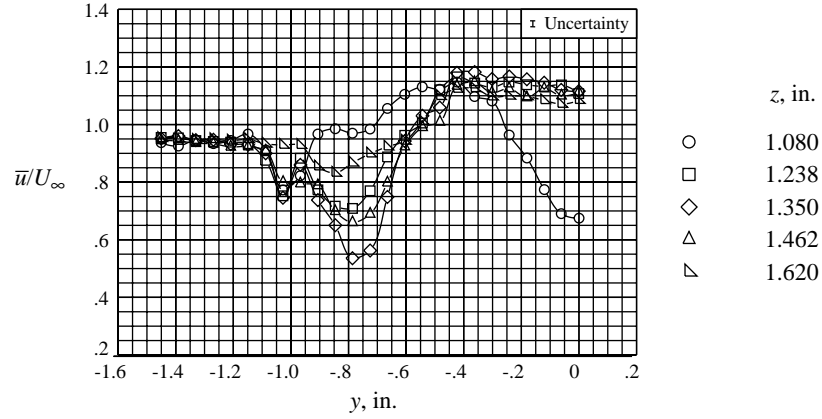
(a) Axial velocity.
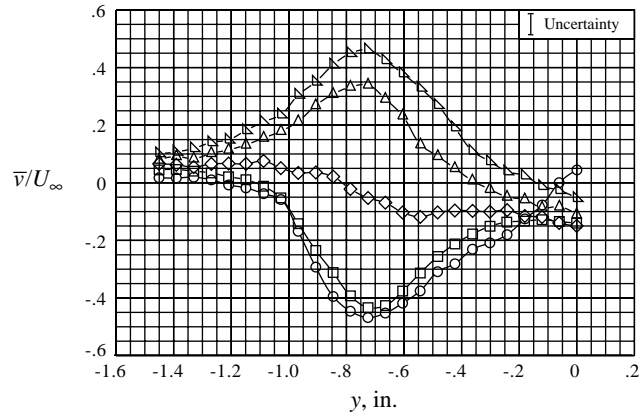
(b) Transverse velocity.
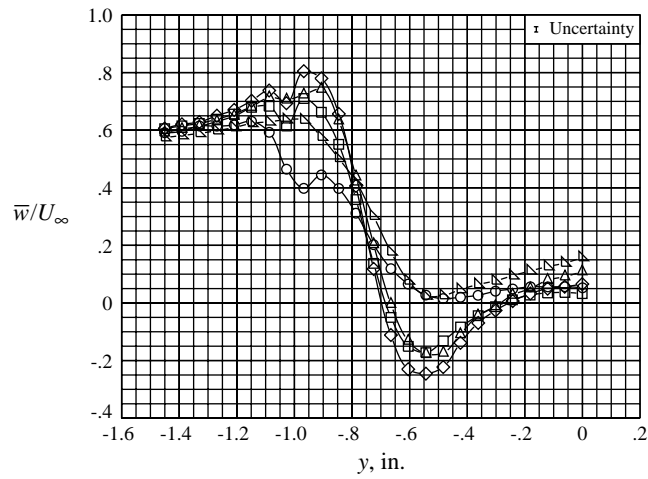
(c) Vertical velocity.

Figure 41. Vortex velocity profiles for forebody model with baseline strake installed. $\phi = 50°$; $\alpha = 25°$; $x = 3.75$ in.
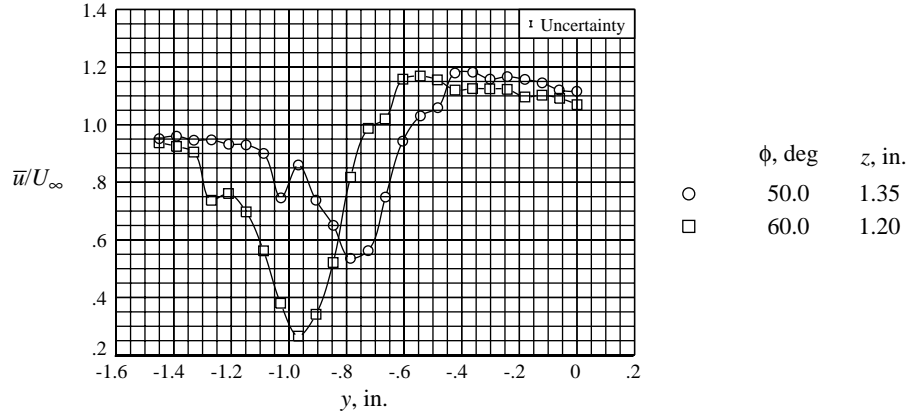
(a) Axial velocity.
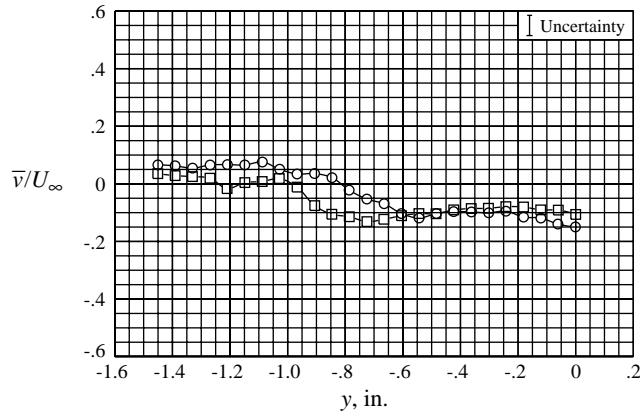
(b) Transverse velocity.
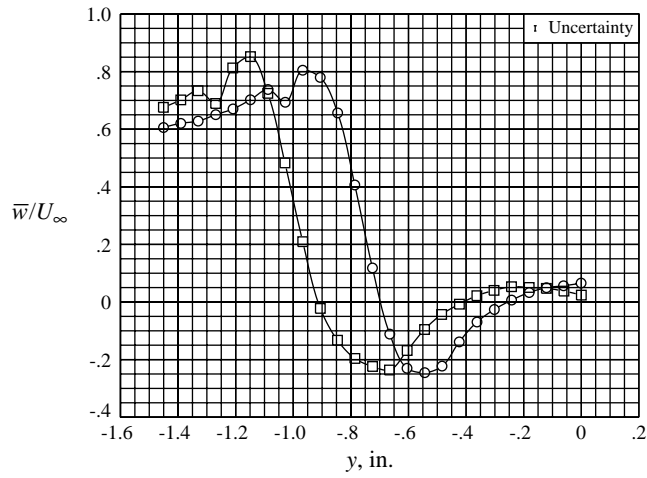
(c) Vertical velocity.

Figure 42. Effect of strake position on vortex velocity profiles for forebody model with baseline strake installed. $\alpha = 25°$; $x = 3.75$ in.

(a) Axial velocity.

Strake	x, in.
○ Baseline	5.15
□ Cambered	5.40

(b) Transverse velocity.

(c) Vertical velocity.
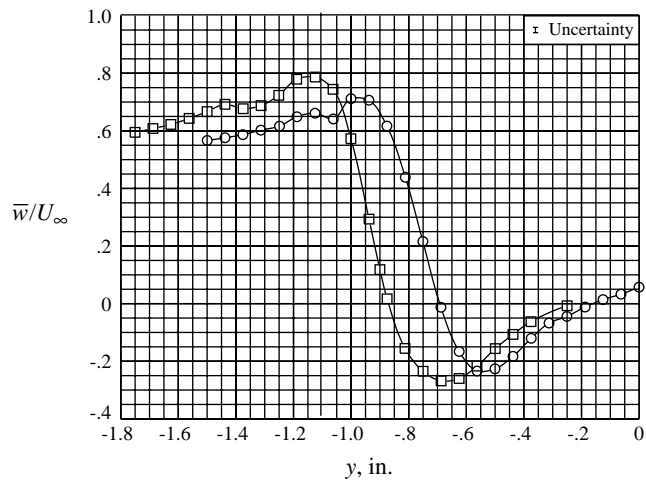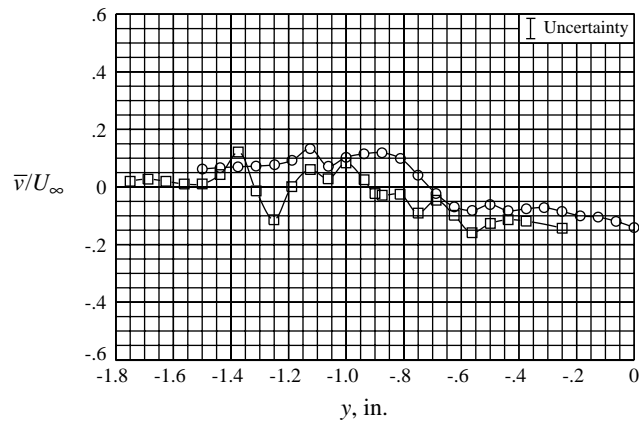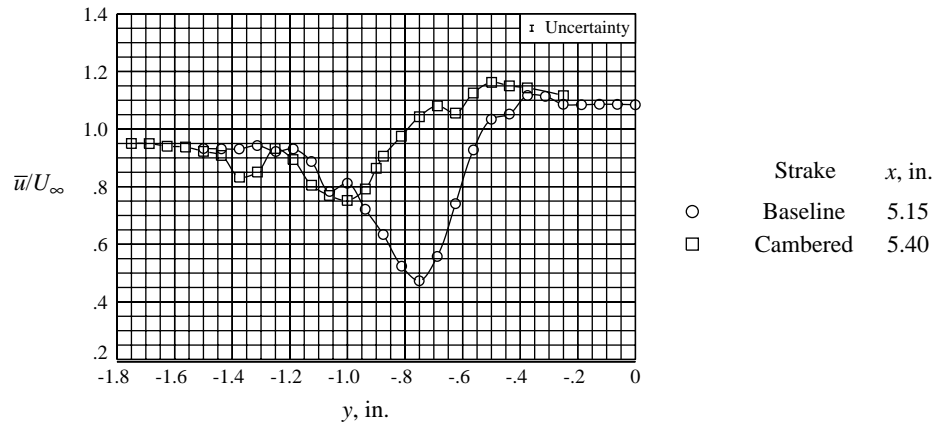
Figure 43. Effect of strake geometry on vortex velocity profiles for forebody model. $\phi = 50°$; $\alpha = 25°$; $z = 1.75$ in.
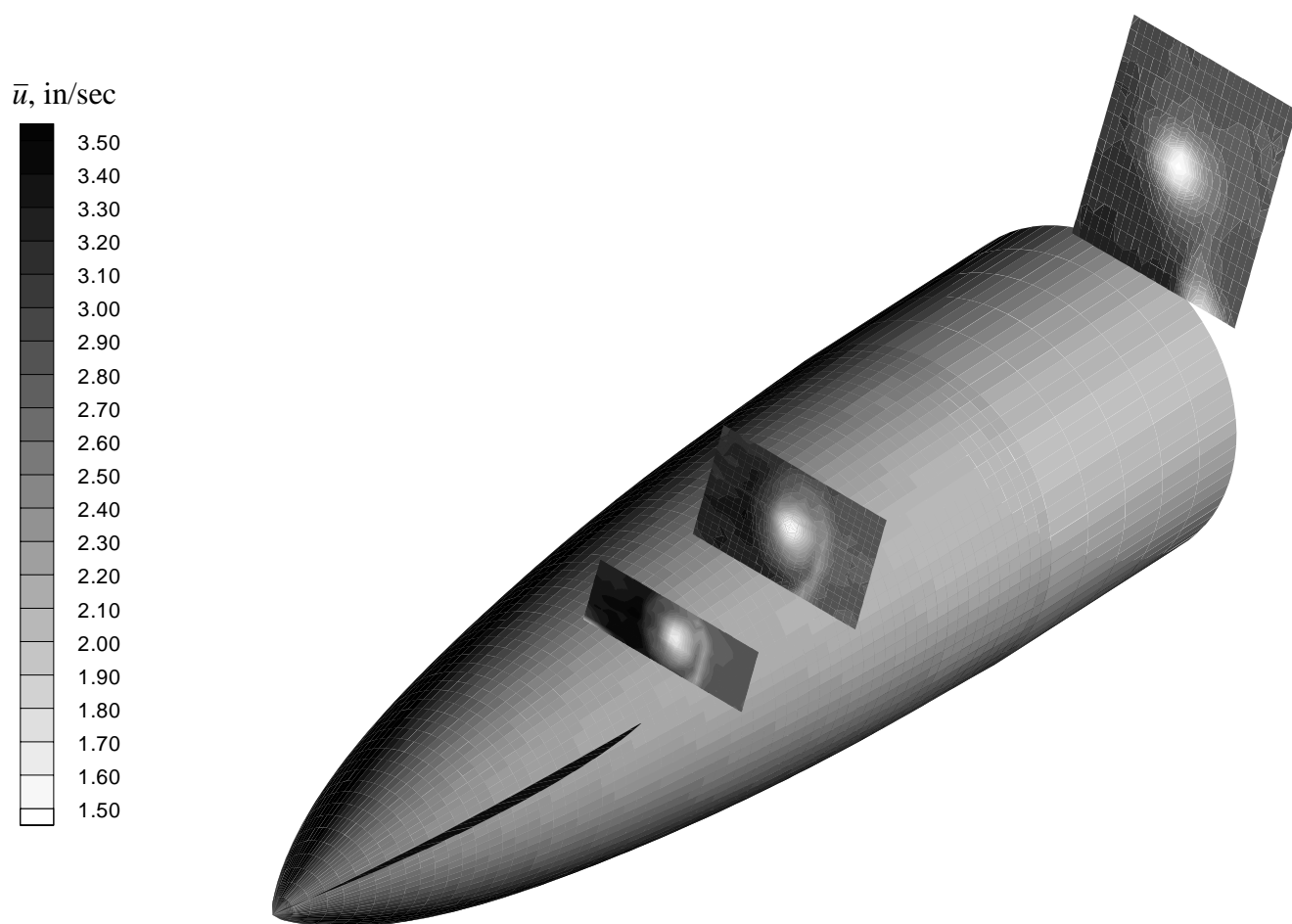
Figure 44. Axial velocity contours. $\alpha = 25°$; $\phi = 50°$.
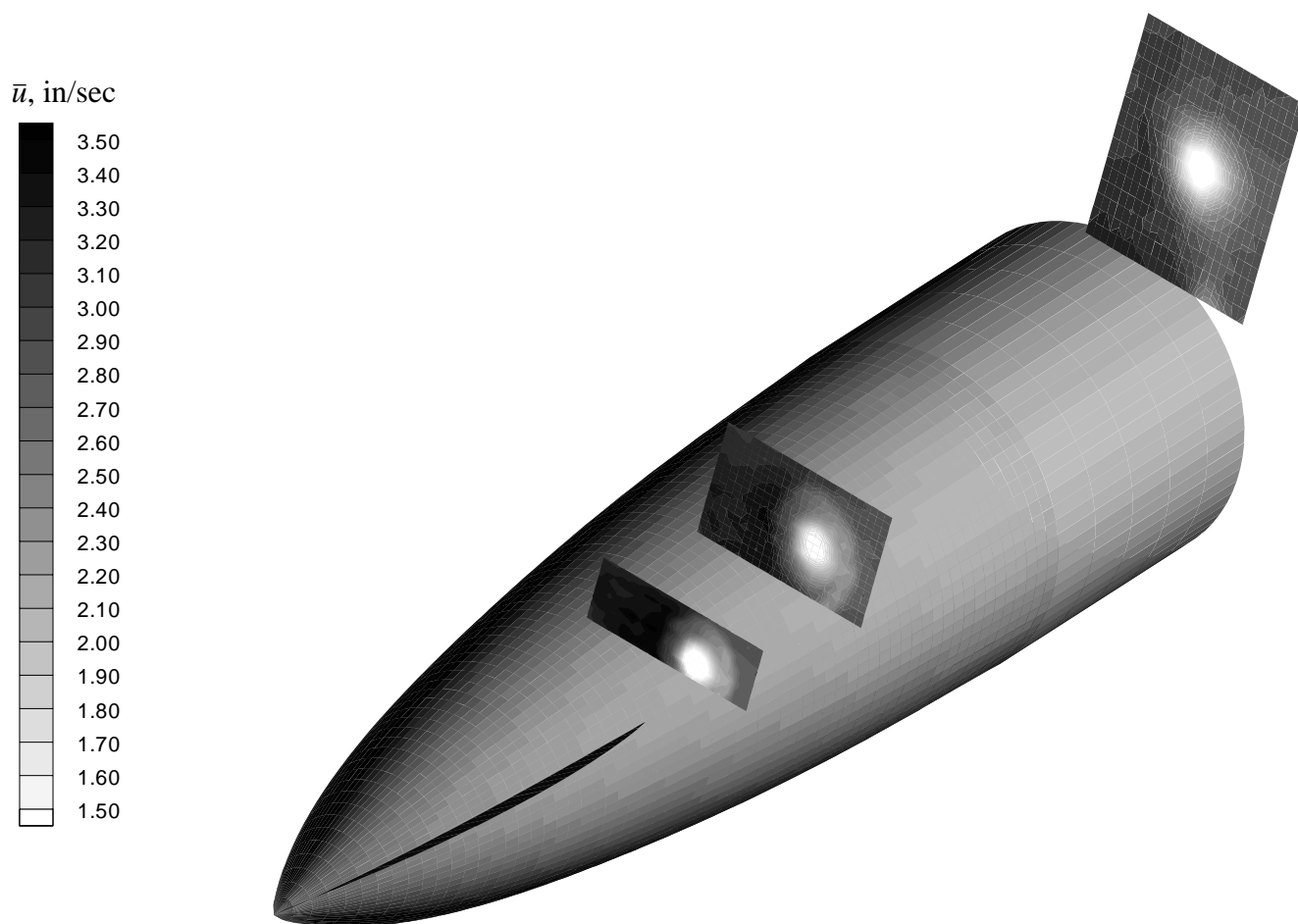
Figure 45. Axial velocity contours. $\alpha = 25°$; $\phi = 60°$.
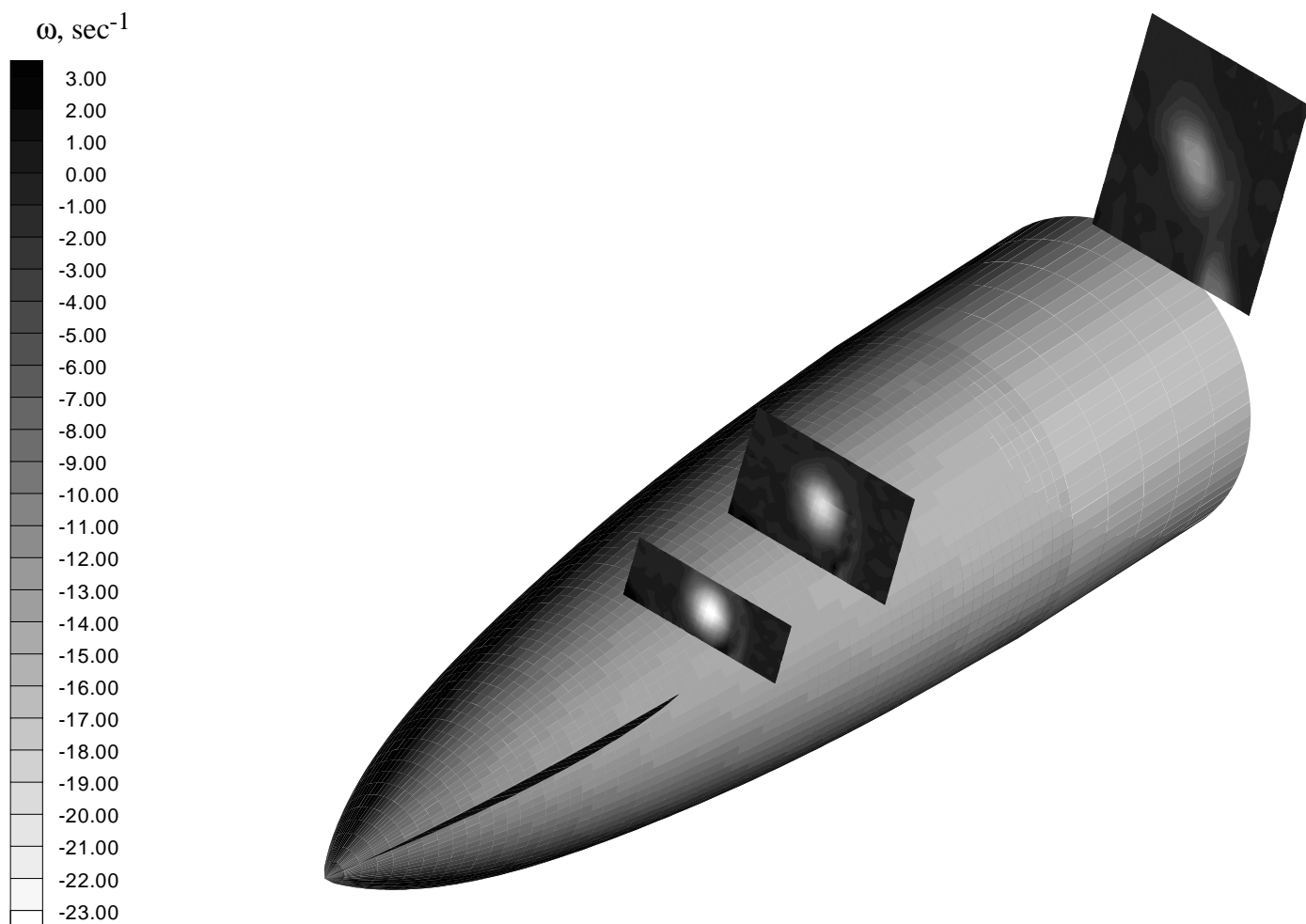
Figure 46. Streamwise vorticity contours. $\alpha = 25°$; $\phi = 50°$.
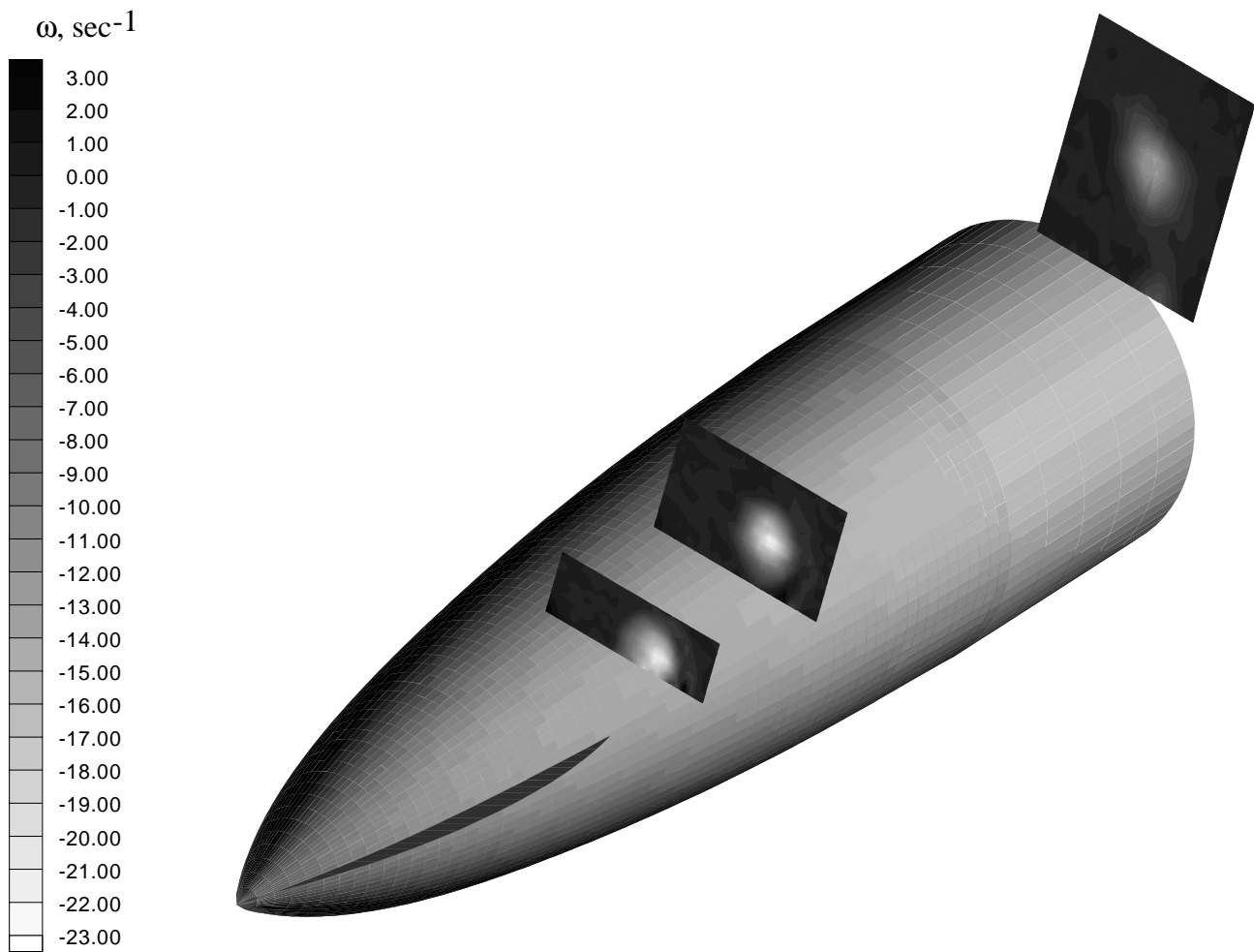
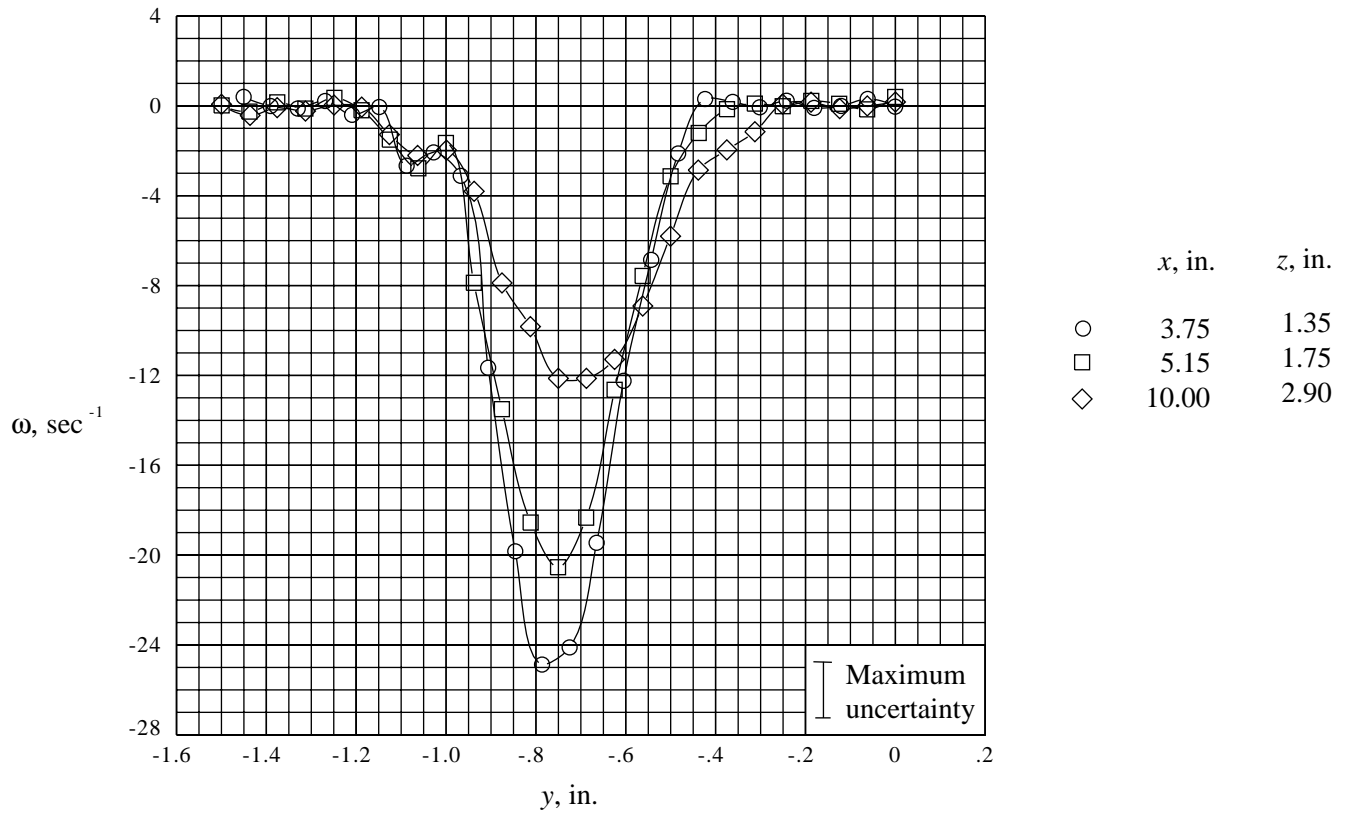Figure 47. Streamwise vorticity contours. $\alpha = 25°$; $\phi = 60°$.

Figure 48. Axial vorticity along scan line through center of forebody-strake model vortex. Baseline strake $\phi = 50°$; $\alpha = 25°$.
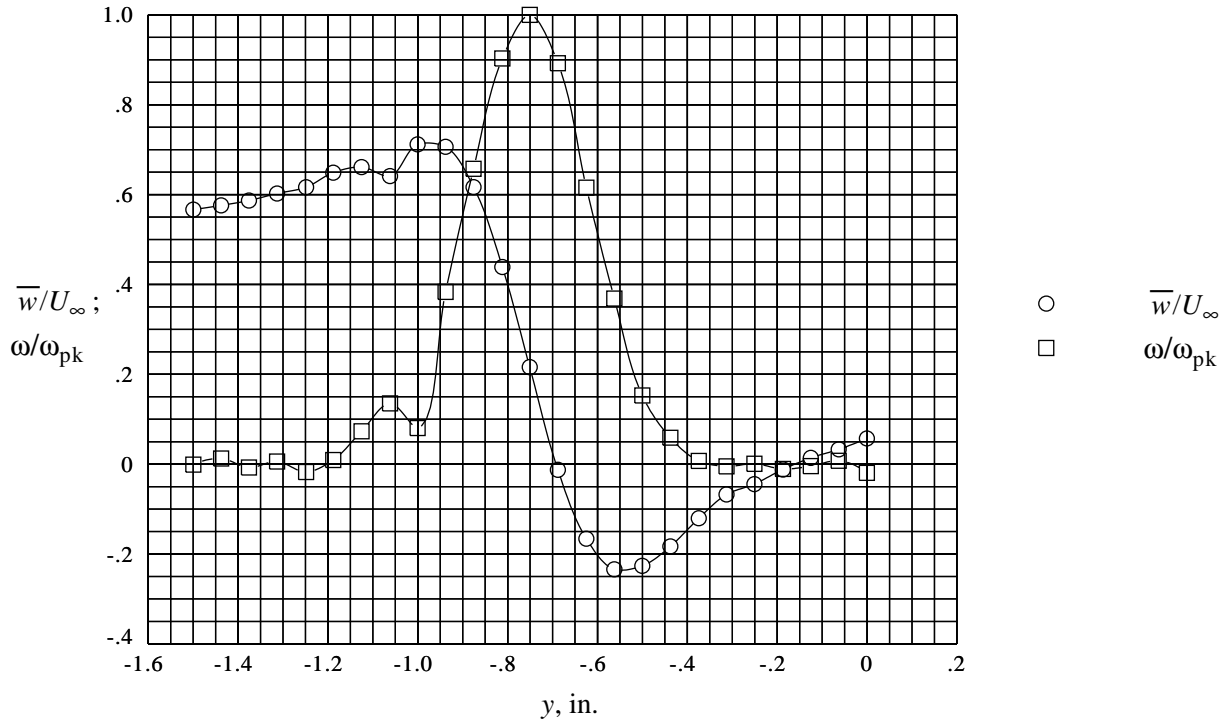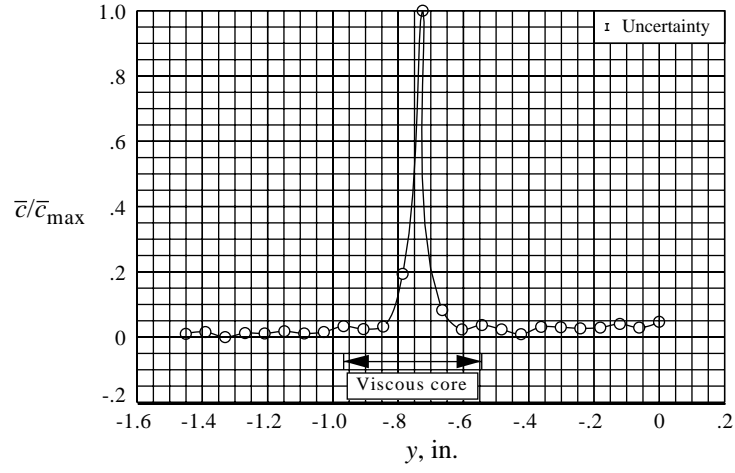

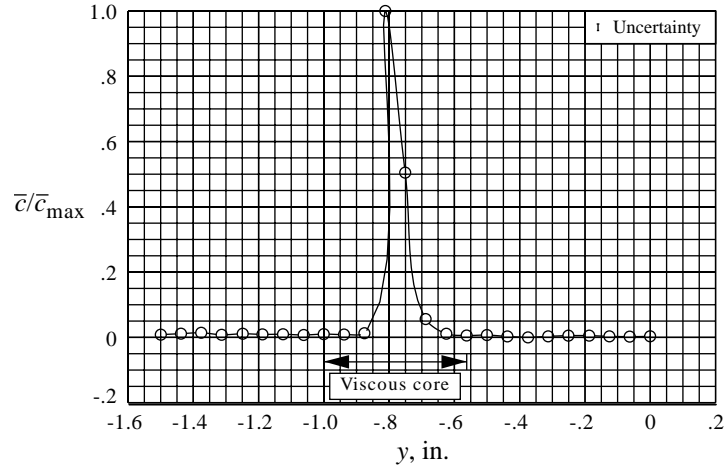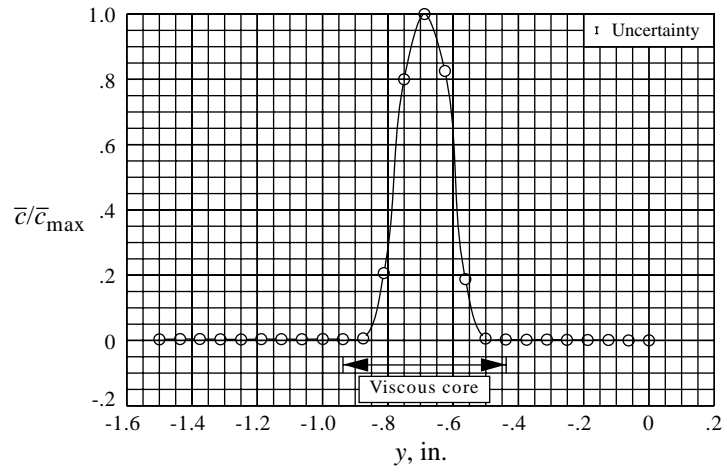Figure 49. Comparison of vertical velocity and streamwise vorticity of forebody-strake model vortex. Baseline strake $\phi = 50°$; $\alpha = 25°$; $x = 5.15$ in.; $z = 1.75$ in.

(a) $x = 3.75$ in.; $z = 1.35$ in.

(b) $x = 5.15$ in.; $z = 1.75$ in.

(c) $x = 10$ in.; $z = 2.9$ in.

Figure 50. Fluorescent dye concentration profiles in vortex of forebody-strake model. Baseline strake $\phi = 50°$; $\alpha = 25°$.

REPORT DOCUMENTATION PAGE

Public reporting burden for this collection of information is estimated to average 1 hour per response, including the time for reviewing instructions, searching existing data sources, gathering and maintaining the data needed, and completing and reviewing the collection of information. Send comments regarding this burden estimate or any other aspect of this collection of information, including suggestions for reducing this burden, to Washington Headquarters Services, Directorate for Information Operations and Reports, 1215 Jefferson Davis Highway, Suite 1204, Arlington, VA 22202-4302, and to the Office of Management and Budget, Paperwork Reduction Project (0704-0188), Washington, DC 20503.

1. AGENCY USE ONLY (Leave blank)	2. REPORT DATE September 1994	3. REPORT TYPE AND DATES COVERED Technical Paper

4. TITLE AND SUBTITLE
Simultaneous Three-Dimensional Velocity and Mixing Measurements by Use of Laser Doppler Velocimetry and Fluorescence Probes in a Water Tunnel

5. FUNDING NUMBERS
WU 505-62-30-01

6. AUTHOR(S)
Dan H. Neuhart, David J. Wing, and Uleses C. Henderson, Jr.

7. PERFORMING ORGANIZATION NAME(S) AND ADDRESS(ES)
NASA Langley Research Center
Hampton, VA 23681-0001

8. PERFORMING ORGANIZATION REPORT NUMBER
L-17328

9. SPONSORING/MONITORING AGENCY NAME(S) AND ADDRESS(ES)
National Aeronautics and Space Administration
Washington, DC 20546-0001

10. SPONSORING/MONITORING AGENCY REPORT NUMBER
NASA TP-3454

11. SUPPLEMENTARY NOTES
Neuhart: Lockheed Engineering & Sciences Company, Hampton, VA; Wing: Langley Research Center, Hampton, VA; Henderson: Purdue University, West Lafayette, IN.

12a. DISTRIBUTION/AVAILABILITY STATEMENT

Unclassified–Unlimited

Subject Category 09

12b. DISTRIBUTION CODE

13. ABSTRACT (Maximum 200 words)

A water tunnel investigation was conducted to demonstrate the capabilities of a laser-based instrument that can measure velocity and fluorescence intensity simultaneously. Fluorescence intensity of an excited fluorescent dye is directly related to concentration level and was used to indicate the extent of mixing in flow. This instrument is a three-dimensional laser Doppler velocimeter (LDV) in combination with a fluorometer for measuring fluorescence intensity variations. This capability allows simultaneous flow measurements of the three orthogonal flow velocity components and mixing within the same region. Two different flows generated by two models were studied: a generic nonaxisymmetric nozzle propulsion simulation model with an auxiliary internal water source that generated a jet flow and an axisymmetric forebody model with a circular sector strake that generated a vortex flow. The off-body flow fields around these models were investigated in the Langley 16- by 24-Inch Water Tunnel. The experimental results were used to calculate 17 quantities that included mean and fluctuating velocities, Reynolds stresses, mean and fluctuating dye fluorescence intensities (proportional to concentration), and fluctuating velocity and dye concentration correlations. An uncertainty analysis was performed to establish confidence levels in the experimental results. These results show characteristics that are unique to each type of flow.

14. SUBJECT TERMS
Laser velocimetry; Vortex flow; Jet flow; Uncertainty analysis; Fluorometry

15. NUMBER OF PAGES
87

16. PRICE CODE
A05

17. SECURITY CLASSIFICATION OF REPORT Unclassified	18. SECURITY CLASSIFICATION OF THIS PAGE Unclassified	19. SECURITY CLASSIFICATION OF ABSTRACT Unclassified	20. LIMITATION OF ABSTRACT

NSN 7540-01-280-5500

Standard Form 298 (Rev. 2-89)
Prescribed by ANSI Std. Z39-18
298-102